2022

MOLECULAR MODELING OF HIGH-PERFORMANCE THERMOSET POLYMER MATRIX COMPOSITES FOR AEROSPACE APPLICATIONS

Prathamesh P. Deshpande
Michigan Technological University, ppdeshpa@mtu.edu

Recommended Citation

Deshpande, Prathamesh P., "MOLECULAR MODELING OF HIGH-PERFORMANCE THERMOSET POLYMER MATRIX COMPOSITES FOR AEROSPACE APPLICATIONS", Open Access Dissertation, Michigan Technological University, 2022.
https://doi.org/10.37099/mtu.dc.etdr/1430

MOLECULAR MODELING OF HIGH-PERFORMANCE THERMOSET POLYMER MATRIX COMPOSITES FOR AEROSPACE APPLICATIONS

By

Prathamesh P. Deshpande

A DISSERTATION

Submitted in partial fulfillment of the requirements for the degree of

DOCTOR OF PHILOSOPHY

In Mechanical Engineering-Engineering Mechanics

MICHIGAN TECHNOLOGICAL UNIVERSITY

2022

This dissertation has been approved in partial fulfillment of the requirements for the Degree of DOCTOR OF PHILOSOPHY in Mechanical Engineering-Engineering Mechanics.

Department of Mechanical Engineering-Engineering Mechanics

Dissertation Co-Advisor: *Dr. Gregory M. Odegard*

Dissertation Co-Advisor: *Dr. Susanta Ghosh*

Committee Member: *Dr. Trisha Sain*

Committee Member: *Dr. Gowtham S.*

Department Chair: *Dr. Jason R. Blough*

Table of Contents

List of Figures

List of Tables

Author Contribution Statement

This research was performed under the guidance of Dr. Gregory Odegard. He has reviewed and supplemented the manuscript as well as provided much needed information for conducting certain challenges throughout this work. Dr. Aaron Kreig and Dr. Julia King supplied the experimental data discussed in Chapter 3; Dr. Kreig wrote the section 3.2. Dr. Matthew Radue helped with setting up the MD simulations in Chapter 4. Dr. Aowabin Rahman and Dr. Susanta Ghosh provided the much-needed guidance with understanding the MD simulation setup in Chapter 5. Karen DeMille executed some of the MD simulations and developed the GCN model discussed in Chapter 5.

Chapter 4: Reprinted (adapted) with permission from Langmuir 2021, 37, 39, 11526–11534; DOI: 10.1021/acs.langmuir.1c01800. Copyright 2021 American Chemical Society.

Acknowledgements

I would first like to thank my advisor Dr. Gregory Odegard for providing the opportunity to work on this research. His advice and teachings have been the foundation of this research. He has been patient with me and helped me through several speed bumps in my work. I would like to express gratitude to my committee members Dr. Susanta Ghosh, Dr. Trisha Sain, and Dr. Gowtham S.

This research would not have been possible without the guidance from Dr. Matthew Radue and Dr. Sorayot Chinkanjanarot. They have steered me through the fundamentals of Molecular Dynamics, data analysis and conducting good research.

I would specially like to acknowledge Dr. Marianna Maiaru and the University of Massachusetts Lowell's iComp^2 Lab and Dr. Ashley Spear, Dr. Aowabin Rahman and Karen DeMille from The University of Utah who have provided much needed guidance and research insights with my research projects.

Thanks to my fellow student researchers at Michigan Tech – Dr. Will Pisani, Dr. Hashim Al Mahmud, Sagar Patil, Joshua Kemppainen and Aaron Krieg. Each one has contributed to at least one of my research projects. Also, I appreciate my other fellow researchers Swapnil Bamane, Prashik Gaikwad, Ivan Gallegos, Khatereh Kashmari, Prasad Soman, Ninad Mohale and Apurva Baruah for providing good conversations.

I would also like to thank the entire USCOMP team for the opportunity to collaborate with such a large group of scholars and allowing me to present my work in form of presentations, posters, and research articles.

My wife Tanmayee has played a pivotal role in my years of pursuing Ph.D., she has sacrificed a lot and selflessly motivated me through the tough times. My son Dhruva, who has been a silent motivation for me to put in more work in my research. Lastly, I would like to thank my Aai, Baba, Prajakta, and my in-laws for their emotional support.

Ultimately, I would like to thank my Lord Shri Ram for helping me stay focused, motivated, and helping me find my way through grim times.

Abstract

The global efforts from major space agencies to transport humans to Mars will require a novel lightweight and ultra-high strength material for the spacecraft structure. Three decades of research with the carbon nanotubes (CNTs) have proved that the material can be an ideal candidate for the composite reinforcement if certain shortcomings are overcome. Also, the rapid development of the polymer resin industry has introduced a wide range of high-performance resins that show high compatibility with the graphitic surface of the CNTs. This research explores the computational design of these materials and evaluates their efficacy as the next generation of aerospace structural materials.

Process-induced residual stresses are a commonly observed phenomenon in composite structures during the manufacturing process. These are generated because of resin shrinkage and relative thermal contraction between the resin and reinforcement during the curing process. Experimental or computational characterization of these stresses can be a challenge due to their complex nature. Predictive models of the curing process require detailed knowledge of the resin thermo-mechanical property evolution during the cure. Molecular Dynamics (MD) is implemented to predict the resin properties of EPON 828-Jeffamine D230 as a function of the crosslink density at room temperature. The molecular models are developed using the Reactive Interface Forcefield (IFF-R). The physical, mechanical, and thermal properties are validated experimentally and using the literature data. The predicted progression of resin properties indicates that each property evolves distinctively.

The next generation of ultra-high strength composites for structural components of vehicles for crewed missions to deep space will incorporate flattened carbon nanotubes (flCNTs). With a wide range of high-performance polymers to choose from as the matrix component, efficient and accurate computational modeling can be used to efficiently down-select compatible resins, drive the design of these composites by predicting interface behavior, and provide critical physical insight into the flCNT/polymer interface. In this study, molecular dynamics simulation is used to predict the interaction energy, frictional sliding resistance, and mechanical binding of flCNT/polymer interfaces for a high-performance

epoxy resin. The results, when compared to the sister studies, indicate that the BMI has stronger interfacial interaction and transverse tension binding with flCNT interfaces, while the benzoxazine demonstrates the strongest levels of interfacial friction resistance. Epoxy dwells in the "Goldilocks" zone with neither superior nor inferior properties. Comparison of these results indicate that BMI demonstrates the best overall compatibility with flCNTs for use in high-performance structural composites.

One critical factor limiting the potential of carbon-based composites in aerospace applications is the poor load transferability between the reinforcement and the polymer matrix, which arises due to low interfacial shear strength at molecular scale. Molecular dynamics (MD) simulations have been employed in several studies that investigate the interface, such simulations are computationally expensive. To efficiently explore and optimize the interfacial design space with the goal of improving the mechanical performance, it is important to develop a machine learning (ML) approach that can be used to assist in the identification of optimal combinations of interface variables. In this study, a MD-ML workflow is proposed to predict optimal functionalization strategies for a bismaleimide (BMI) and three-layer graphene nanoplatelet (GNP) nanocomposite with maximized interfacial shear strength. In turn, these predictions of pull-out force will be used to identify optimal surface functionalizations that maximize the pull-out force. The details on the MD modeling and training data generation for the ML model are discussed in this work.

1 Introduction

Polymer matric composites (PMCs) are increasingly used in the aerospace industry as structural components. Decades of research has shown that the PMCs provide an excellent replacement for the metallic counterparts. These materials provide excellent specific mechanical properties which are critical in the aerospace applications. Additionally, the anisotropic nature of the material is desirable for manufacturing specifically engineered components. Persistent research and development have resulted in significant improvements in the traditional manufacturing processes. As a result, there has been an ever-increasing and a niche supply base which has helped in establishing material standards.

Even with all the advancements there exist inherent drawbacks when using PMCs for highly specialized applications like aerospace. The widely studied shortcoming is the interface between the matrix and the reinforcement [1, 2]. The adhesive nature of the interface results in low compressive strength and the ability to undergo delamination. Along with the mentioned mechanical properties, the thermal properties are also inferior to the required standards. All these limitations stem from the inherent poor properties of the polymer matrices and the adhesive interface. Addressing these shortcomings has been the ongoing research with these materials.

Enhancing the polymer matrices has been researched widely and reports have shown that there are diverse options that can improve the performance of the material. One option is the process modeling of the matrix to enhance the manufacturing process which improves the production quality. Traditional processes rely heavily on the physical experiments and involve trial-and-error type of approach. Another approach focuses on the covalent functionalization of the interface. Covalent functionalization results in degradation of the pristine sp^2 carbon surface of the reinforcement which has some structural advantages [3]. Studies have shown that a balanced approach can help improve the interfacial properties[4, 5].

Exploration of different criteria that improve the material properties is an expensive process. The cost of experimentation and property validation is extremely high since these are special materials with limited supply base. Computational tools have been studied and proved effective with property prediction of PMCs [6-12]. The Integrated Computational Materials Engineering or ICME has been gaining recognition in the research community for its advantages of relying more on computational modeling to drive materials engineering [13]. Also, Molecular Dynamics (MD) has been used to characterize such materials in detail and studies have shown that MD integrates very well with ICME approaches [14]. The use of computational tools not only help with accelerating material design with reliable modeling but also reduce the cost of experimentation and material manufacturing.

The goal of this work is to use molecular modeling to investigate polymer matrix composites' property evolution during manufacturing and characterization of the interface. To be precise, this work is divided into three projects –

1. Process modeling of an epoxy cure – A study investigating the evolution of thermo-mechanical properties of an epoxy matrix during the manufacturing process.
2. Characterization of flattened carbon nanotubes/epoxy interface – A study to predict interfacial properties of CNT-based composite.
3. Design and improve the interfacial strength of graphene/bismaleimide interface – A study utilizing MD and Machine Learning to identify potential functionalization strategy which improves interfacial shear strength of the composite material.

2 Literature Review

2.1 Molecular Dynamics

Molecular Dynamics or MD is a computational used to study material behavior at nanoscale. MD is popularly used to predict thermo-mechanical properties of a wide variety of materials. The strongest feature of MD is the ability to link a chemical structure to the macroscopic material properties. This incentivizes the large design space which by conventional tools is never available to explore.

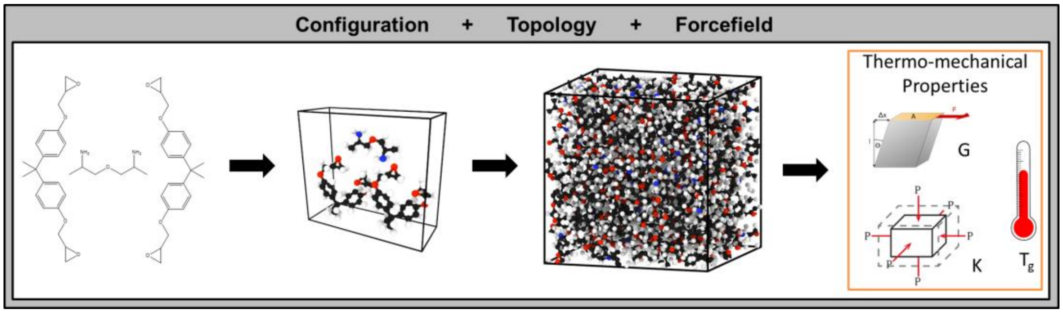

Figure 2.1. Molecular Dynamics workflow

Any MD workflow requires three inputs from the user – Configuration, Topology and Force field [15, 16]. The configuration of the system defines the atomic positions and velocities of individual atoms. Topology of the system defines the chemical description of the system which is the molecular structure of the material. Last is the force field, which is the most vital information; the force field defines the interatomic interaction between atoms. This interaction includes the energy contribution of different bond terms like bonds, angles, and torsion or dihedrals, and non-bonded terms like van der Waals forces, and coulombic charges. With the three inputs available, a MD software simulates atomic trajectories over a period by using an integrative approach which obeys Newton’s second law of motion. Usually, a Verlet algorithm is used to perform time integration. Based on the end condition, the simulation progresses until equilibrium or end of simulation runtime. Figure 2.1 shows the flowchart depicting a standard MD simulation workflow.

Advances in MD simulator design and capabilities, and parameterization of different force fields based on the material chemistry and application has improved the efficacy of the property predictions. The rapid and inexpensive characterization of materials has helped improved reliance on MD. Even with all the advantages, there are certain shortcomings when using MD. MD predictions are made at extremely small length scales and very small time scales. MD simulations with thousands of atoms can be simulated only over a few nanoseconds and the required wall-clock times are several hours depending on the force field and its computational efficiency. Such limitations are usually overcome by different up-scaling techniques like micromechanics and peridynamics.

2.1.1 Force field

Force field is a set of numeric parameters which define interaction between atoms in an MD simulation. These parameters dictate the time evolution of velocities and forces when thermal, physical, chemical, or mechanical conditions are applied on the set of atoms in an MD simulation. There is a variety of force fields available in the literature and their usage depends on the choice of chemistry and the material application under study. In general, the force fields are classified under two primary categories – fixed bond and reactive or bond order force fields.

The fixed bond force fields rely heavily on the topological information provided by the user. The parameter set usually defines key energy terms which control the atomic interactions. Some of these terms include bond potential energy, angle potential energy, dihedral potential energy, van der Waals potential energy, and electrostatic potential energy. For example, the equation governing the bond between two atoms is follows:

$$\mathbf{E} = \mathbf{K}\,(\boldsymbol{r} - \boldsymbol{r_0})^{\mathbf{2}} \tag{1}$$

$$\mathbf{E} = \boldsymbol{K_2}(\boldsymbol{r} - \boldsymbol{r_0})^{\mathbf{2}} + \boldsymbol{K_3}(\boldsymbol{r} - \boldsymbol{r_0})^{\mathbf{3}} + \boldsymbol{K_4}(\boldsymbol{r} - \boldsymbol{r_0})^{\mathbf{4}} \tag{2}$$

Where, K, K_2, K_3, and K_4 are the stiffness constants with units in energy/distance^2 and r_0 is the equilibrium bond distance between the two atoms with distance units. Each of these terms usually follow a harmonic curve wherein the over-stretching of bonds result in unrealistic atomic forces. The Equation (1) falls under class-1 fixed bond force fields. The class-2 force fields maintain the harmonic nature of the curve but include additional cross terms which improve the energy calculations by increasing accuracy and computational efficiency. Equation (2) describes the bond energy of class-2 bonds. Some of the popularly used class-1 force fields are OPLS, AMBER, and CHARMM [17-20]. Some of the class-2 force fields are PCFF, COMPASS, and IFF [21-23]. Every force field is designed for specific materials and specific applications but can be adapted for other applications if the modeled material is well parameterized.

The reactive or bond order force fields do not rely on topological parameters like bonds, angles, and dihedrals. Bond order is assigned to every atom based on distance of neighboring atoms. Every timestep, the bond order is updated which proves to be especially useful to simulate reactive events. Since reactive events heavily rely on bond scission and bond formation, a bond order force field is the only force field that can be reliably used. The Reactive Force field or ReaxFF is the most popular reactive force field which has proved to be very accurate with MD predictions [24]. However, each parameterization of ReaxFF is tailored for specific materials and their corresponding applications. Unlike with the fixed bond force fields, the ReaxFF parameters are not useful when using for any other purpose.

The Reactive Interface force field (IFF-R) is a novel force field which combines the class-2 fixed bond and reactive forcefield by implementing a hybrid bond assignment [25]. The harmonic bonds are converted to Morse bonds which have the capacity to neutralize energy when bonds are over-stretched. Figure 2.2 shows the harmonic and morse bond energy curve as a function of interatomic distance. Unlike the harmonic bond, the morse bond energy converges upon reaching the bond dissociation energy. The bond dissociation energy for different bonds have been studied and there are abundant databases in literature [26]. Recent studies have shown that this force field combines the best features of the two types of force fields. Equation (3) is the governing equation for the morse bonds.

$$\mathbf{E} = \mathbf{D}\left[\mathbf{1} - \boldsymbol{e}^{-\boldsymbol{\alpha}\,(\boldsymbol{r}-\boldsymbol{r_0})}\right]^{\mathbf{2}} \qquad (3)$$

Where, D is the bond dissociation energy, r_0 is the bond equilibrium distance, and α is the well depth parameter which dictates the slope of the morse bond curve at longer bond lengths. Even with all the advanced capabilities, the IFF-R still falls under the class of fixed bond force fields. Hence, complex operations like change in hybridization and new reactive bond formation cannot be achieved without user intervention which is a default feature in ReaxFF. To summarize, the IFF-R is an excellent force field when simulating simple bond dissociation but is limited by the same. Depending on the MD simulation workflow and material application, the choice of force field needs to be thoroughly researched.

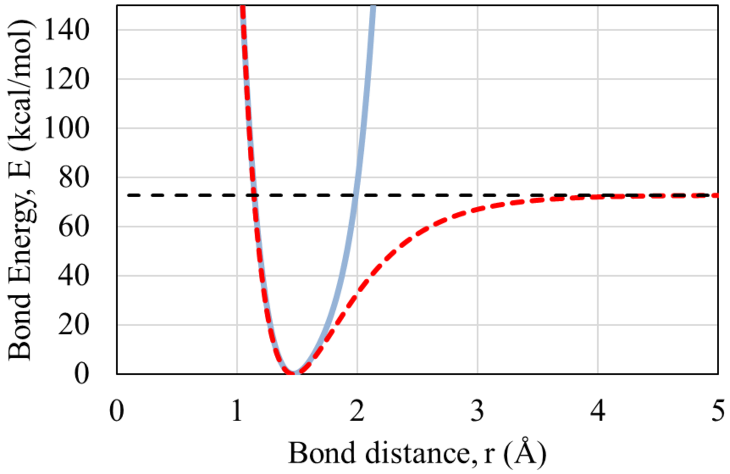

Figure 2.2. Energy curve for a carbon-nitrogen single covalent bond. (blue) The harmonic bond, (red-dotted) morse bond, and (black-dotted) bond dissociation energy [26].

2.2 Flattened Carbon Nanotubes

Carbon nanotubes or CNTs were discovered in 1991 by Sumio Iijima [27]. Since then, there has been a consistent effort to fully utilize their structural and mechanical superiority for varying application in different industries [28, 29]. CNTs are getting more attention for their potential usability in aerospace structures since they exhibit properties ideal for fabricating lightweight yet ultra-strong components (specific modulus of ~1 TPa, specific strength of ≥ 100 GPa) [30].

A recent study conducted at the High Performance Materials Institute of Florida State University, researchers were able to fabricate CNT composite with the bismaleimide (BMI) matrix [31]. In the same study, they were able to boost the composite properties by stretching the CNT bundles unidirectionally. The increase in reported properties included a three-fold increase in Young's modulus and a two-fold increase in the tensile strength. The unidirectional stretching was up to 80% strain and the application resulted in collapsing of the nanotubes. The flattened CNTs were observed, and it was evident that flattening resulted in neighboring CNTs to align and form stacks which helped increase the surface-surface interaction between the stacks. Jolowsky et al. [32] demonstrated a panel-level fabrication of the same material and reported macroscale mechanical properties.

2.3 Machine Learning Application in Atomistic Modeling

Machine Learning or ML methods have gained a lot of traction in this past decade due to the rapid prediction capabilities. Applying an ML algorithm to MD simulation data has been limited to only a studying a few aspects of MD simulations. There are several studies that use ML models to predict certain molecular properties or parameterize newer force fields [33-36]. Chmeila et al. [37] implemented a gradient-domain machine learning approach to develop efficient force fields from ab-initio molecular dynamics simulation data. The key feature of the developed model was its adaptability to newer features like including novel reaction pathways and model scaling to name a few. Another study by Alred et al. [38] focused on applying a ML model to study covalent bonding between CNT atoms and sulfur. With increasing efforts on applying ML concepts in atomistic simulations, there has been fewer efforts toward developing a framework to predict stochastic events like interfacial failure in composites.

A recent study by Rahman et al. [39] developed a surrogate ML model for MD simulations to predict interfacial shear strength in a CNT/epoxy nanocomposite. A convolutional neural network (CNN) was developed which used a radial distribution function to quantify the local chemical environment at the CNT/epoxy interface. The results showed poor accuracy due to limited MD simulation data; however, a novel method was established which could successfully featurize the chemistry in an MD model. With initial benchmarks established, the study can be used to develop higher fidelity models and expand the design space that was initially used.

3 Process Modeling of DGEBA/PEA Cure

3.1 Introduction

Epoxy based polymer matrix composites (PMCs) make-up a substantial part of the primary structure composition in modern aircrafts. These materials have gained increased attention over the course of few decades because of the superior structural properties like specific stiffness and specific toughness. Ongoing research on these materials has helped in refining the current manufacturing processes, lowering of the production costs and establishment of specialized supply base. High-performance thermosetting polymers are class of polymers which are specifically developed for aerospace or similar applications. These materials are typically multi-component blends, however there are some available one-component systems. During the manufacturing process, the thermoset polymers undergo the cure, a chemical reaction, which transforms the material into its final form. During the cure, chemical bonds are formed that generates a crosslinked robust network. This network formation is localized and results in formation of residual stresses [40-42]. This procedure is performed in-situ, and the formation of residual stresses is a direct result of mismatch between the thermal expansion of the polymer and the reinforcement. Presence of such localized stresses is undesirable and hampers the integrity of the structure. Understanding the link between the processing conditions and evolution of the residual stresses is critical to improve the lifecycle of components, especially in high-performance applications.

The chemical transformation during the cure is a nano-scale phenomenon where covalent bonds are formed under specific environmental conditions. To study such nano-scale characteristics, Molecular Dynamics (MD) has been extensively used in the research community [9, 10, 43-45]. MD provides a robust framework to study this transformation by controlling the covalent bond formation and evaluating the property evolution. The accuracy of MD prediction is dictated by the choice of forcefield. Forcefield selection is dependent on the simulated material system, specifically it’s chemistry. For polymers, classical forcefields like AMBER, OPLS, COMPASS, PCFF, and many more have been used to predict thermo-mechanical properties [6, 46-54]. However, a forcefield developed specifically for simulating high-performance polymers has not been studied. The Reactive Interface Forcefield (IFF-R) has been proven to accurately predict properties for such materials [8, 25, 55, 56]. Additionally, this forcefield is known for its accurate atomic charge assignments, which affects the predicted material properties using MD. The classic Reactive Forcefields (ReaxFF) have also been used in MD simulations to predict accurate mechanical properties [9, 11, 43, 44]. In comparison to the classical ReaxFF, this forcefield shows comparable predictions with much better computational efficiency while maintaining the bond topology information [25].

To fully understand the curing procedure and its effect on residual stress evolution, it is important to simulate the cure cycle from the purely un-crosslinked state to the fully crosslinked polymer, including the intermediate crosslink densities. A recent study from Fan et al. [46] reported the thermo-mechanical characterization of a bisphenol-A based epoxy as a function of polymerization. The results reported a significant difference between the MD predictions and the available literature values. Previous work on bisphenol-A based epoxy using IFF-R has shown that the prediction of thermo-mechanical properties shows a perfect match with the available literature values [44, 57, 58]. This work uses a refined methodology of modeling the bisphenol-A epoxy and Jeffamine D230 system using IFF-R forcefield. The physical, mechanical, and thermal property evolution is studied as a function of polymerization progression or the crosslink density. Experimental validation is also performed to support the MD predictions of some of the quantities for the fully cured resin.

3.2 Materials and Experiments

The epoxy resin used in this study is a type of diglycidyl ether of bisphenol A (DGEBA), sold commercially as EPON 828 [59]. Jeffamine D230, a poly(oxypropylene) diamine, was used as a curing agent [60]. The neat resin was supplied by Fisher Scientific International. Huntsman Corporation supplied the curing agent. The chemical structure of EPON 828 has two epoxide groups with an epoxy equivalent weight of 192 g/mol for each epoxide group as illustrated in Figure 3.1(a). Jeffamine D230 has a general chemical structure presented in Figure 3.1(b) where n = 2.5 and has a molecular weight of 230 g/mol [61].

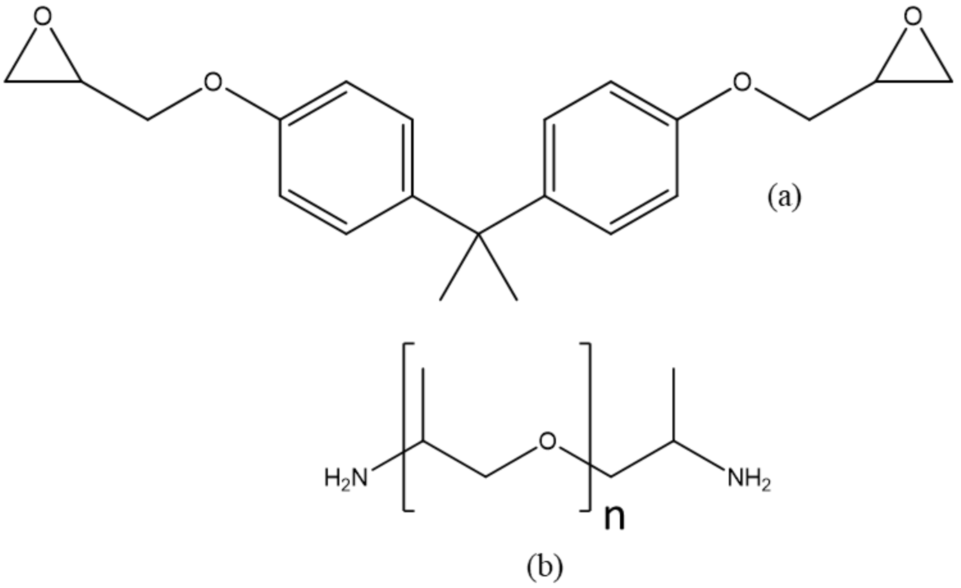

Figure 3.1. Molecular structures of (a) Diglycidyl ether bisphenol-A (DGEBA) and (b) Polyether amine (PEA). Where *n* is the number of repeating units.

EPON 828/Jeffamine D230 epoxy samples were manufactured using an open molding method. A total of four speedmixer cups were each charged with 66.7 g of EPON 828 epoxy resin and 21.2 g of Jeffamine D230 curing agent. The Speedmixer cups were then mixed in a Speedmixer at 2000 rpm for 5 minutes at 25 °C and then heated to 50 °C in a vacuum oven. Cups were degassed in the vacuum oven at 50 °C for 30 minutes at 1 atm vacuum pressure. The resin system was cast into a steel open mold assembly that produces 6.5” long bars 0.75” wide. The resin was degassed once more for 30 minutes at 50 °C and at 1 atm vacuum pressure. The oven temperature was then raised to 80 °C and held for 5 hours. Then the oven was turned off and the system was allowed to cool overnight back to room temperature.

Mass density measurements were taken on the cured resin system according to ASTM D792, which uses the buoyancy force of a sample of known mass submerged in a liquid of known density to calculate the mass density of the sample. Test samples were cut from a bar using a vertical band saw so that the geometries of test samples were 1.5” long, 0.5” wide, and 1/8” thick. A beaker of water was placed on a stand located over the balance. A sample holder that reaches above and over the beaker was clipped to the edges of the balance plate and a sample hanger was immersed into the beaker. The sample was placed on the upper dry plate located at the top of the sample hanger and a dry mass measurement was taken. The sample was then placed on the lower submerged plate. The mass density of the sample was calculated using Equation (4), where ρ is density, a is mass of dry sample, and b is mass of the immersed sample.

$$\boldsymbol{\rho_{sample}} = \frac{\boldsymbol{a}}{\boldsymbol{a-b}} * \boldsymbol{\rho_{water}} \tag{4}$$

Specimens were assessed for tensile properties at 23°C according to ASTM D638 and using the ASTM Type I sample geometry: 6.5” long and 1/8” thick. A Ceast router was used to grind the specimens into dog-bone shaped samples with a width of 12.7 mm in the gage region. Eight samples were assessed at a crosshead rate of 1 mm/min using an Instron 4206 screw-driven mechanical testing machine. Stress values were recorded by the testing machine and a 2” axial extensometer from Epsilon Technology Corporation was used to collect elongation data from which the axial strain was calculated. The tensile modulus was determined from the initial slope of the stress-strain curve. The yield stress was determined by drawing a second stress strain curve offset by 0.2% strain in the form of a straight line with the slope equal to the slope of the elastic region for the experimental stress-strain curve. The yield stress is determined by locating where the offset line crosses the experimental curve. The poisons ratio is determined by locating the ratio of the axial strain to the transverse strain in the elastic region of the stress strain curve.

3.3 Molecular Modeling

The details of MD simulations are discussed in this section. The Large-scale Atomic/Molecular Massively Parallel Simulator (LAMMPS) software package, version June 2018, was used for performing all the MD simulations in this paper [62]. Like other molecular dynamics code, LAMMPS uses various interatomic potentials depending on the studied material system. The IFF-R forcefield was used to simulate the interatomic interactions. This forcefield uses “hybrid” style bond description which comprises of both harmonic and morse potentials. The availability of morse potential provides a pathway to simulate bond scission, which can prove useful for deformation simulations [25].

3.3.1 Materials and Stoichiometry

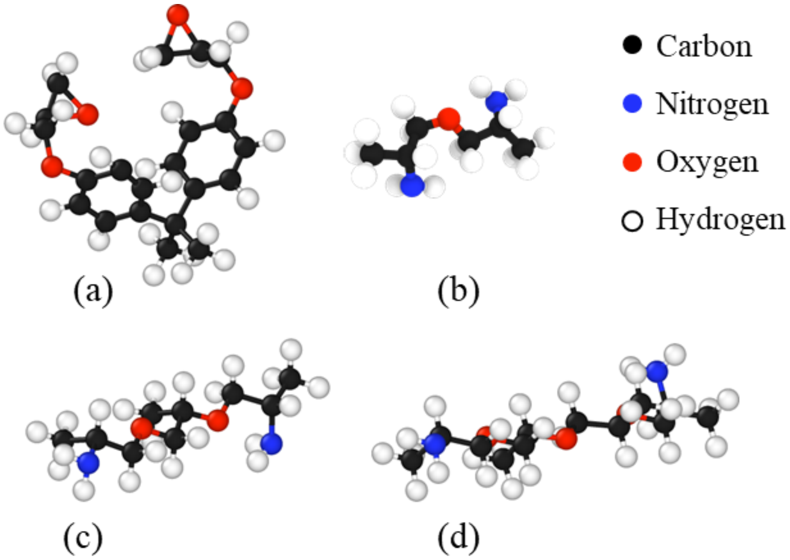

Figure 3.2. Molecular models of (a) DGEBA, (b) PEA with n = 1, (c) with n = 2, and (d) with n = 3.

Figure 3.2 shows the molecular models of the (a) epoxy and (b), (c), (d) three variations of polyether amine or PEA monomers. The images were generated using the visualization software OVITO [63]. Two structures of PEA with different molecular weight were modelled, one was the generic structure with n = 1 and the other was the accurate composition of D230 Jeffamine curing agent. For the D230 structure, the smaller monomer (n = 2) consisted of two repeating units and a molecular weight of 190. The larger monomer (n = 3) had three repeating units and a molecular weight of 248. To match the experimental molecular weight, the two monomers were mixed to obtain the average bulk molecular weight of 230 [61]. The epoxy monomer was mixed with the D230 monomers in a stoichiometric ratio of 38:6:13 where the simulation box contained 38 monomers of epoxy for 6 monomers of n = 2 and 13 monomers of n = 3. The other system consisted of 2:1 mixture of epoxy monomers with the PEA (n =1).

3.3.2 Model Setup

The following steps demonstrate the MD simulation setup of the neat epoxy/PEA system. All the simulations were performed using the periodic boundary conditions, and the Nose-Hoover thermostat and barostat with “aniso” settings [64-67]. To account for statistical variation, five identical replicates were built with different initial velocities for both the systems. For clarity, throughout the chapter, the system with the accurate composition of D230 will be referred to as epoxy/D230 and the other system will be referred to as epoxy/PEA.

The single individual monomers were arranged in form of arrays in a simulation box with the stoichiometric ratio mentioned in section 3.3.1. To obtain the stable molecular configuration, molecular minimization simulation was performed using the conjugate gradient algorithm [68].

To generate the bulk system, the monomers were replicated with the total atom count of 21,256 in case of epoxy/D230 and 4428 in case of epoxy/PEA. The initial density of the model was in the range of 0.09 – 0.10 g/cm^3. To effectively mix the three sets of monomers, a short mixing simulation was performed by ramping the temperature down from 600 K to 300 K over 100 ps. The timestep of 1 fs and NVT ensemble was implemented.

The simulation box was first deformed to density of 0.4 g/cm^3 to bring the molecules closer. Next the simulation box was slowly compressed in all directions to densify the system. The deformation was performed with the target density of 1.16 g/cm^3 and a constant deformation rate of 3 Å/ns over 4 ns. During the deformation, intermediate minimization steps were implemented every 0.2 ns to promote optimized molecular configurations. Figure 3.3 shows the implementation of densification process.

An annealing simulation was performed to obtain close packing of the monomers. This step was important to maximize the bond formation during the polymerization simulation. In this step, the system temperature was ramped down from 600 K to 400 K with a constant cooling rate of 50 Å/ns using the NPT ensemble and a timestep of 1 fs.

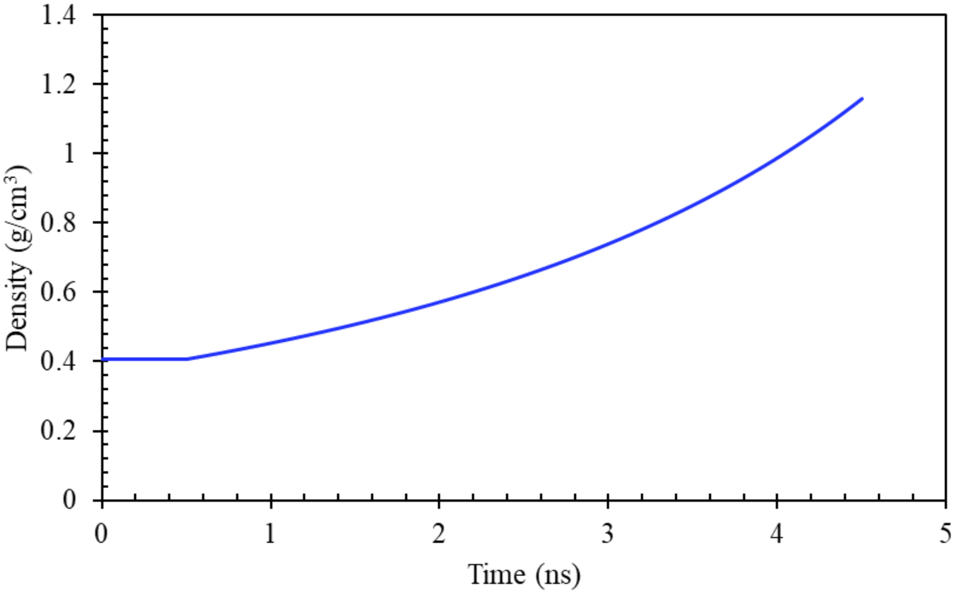

Figure 3.3. Density progression during the deformation simulation.

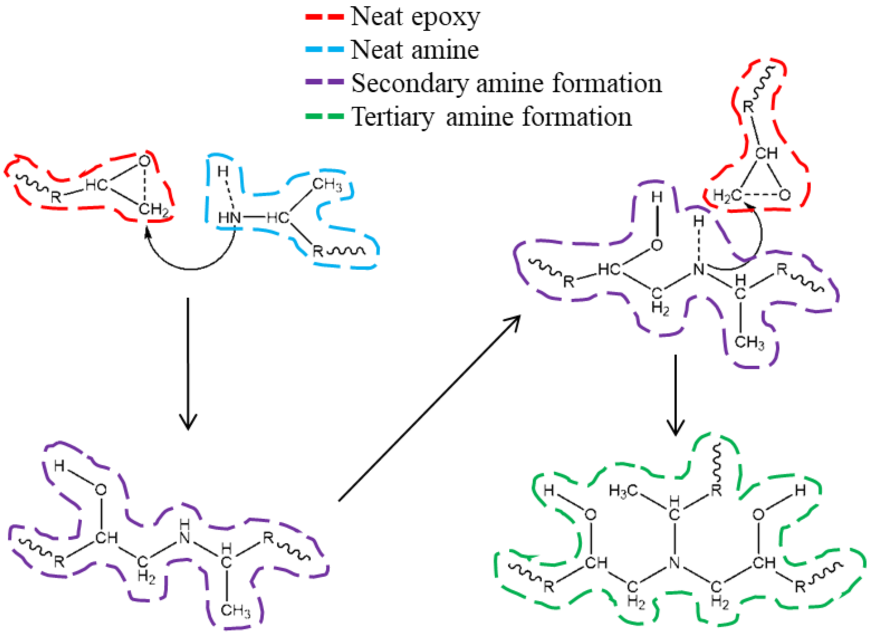

Figure 3.4. Two-step polymerization reaction for epoxide-amine functional groups. The dotted bonds represent the reactive bonds. Dotted bonds represent the reactive bonds that dissociate during the crosslinking.

The annealed models were polymerized virtually using the REACTER protocol as demonstrated by Gissinger et al. [69, 70]. This tool provides highly reproducible procedure for crosslinking the polymers. Additionally, the ability to control the number of new bonds formed is of particular importance. Figure 3.4 shows the two-step polymerization of the epoxy-amine cure reaction. The two-step bond formation was achieved by setting the bond formation cutoff distance in the range of 4 - 6 Å and probability of bond formation in between 0.00002 – 0.5 %. With the increasing bond formation, the cutoff and probability were slowly increased. Using the REACTER tool, user-defined crosslink densities were obtained. In this case, the crosslink density is defined as the percent of newly formed bonds from the total possible new bonds. Intermediate crosslink densities of 5 – 95% in intervals of 5 % were generated. The simulations were performed using 1 fs timestep and NVT ensemble at 400 K temperature. Figure 3.5 shows the amine conversion for all crosslink densities in epoxy/D230 models. To promote maximum conversion, the tertiary amine formation was prioritized during each simulation for all the models. Each crosslink density refers to a separate model, and a total of 21 models per replicate were developed for each system.

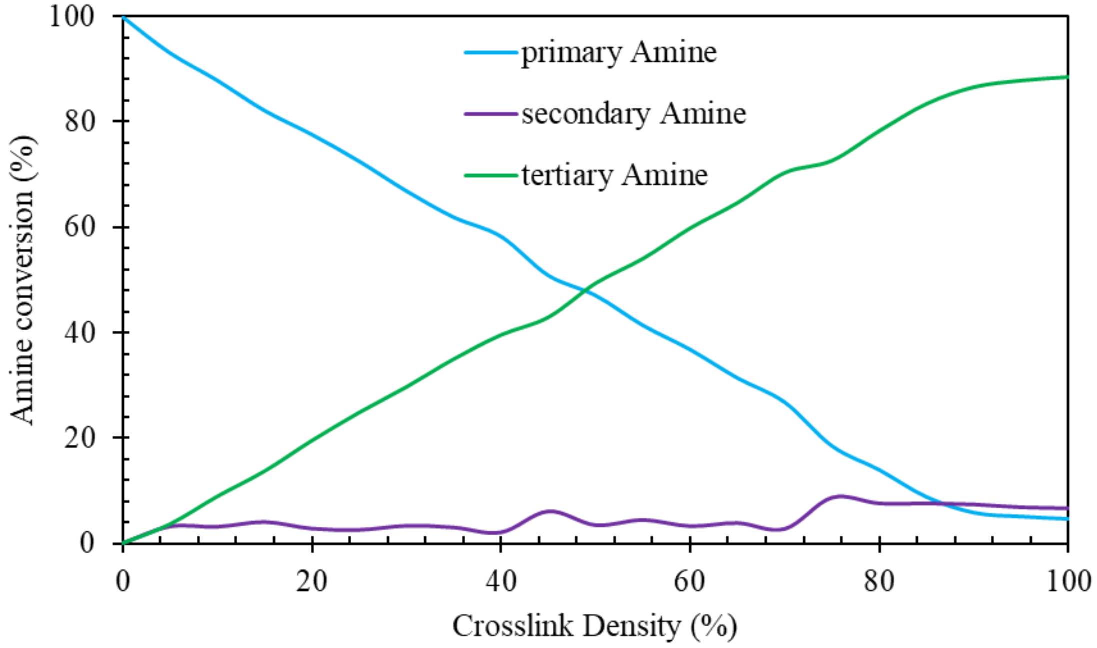

Figure 3.5. Amine conversion for different crosslink densities.

After polymerization all the models were re-annealed to allow the new networks to reconfigure to their optimal orientation. The simulation settings were identical to that mentioned in earlier paragraph except for the timestep which was varied between 0.1 – 1 fs.

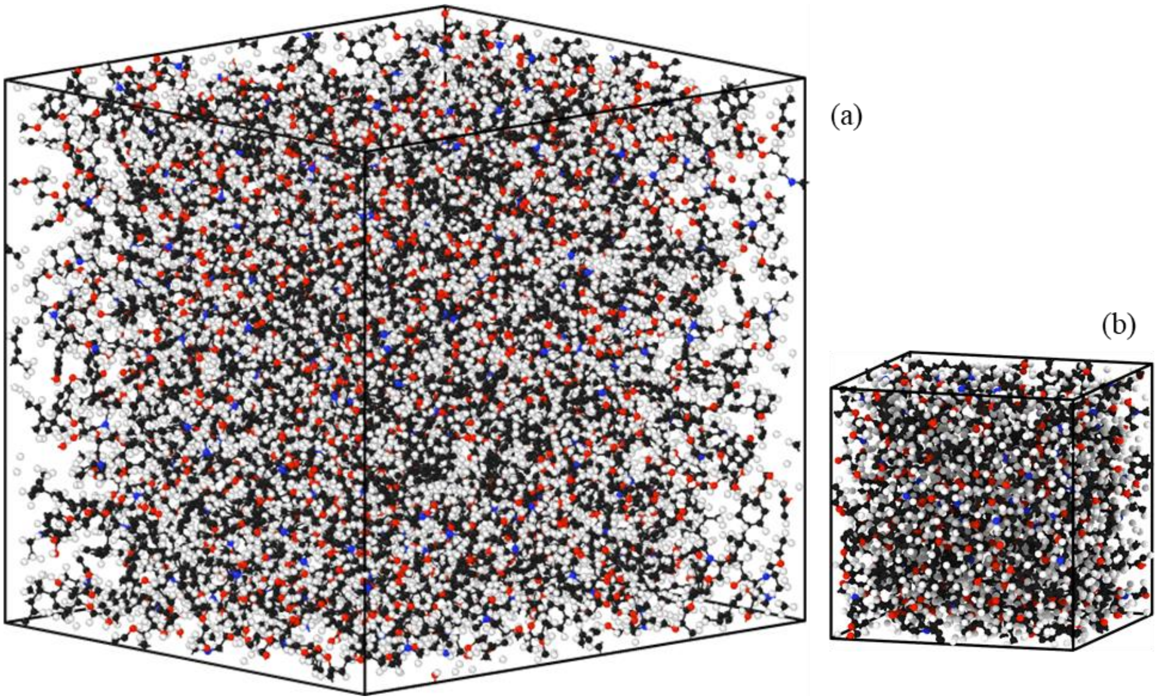

Figure 3.6. Representative MD models of (a) Epoxy/D230 and (b) Epoxy/PEA.

The annealed models were equilibrated using the NPT ensemble at 300 K temperature and 1 atm pressure. The simulation run time was 2 ns with a 1 fs timestep. Figure 3.6 shows the representative MD model of the epoxy/D230 and epoxy/PEA with maximum crosslink density. The fully equilibrated models were used to run the mechanical deformation and thermal simulations.

3.3.3 Gel Point and Network Characterization

The theoretical gel point of a polymer depends on the formation of very large molecules during the crosslinking process [71]. To establish the formation of such molecules, there are established methods in MD that were implemented in this study [72, 73]. These three metrics were investigated for the five replicate systems. The metrics used are the molecular mass of the largest molecule (primary chain or p-Chain), molecular mass of the secondary molecule (secondary chain or s-Chain) and the reduced molecular mass of the model (RMW). The RMW is the average molecular mass of the system minus the mass of the largest molecule. Figure 3.7 shows a representative plot of the three metrics which are computed at every crosslink density for the epoxy/D230 system. The inflection point of the molecular mass of p-Chain curve indicates the gel point of the model. The peaks of molecular mass of s-Chain and the RMW are an indicator of the gel point for the model. The predicted gel point of the epoxy/D230 system was at 55.2 ± 5.4 % for the all the three metrics and that of the epoxy/PEA system was at 62.0 ± 2.7 %.

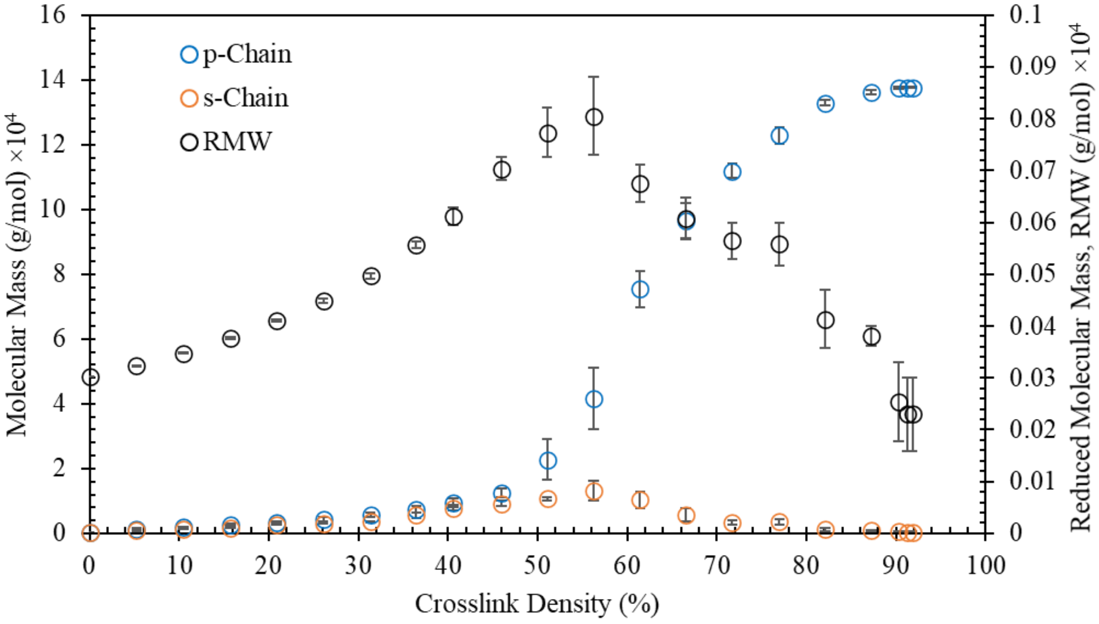

Figure 3.7. Representative plot for gel point prediction for epoxy/D230 system using the three metrics with p-Chain and s-Chain on primary Y-axis and RMW on secondary Y-axis.

The physical interpretation of the gel point using MD can be performed by conducting network characterization. OVITO [63] was used to observe the evolution of individual networks as the crosslinking progressed. Cluster Analysis tool isolates every unique network based upon bond topology information from the LAMMPS data files. Using this tool, Figure 3.8 was generated. Figure 3.8 clearly shows the largest network or cluster consumes the secondary clusters as global crosslink density approaches 100%. The instance when this cluster completely spans the simulation box is an indicator that the system will be able to resist loading. This criterion can be used to qualitatively classify gelation point using MD simulations.

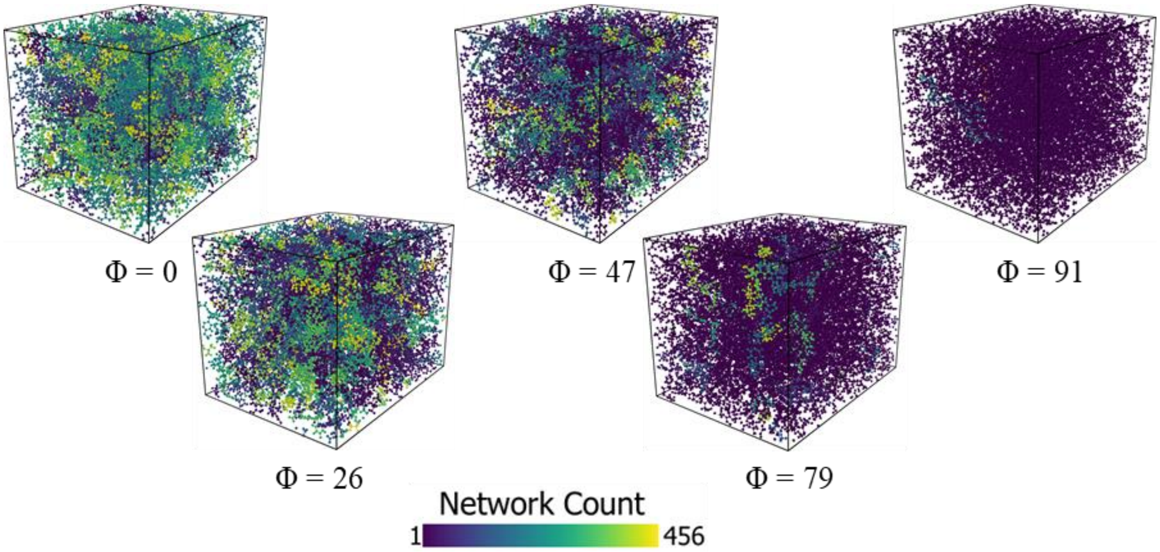

Figure 3.8. Cluster analysis showing the evolution of the individual networks, where Φ is the crosslink density (%).

3.3.4 Property Simulations

The density and volumetric shrinkage were obtained from the equilibration simulation. Time averaged density and box volume over 1 ns was used to compute the system density and volume. To obtain the bulk modulus, the models were subjected to high hydrostatic pressure of 5000 atm at room temperature using NPT ensemble and the corresponding volume was compared to that from the equilibration simulation. The bulk modulus was calculated as described in detail elsewhere [50]. To obtain the shear modulus, the simulation box was converted to triclinic by running a 0.5 ns simulation using NPT ensemble. Next, shear deformations were performed in the XY, XZ and YZ plane direction. These simulations were performed at room temperature with a strain rate of 2×10^{8} s^{-1}. OriginPro software was used to analyze the stress-strain data and compute the shear modulus [74].

Young’s modulus and Poisson’s ratio was calculated from the predicted bulk and shear moduli using the homogenous equations for isotropic materials [75]. Odegard et al. [8] explained a detailed procedure to compute the yield strength from shear deformation simulations. The same approach is implemented in this work. The last set of simulations were the thermal simulations of heating and cooling. For both the simulations, the simulation box was subjected to thermal gradient with the terminal temperatures of 550 K and 250 K. The temperature range was selected such that the material glass transition temperature would lie in the middle of the range. The simulations were performed using NPT ensemble with a constant cooling and heating rate of 50 K/ns.

3.4 Results

This section details the physical and mechanical property predictions. The error bars in all the graphs represent standard deviation associated with the five replicates. The displayed trendlines and R^2 values are to provide clear trends on the property evolution and do not bear any physical significance. Experimental validation of the predicted values is provided for fully polymerized models which includes values from the literature.

3.4.1 Density

Figure 3.9 shows the mass density predictions for all the models as a function of the crosslink density at 300 K temperature. For the fully polymerized models, the MD predicted density for the epoxy/D230 system is 1.153 ± 0.002 g/cm3. The plot in Figure clearly shows a non-linear trend with the increasing crosslink density. The plateauing of the curve beyond 50% crosslink density can be attributed to the gel point prediction discussed in section 3.3.3. Beyond the gel point, the network resists volumetric change and hence a constant value for density is observed. The experimental values from the literature and obtained from this work is plotted at in correspondence to the maximum crosslink density only to signify the values at full cure. Experimentally, the calculated density was 1.155 ± 0.001 g/cm3 for the ten tested samples. The MD predicted values show a perfect match with the experimental values and with the available values from the literature [76-78]. In comparison to previous MD studies, the density predicted using IFF-R are more accurate which is beneficial to understand the evolution of all the properties [46, 48, 51, 79]. For the epoxy/PEA models, the predicted densities were significantly higher than the experimentally reported values. Since the chemistry of the epoxy/PEA models is not accurate hence the over prediction is to be expected.

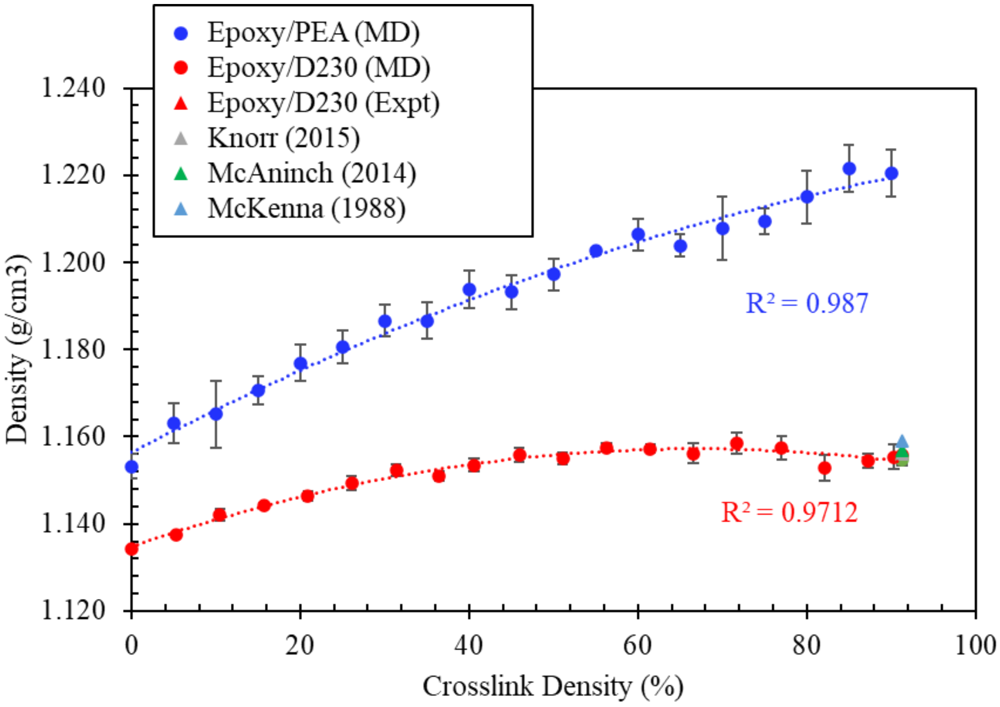

Figure 3.9. Density prediction for different crosslink densities.

3.4.2 Volume Shrinkage

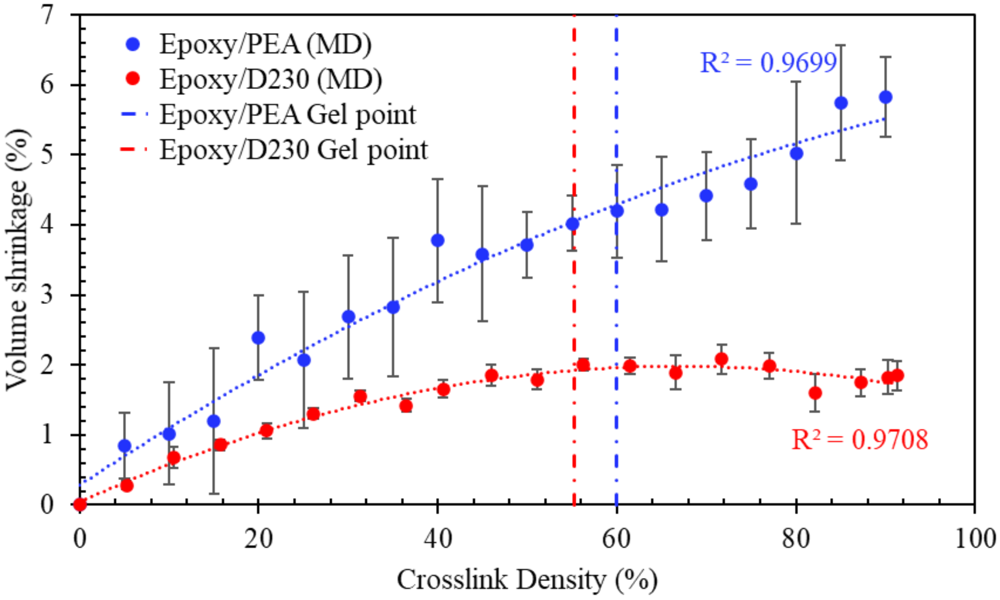

Figure 3.10. Total volumetric shrinkage prediction at each crosslink density.

Figure 3.10 shows the change in volume or volumetric shrinkage as the crosslinking progresses, and the trend clearly shows a non-linearity as the crosslink density crosses 50%. The MD predicted total shrinkage for fully crosslinked epoxy/D230 models at 300 K temperature is 1.63 ± 0.34 %. Figure 3.11 shows the predicted post-gelation shrinkage, and it shows a linear increase as the models approach maximum crosslinking. The post-gelation shrinkage observed for the maximum crosslinked model was 0.43 ± 0.35 % which is negligible compared to the available data in the literature for the EPON 828 resin [80]. However, any form of shrinkage predictions for this exact resin formulation are not available in the literature. For the epoxy/PEA models, the volumetric shrinkage prediction was significantly higher. However, the evolution of shrinkage still follows a nonlinear trend.

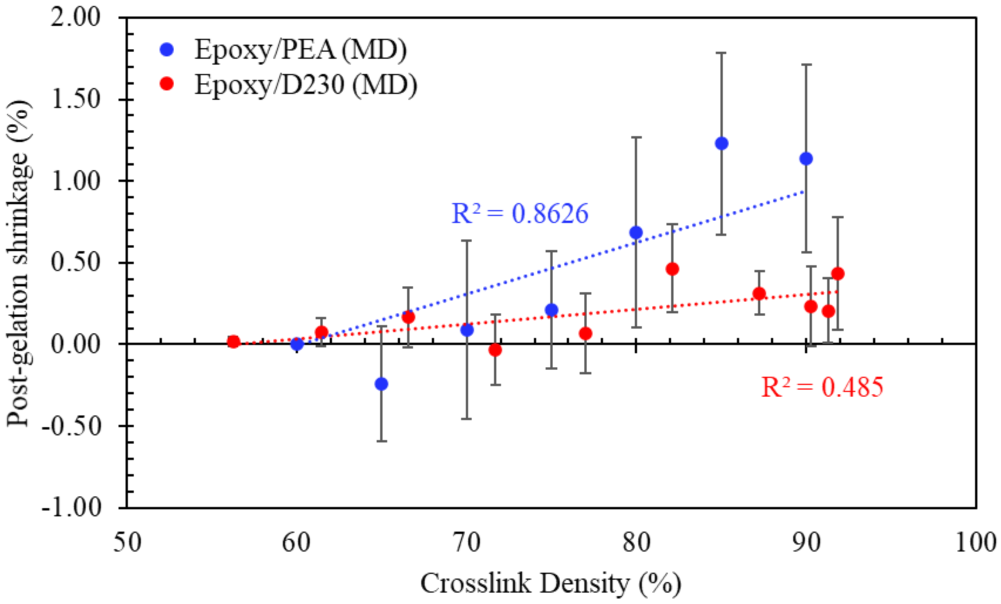

Figure 3.11. Post-gelation shrinkage prediction at each crosslink density beyond gel-point.

3.4.3 Bulk modulus

Figure 3.12 shows the bulk modulus as a function of the crosslink density at 300 K temperature. The evolution of bulk modulus for both the systems is also non-linear with the pre-gelation increase being significantly higher than post-gelation. After gelation, the polymer network becomes dense enough to carry load, hence addition of more crosslinks has less effect on the trend. The bulk modulus value for fully crosslinked epoxy/D230 models was predicted to be 6.38 ± 0.04 GPa. Experimental validation of bulk modulus is not available for any polymeric materials. However, this result will be used to predict the Young's modulus and the Poisson's ratio, which are validated.

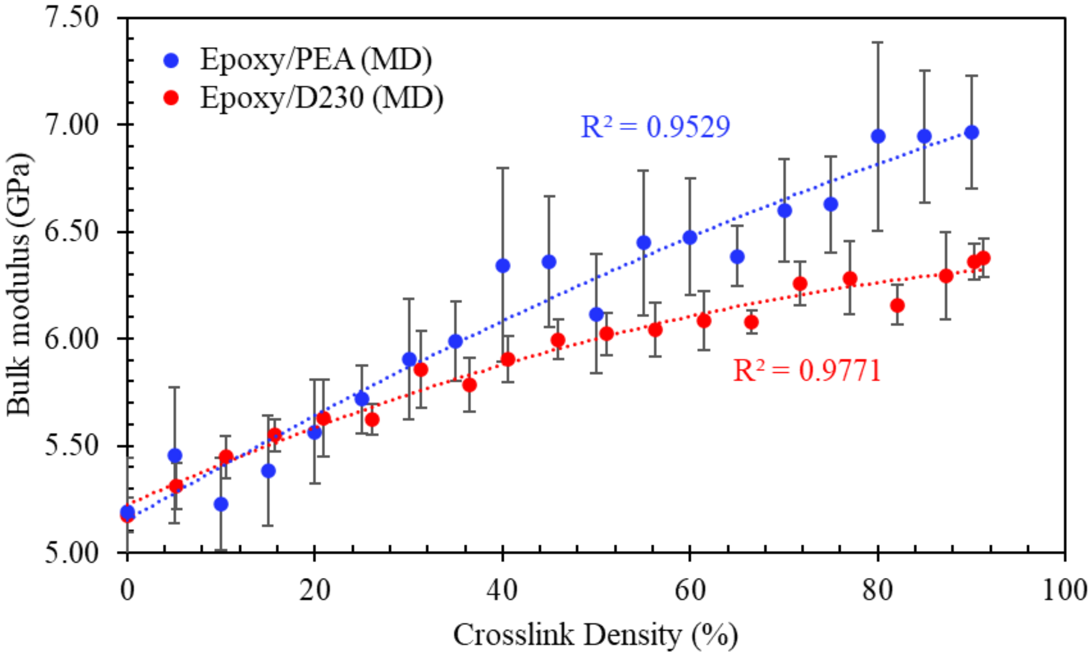

Figure 3.12. Predicted bulk modulus at different crosslink densities.

3.4.4 Shear modulus

Figure 3.13 shows the predicted shear modulus as a function of crosslink density at 300 K temperature. The trend shows a linear rise in the shear modulus for both the systems with the progression of crosslinking. For the fully crosslinked epoxy/D230 models, the predicted shear modulus was 1.18 ± 0.10 GPa. Unlike with the bulk modulus evolution, the shear modulus steadily increases with the increasing crosslink density.

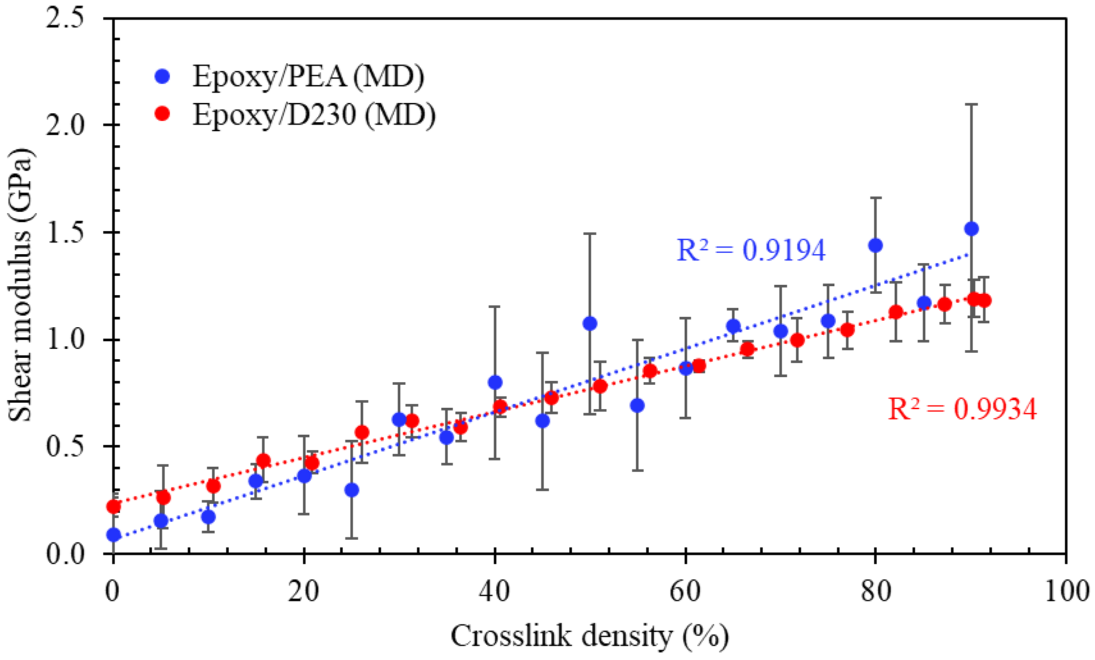

Figure 3.13. Predicted shear modulus at different crosslink densities.

3.4.5 Young's modulus

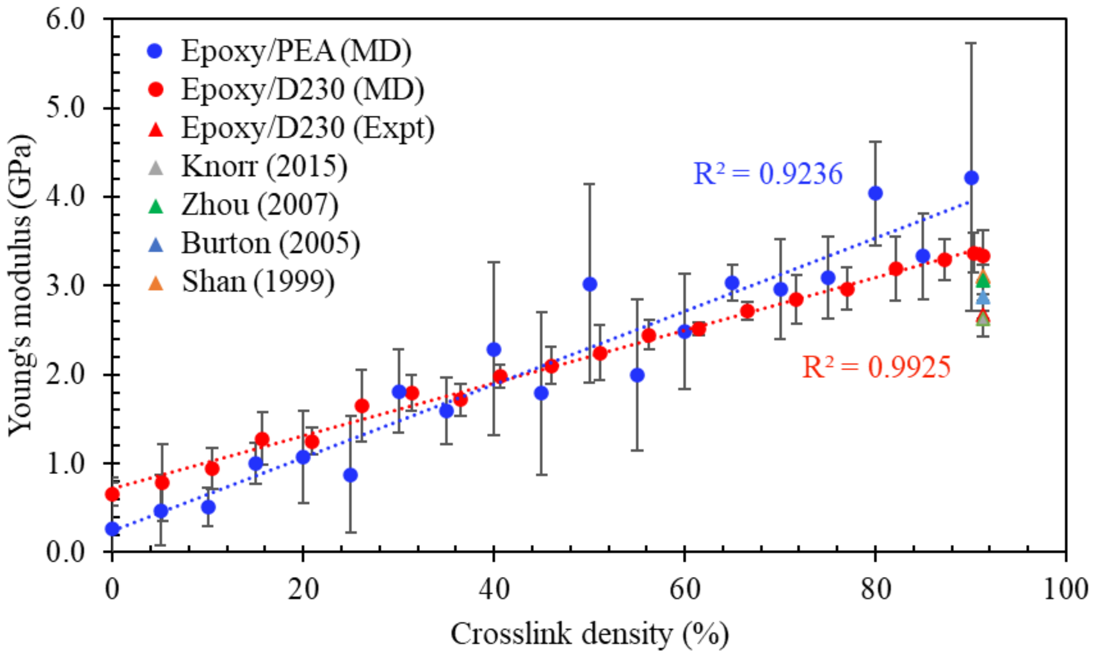

Figure 3.14. Young's modulus as a function of crosslink density.

Figure 3.14 shows the predicted Young's modulus with increasing crosslink density. The Young's modulus clearly shows a linear increase with the crosslink density progression for both the systems. For fully crosslinked epoxy/D230 models, the predicted Young's modulus was 3.34 ± 0.28 GPa. In comparison, the experimentally calculated value of the ten fully cured samples was 2.67 ± 0.04 GPa. The experimental results and other literature values clearly indicate the MD predictions are slightly above the reported values for this resin [61, 76, 81, 82]. This over-prediction is a result of the high strain rates that are implemented in MD simulations. A strain rate of 10^8 s^{-1} magnitude was used for all the deformation simulations, whereas the experimental value was 10^{-5} s^{-1}. All the literature values are reported at 10^{-5} s^{-1} strain rate. The epoxy/PEA models over predicted significantly with no experimental data to validate and therefore further analysis was not performed.

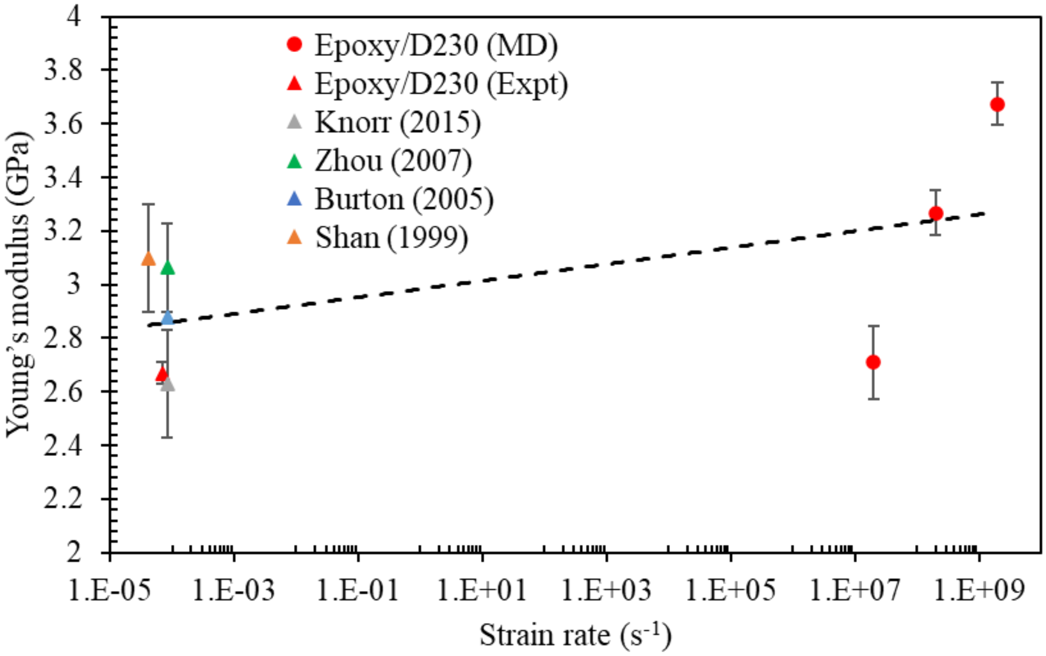

Figure 3.15. Young's modulus as a function of the strain rate.

To perfectly capture the strain rate effect, additional simulations were performed on fully crosslinked models of epoxy/D230 system. The two new strain rates were 2×10^7 s^{-1} and 2×10^9 s^{-1}. Figure 3.15 shows the Young's modulus prediction at higher strain rate and the experimentally calculated values at the corresponding strain rate. When comparing the MD predictions with the available data from experiments and the corresponding strain rates, a logarithmic trend was observed. This trend can be used establish a statistical relationship between the MD predictions at higher strain rates and the experimental calculations at lower strain rates.

3.4.6 Poisson's ratio

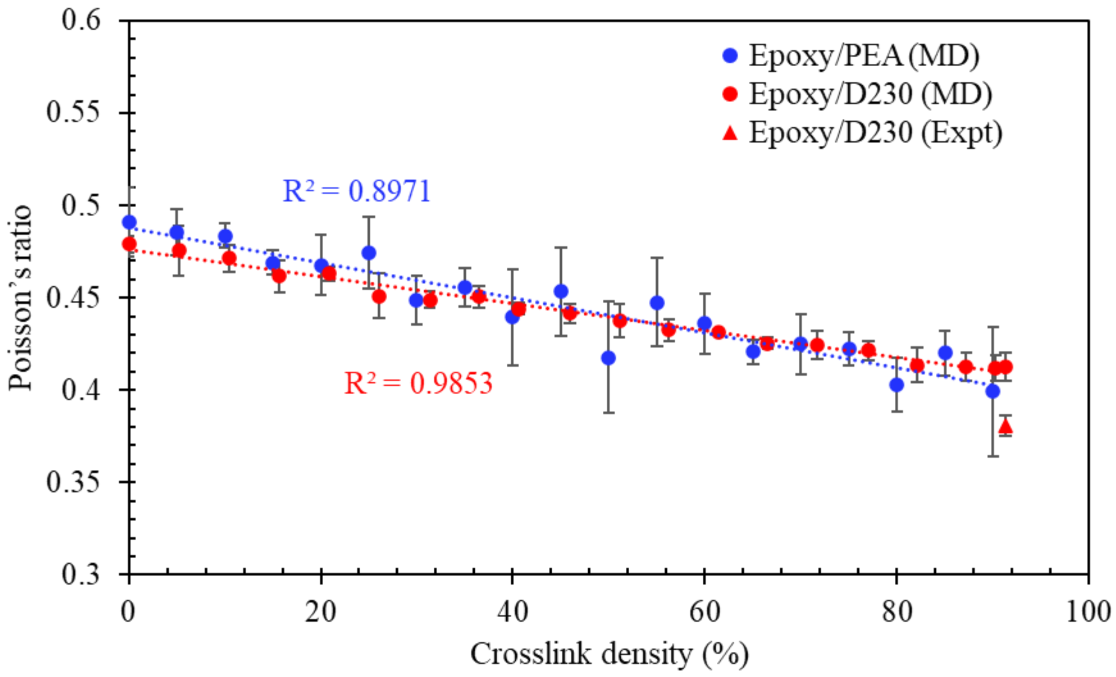

Figure 3.16. Poisson's ratio for different crosslink densities.

Figure 3.16 shows the Poisson's ratio prediction as a function of crosslink density for both the systems. The predicted value for fully crosslinked epoxy/D230 models was 0.41 ± 0.01. At 0% crosslink density, the values obtained were 0.48 ± 0.00. For liquid materials, the expected value of Poisson's ratio is equal to 0.50 which validates our predictions for 0% crosslink density [83]. The experimental results show an average value of 0.38 ± 0.01 which is remarkably close to the predicted values. For the other system, experimental validation was not available. In general, the Poisson's ratio shows a linear decrease in value with the increasing crosslink density.

3.4.7 Yield strength

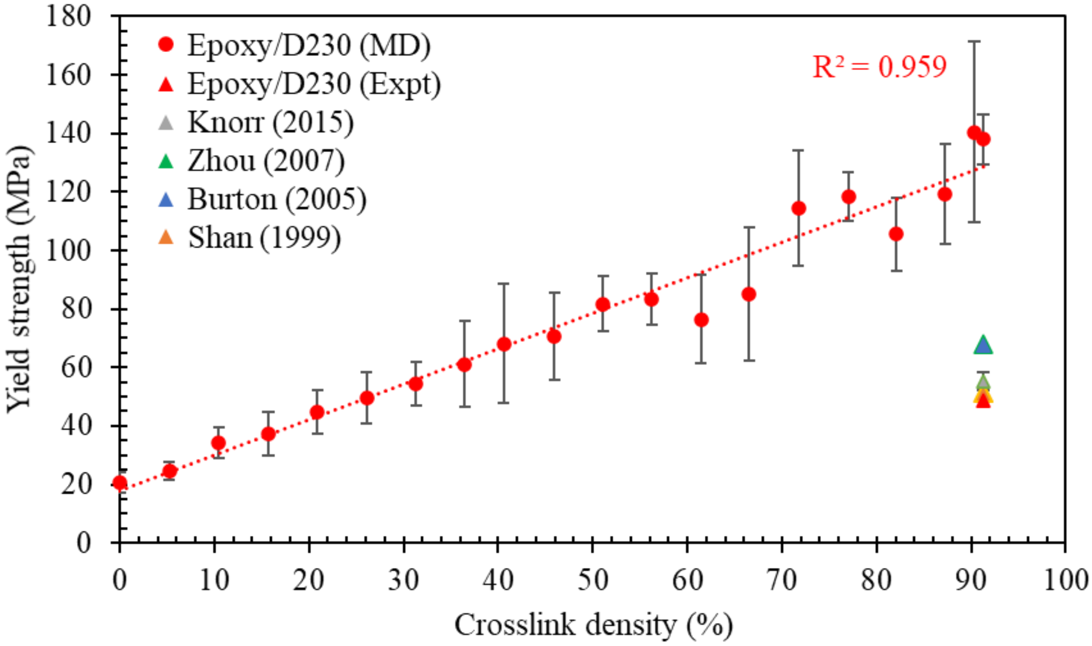

Figure 3.17. Predicted yield strength at different crosslink densities.

Figure 3.17 shows the yield strength predictions for the different crosslink densities for the epoxy/D230 models. The yield strength shows a linear increase with the increasing crosslink density. For the fully crosslinked models the predicted yield strength was 138.1 ± 8.6 MPa. The experimentally measured value across ten samples was 48.7 ± 0.5 MPa. Compared to the Young's modulus, the strain rate effect is much stronger in yield strength predictions. Because yield is computed at much higher strain than the modulus, the strain rate effect is much stronger. The experimental measurements agree with the previously reported values [61, 76, 81, 82]. Yield strength was not computed for the epoxy/PEA models since the computation is complex and validation is unavailable.

Figure 3.18 shows the predicted yield strength of the fully crosslinked models at three different strain rates and the experimentally reported values at the corresponding strain rate. Like the Young's modulus, the disparity in the predictions and the available experimental values is significant. However, the logarithmic curve fit provides statistical link between the computational strain rates and the experimental strain rates.

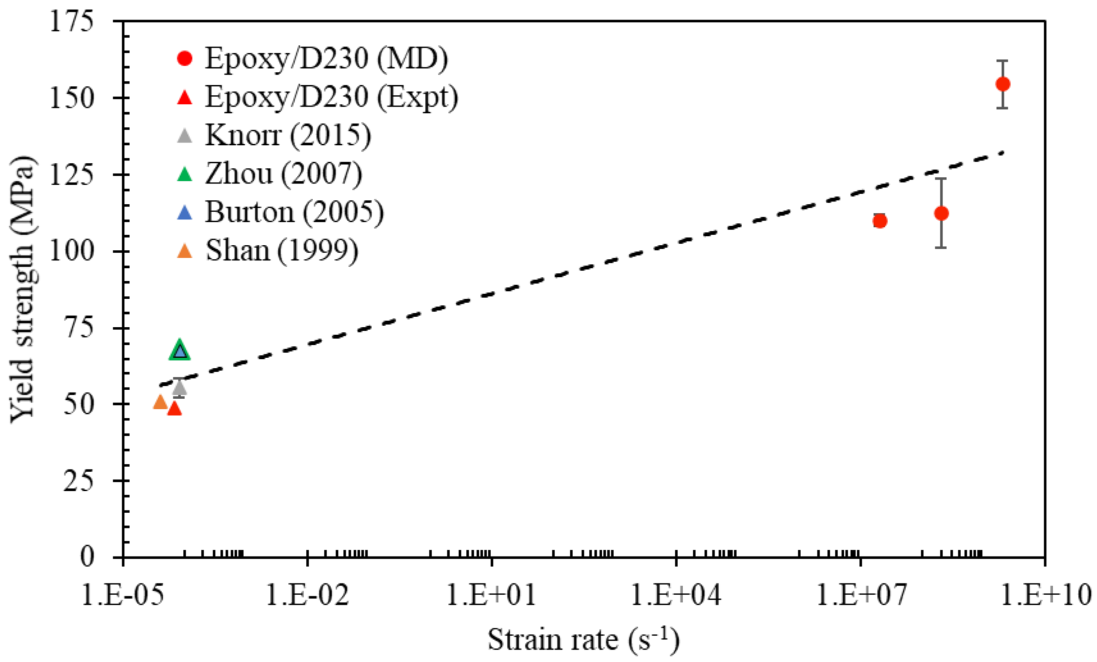

Figure 3.18. Yield strength as a function of the strain rate.

3.4.8 Glass Transition Temperature

Figure 3.19 shows the MD prediction of the glass transition temperature or T_g of the epoxy/D230 system for varying crosslink densities. The T_g increases non-linearly with the progressive crosslinking and converges as maximum conversion occurs. The predicted value for fully crosslinked models was 88.4 ± 21.9 ^{o}C. The experimentally measured T_g was 99.8 ± 0.3 ^{o}C. The MD prediction lies well within the standard deviation of calculated value. When comparing to literature reported values, the prediction shows good agreement with all the values [61, 76, 77, 84, 85]. With all the thermal simulations the standard deviations observed were large due to few models not providing accurate results. All the outlier data points were included to report all the MD simulation data. However, to lower the standard deviation, either the outlier data points need to be excluded from the computation or reconstruct new models and rerun all the MD workflow. The second approach being the most appropriate step, is the most computationally expensive. Comparing the results from this study with available MD-based studies in the literature, it is evident that IFF-R does a better job with the prediction [46, 48, 79].

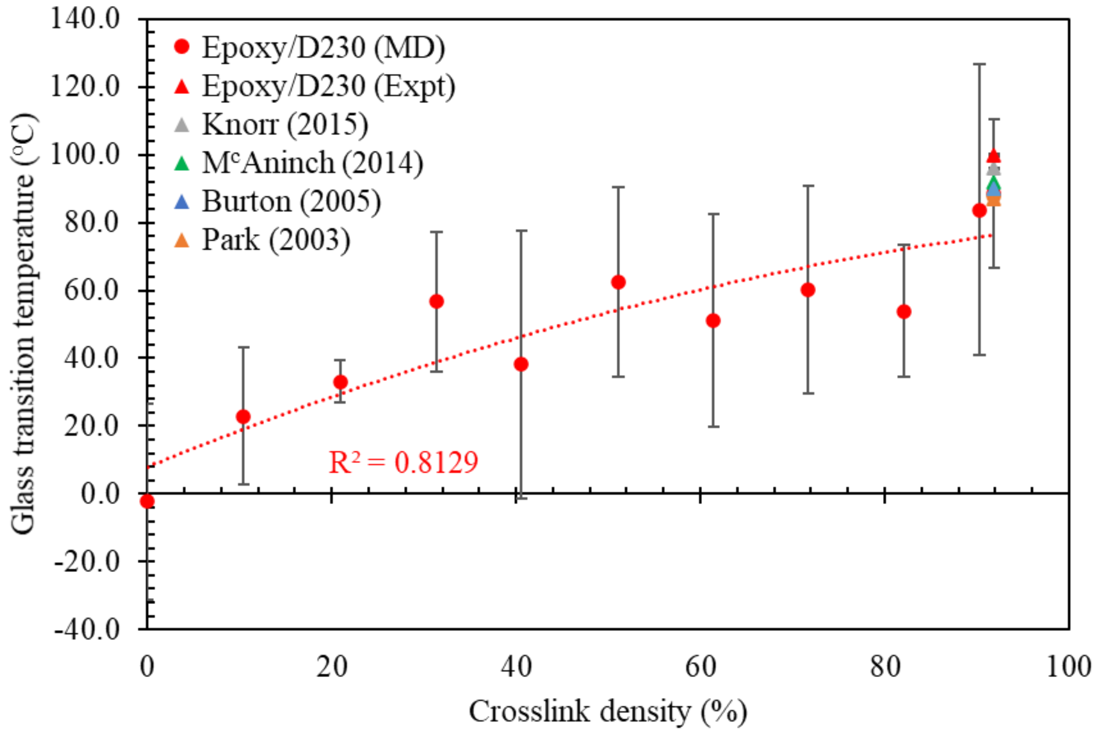

Figure 3.19. Glass transition temperature for different crosslink densities.

3.4.9 Coefficients of Thermal Expansion

Figure 3.20 shows the MD prediction for coefficient of thermal expansion or CTE, above and below the T_g, as a function of the crosslink density. Both the CTEs show a linear decline with the increase in the crosslink density. For the CTE below T_g the predicted value for fully crosslinked models was $6.49 \pm 0.42 \times 10^{-5}$ /K. Comparing the predictions with the literature data the results indicate a good agreement with the reported values [76, 85, 86]. For the CTE above T_g the predicted value for fully crosslinked models was 8.19 1.32 10-5 /K. There is significant underprediction with the above T_g CTE values [76, 85, 86]. In the above T_g region, the thermal sensitivity is quite high due to higher temperatures. Due to the increased stochastic response the accuracy of prediction is directly affected and results in the underprediction of the properties.

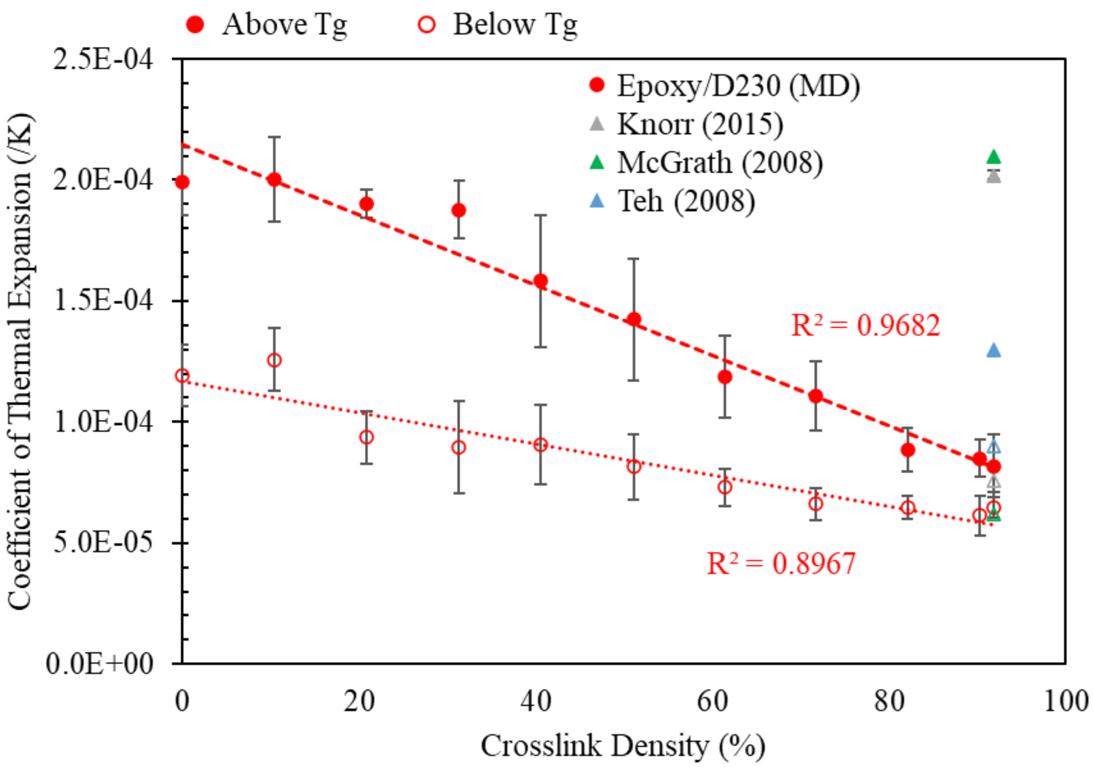

Figure 3.20. Coefficient of thermal expansion (both above and below T_g) at different crosslink densities.

3.5 Conclusion

The results of this study indicate that the mass density, shrinkage, the mechanical, and thermal properties of a Bisphenol-A based epoxy and a linear chain amine hardener show a definitive trend at distinct stages of crosslinking, especially in the pre-gel point region. The use of IFF-R produces validated results which verifies the obtained evolution trends. The MD predicted quantities generally agree with the experimentally measured and literature properties except for the strain dependent properties which are over-predicted. The accuracy in prediction is also attributed to the accurate modeling methodology with the epoxy/D230 system. The study by Odegard et al. [8] reported that a scaling effect with strain rate dependent quantities is to be expected when running high strain rate MD simulations. The ability to extract the property evolution at distinct stages of crosslinking can be useful to help tailor the resin properties as per desired application. In future studies, the complete MD results can be used as input in higher length-scale FEA models to generate optimized composite properties [14].

4 Interfacial characteristics of Epoxy/flCNT composites

4.1 Introduction

The need for lightweight ultra-strong structural materials is increasingly being recognized for the next generation of space vehicles for deep-space human travel. To fulfill this need, significant focus has been placed on carbon nanotube (CNT) based composites materials [87-90]. These materials have the potential to exhibit superior thermo-mechanical properties relative to the current state-of-the-art composites [30, 91]. So far, a major shortcoming of these materials is their failure to translate these outstanding properties to higher length scales. Therefore, it is necessary to investigate and mitigate the failure of the CNT/matrix interfacial region to fully utilize the benefits of these materials.

A recent study by Downes et al. [31] introduced a novel fabrication method which generates stacks of flattened CNTs (flCNTs) resulting in self-aligned assemblages. These structures promote higher surface-to-surface contact which was evident when combined with a bismaleimide polymer matrix. The flCNT/BMI composite showed a twofold increase in tensile strength and a threefold increase in the tensile modulus when compared to the round CNT composite counterpart [31]. Even though the flCNT-flCNT contact was enhanced by the flattening and stacking, the TEM-observed fracture surfaces showed intra-stack sliding in addition to complete stack pullout. A follow-up study by Jolowsky et al. [32] provided a pathway to scale the flCNT composite fabrication method to macro-scale panels with excellent mechanical properties.

Although these early experimental studies showed promising results for the development of flCNT composites, they did not address the influence of different resin types on the panel-level mechanical performance. Many studies have addressed the interfacial characteristics of CNT/polymer composites [1, 2], however, none of these studies provide a comprehensive view of the influence of resin type on composite performance, and none of them address flCNT/polymer interfaces directly. Indeed, such studies for a broad range of resin types are difficult to achieve experimentally because of the difficulty and expense of fabricating and testing flCNT composites. Computational approaches are needed to efficiently drive the development and design of future flCNT composites.

High-performance polymer-based composite materials are extensively used in aerospace applications because of their excellent thermal and mechanical properties [88, 92]. Epoxy-based polymer systems are thermosets that are specifically used for structural applications [93-95]. Molecular modeling studies exploring the thermo-mechanical properties have been previously performed on such polymers [96, 97]. However, the influence of the molecular structure on the overall mechanical properties and reinforcement interface characteristics remains largely unexplored. Using MD, this study focuses on modelling the polymer/flCNT interface of a glycidylamine-based epoxy. The simulated system is an aerospace-relevant thermoset epoxy resin [93, 98, 99]. This study compliments the results published by Patil et al. [100], Pisani et al. [101], and further comparison with other thermosetting polymers can be found in Deshpande et al. [102].

4.2 Molecular Modeling

The details of the MD simulation are discussed in this section. The LAMMPS software package was used for all the simulations discussed in this paper [62]. The Interface Force Field (IFF), developed by Heinz et al. [21], was designed to accurately model the properties of inorganic surfaces. Included in the original scope of IFF is the ability to capture inorganic-organic interfaces and the adsorption of organic molecules onto inorganic surfaces. Recently, the Polymer Consistent Force Field was supplemented with IFF (PCFF-IFF) and proven successful for predicting the dispersibility of CNTs in different solvents and polymer solutions [103]. The PCFF-IFF or IFF forcefield was used to assign the interatomic potential in this study, as it was previously shown to yield accurate results for flCNTs and consists of all the relevant atom types associated with the amorphous polymer systems [104]. Additionally, this force field can model the π electrons virtually which is critical to accurately capture the polymer-flCNT interface. The IFF force field is well-known for its accurate atomic charge assignments, which has proven to have a significant effect on the predicted matrix-reinforcement interface characteristics and molecular conformations of polar molecules [100-102].

The following paragraphs demonstrate the workflow implemented in LAMMPS to build the MD models of epoxy/flCNT for each polymer mass fraction. Figure 4.1 shows the equilibrated conformations of individual monomers. A 1 fs timestep and the Nose-Hoover thermostat and barostat with “aniso” settings were used for all the simulations [64-66, 105].

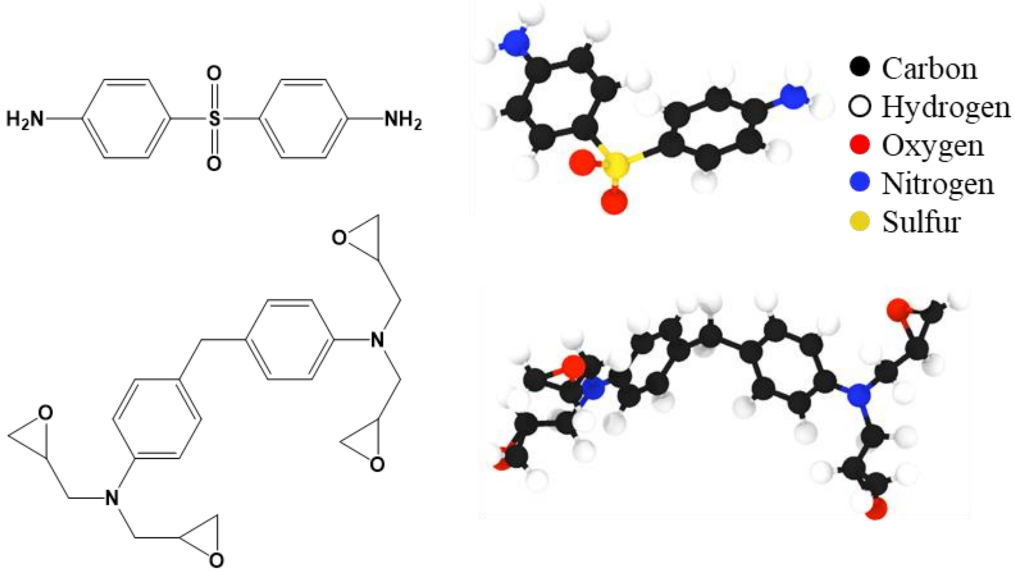

Figure 4.1. Molecular models of the monomeric units of DDS (top) and TGMDA (bottom)- chemical structures(left) and minimized structures (right) using LAMMPS. OVITO was used for molecular visualizations [63].

Relatively small simulation boxes were created to establish the equilibrium configuration of the stand-alone monomers, as shown in Figure 4.2(a). For the monomer layer, one TGMDA monomer and one DDS monomer were added to a simulation box (1:1 molar stoichiometry). To obtain the lowest energy configuration for each structure, a molecular minimization simulation was run by using the “minimize” command in LAMMPS using the conjugate gradient (CG) algorithm [68].

The monomer layer was first built without including the flCNTs. The equilibrated monomers were arranged in regularly spaced arrays in a simulation box at a low initial mass density (approximately 0.1 g/cm^3) as shown in Figure 4.2(b). Additional molecular minimization simulations were run to ensure the grouped monomers had their correct conformation before the next step.

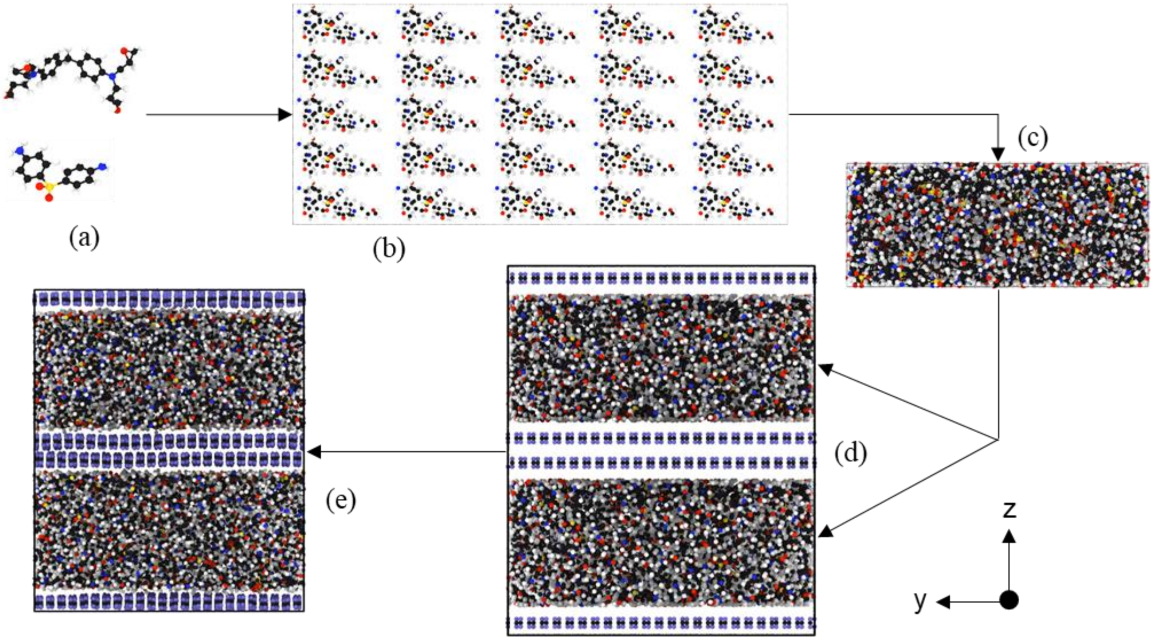

Figure 4.2. Molecular modelling workflow for the epoxy system: (a) Modeling individual monomers and placing them in a simulation box. (b) Replicating the box to form a bigger system. (c) Densifying the simulation box to tightly pack the monomers. (d) Combine the compressed model with the flCNT. (e) Perform annealing, polymerization, and equilibration on the model to prepare for property prediction.

Next, the monomers were densified to target mass density of 1.29 g/cm^3 [106]. The density value was chosen as an initial guess, with the final mass density achieved at the end of this step [9, 43, 107]. The X and Y dimensions of the simulation box was preset at 101 and 51 Å, respectively, since in a forthcoming step, fixed-dimension pseudo-flCNT layers were inserted [108]. The X and Y dimensions were kept constants for all the models to provide a uniform contact area at the interface. The densification simulations were performed at 300 K using the “fix deform” command in LAMMPS, where the Z dimension was gradually reduced at a constant rate of 10 Å/ns. The box boundaries were non-periodic and reflecting in all three directions using the “fix wall/reflect” command in LAMMPS such that they could be effectively placed between flCNTs in the subsequent step [109]. The final densified layer is shown in Figure 4.2(c).

For assembling the layered MD models, a periodic box of 101×51 Å dimensions in the X-Y plane was created. The single densified monomer layer was duplicated in the Z direction, creating a second identical layer. The second layer was necessary to run the friction simulations described below. The two layers were separated by 10 Å in the Z direction and 5 Å of empty space was added on top and bottom of the polymer layers to accommodate the two flCNTs. Because the boundaries were periodic, the polymer layer was now allowed to traverse the boundary. The flCNT layers with 23,616 atoms each were inserted into the free spaces to complete the setup as shown in Figure 4.2(d). This method of combining the monomer layers and flCNTs helped to maintain the flatness of the flCNTs. Upon assembly, the model was relaxed using an energy minimization. These layer models were developed to achieve a series of specific overall monomer mass fractions. The mass fraction, in this case, is the ratio of molecular mass of monomers to the molecular mass of the entire system including the flCNTs. In this work, individual models for mass fractions ranging from 10 % to 80 % were built with the sizes ranging from 25,000 – 65,000 atoms.

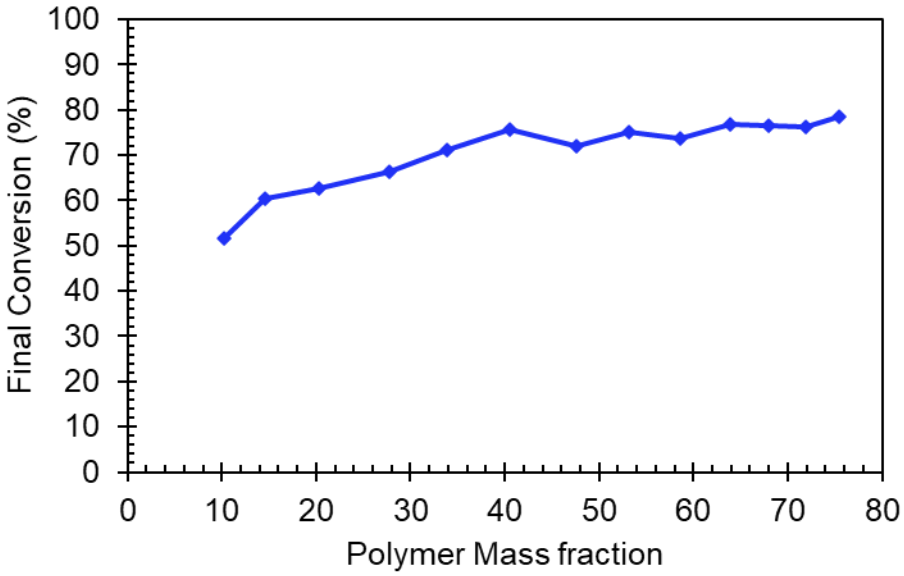

Figure 4.3. Maximum conversion achieved in the system based on polymer concentration.

The assembled layered MD models were equilibrated by running a 0.1 ns simulation using the NPT ensemble with the temperature and pressure set to 300 K and 1 atm, respectively. Next, the system temperature was increased to 600 K and equilibrated for 0.1 ns using the NPT ensemble. Finally, the model was annealed down to 300 K over 6 ns with a constant cooling rate of 50 K/ns. To allow the simulation box volume to adjust for the changes in temperature, a barostat was set to maintain a pressure of 1 atm.

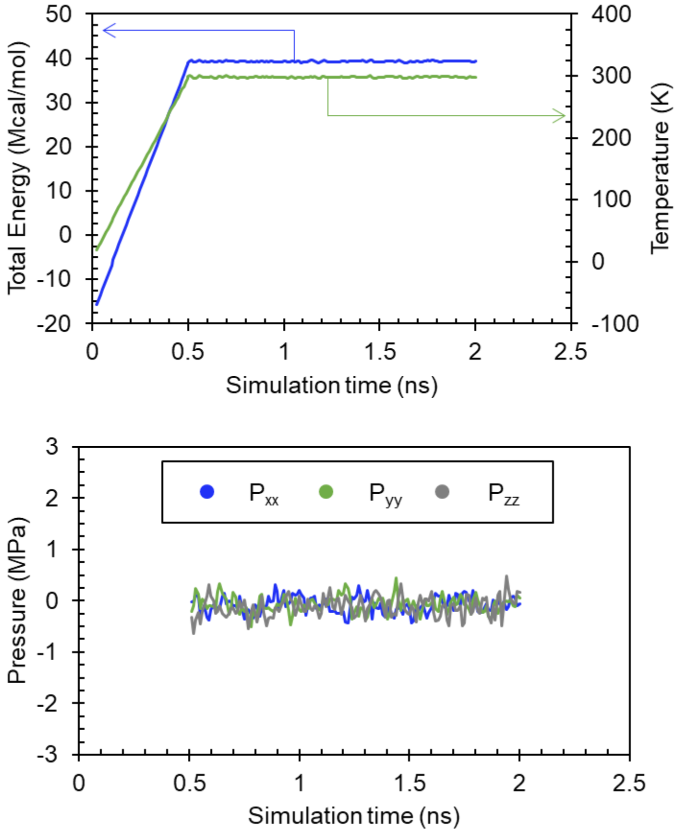

Figure 4.4. (top) Total energy and temperature of the flCNT/epoxy (40.52% mass fraction) model during the equilibration simulation. (bottom) System pressure (tensor) of the model after energy convergence.

After annealing, the models were virtually cured by performing polymerization simulations. Polymerization simulations were performed using the REACTER protocol as demonstrated by Gissinger et al. [69]. Rather than using in-house scripts, this choice provides a highly reproducible procedure for crosslinking polymers [69, 70]. The simulation was performed at 400 K temperature to promote maximum bond formation. The bond formation cutoff distance was maintained at 6 Å. All the polymerization simulations were performed using 1 fs timesteps in the NVT ensemble for 500 ps. Figure 4.3 shows the maximum conversion in all the models.

The epoxy polymerization was performed by simulating self-promoted epoxide-amine crosslink reactions as shown in Figure 3.4. This crosslinking reaction is a two-step process which begins with the opening of the oxirane ring and bond formation with the primary amine. Once formed, the secondary amine reinitializes the ring opening of another oxirane ring in its vicinity [6, 9, 110].

After polymerization, the models were annealed, again, using identical settings as described before. This second stage of annealing was performed to help the newer networks find more desirable configurations [111]. After annealing, the models were equilibrated to prepare for room temperature property prediction. These simulations were performed using the NPT ensemble over 2 ns. Figure 4.2(e) shows the fully equilibrated model. Once equilibrated, the models were checked for convergence by observing the total energy of the system. Convergence of the energy was established to approve of the equilibration. Another appointed check was evaluation of the virial pressure tensors within the system. Figure 4.4 shows the representative plot of the energy and pressure curves. The initial ramp in the energy and temperature curve was because the simulation was conducted in two steps. During the first 0.5 ns, the system was slowing heated up to the room temperature to avoid any thermally induced vibrations. The later portion of the simulation was at room temperature (300 K) using the NPT ensemble and 1 fs timestep.

Figure 4.5 shows the atomic mass densities along Z-direction and highlights the higher atomic densities near the interface for a representative model. The higher polymer density at the interface can be seen in the form of a secondary peak (red-dotted circles) adjacent to the larger peaks, which represent flCNT atoms. Figure 4.6 shows the polymerized models for different polymer mass fractions. Within these figures, the left-most image displays the lowest polymer mass fraction resulting in clustering of polymer atoms. The middle image displays a perfectly saturated interface with the two flCNT layers completely separated by the polymer atoms. The right-most image displays the highest polymer mass fraction which results in addition of excessive polymer atoms.

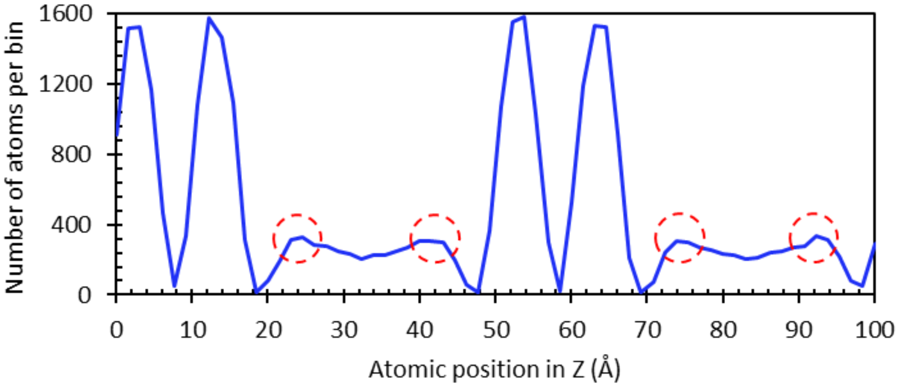

Figure 4.5. Atomic count profile for the 40.52% Epoxy showing the distribution for 0.5 Å bin size. Secondary peaks (red-dotted circle) highlighting the interfacial saturation by polymer atoms.

The equilibrated models were then evaluated for the interfacial interaction energy, friction resistance, and transverse strength. The interaction energy and friction simulations were also conducted on the unpolymerized models to assess the effect of polymerization. To compute the interaction energy, the purely non-bonded potential energy unrelated to the polymer and flCNTs was extracted from the model using the help of the "compute group/group" command in LAMMPS [112, 113]. For all models, the simulations were performed in the NPT ensemble over 0.5 ns to collect the time-averaged interaction energy data. Temperature and pressure settings of 300 K and 1 atm respectively were used for all these simulations.

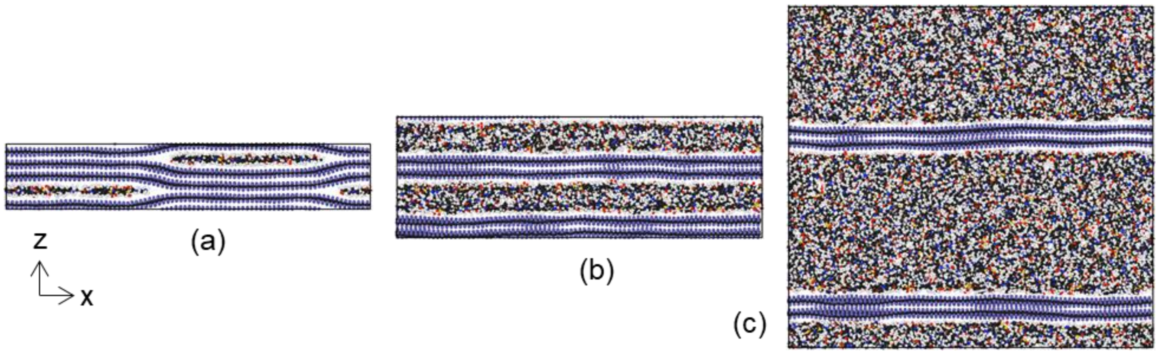

Figure 4.6. Molecular models of flCNT/epoxy composites with mass fraction- (a) 10%, (b) 41%, and (c) 75%.

Patil et al. [100] demonstrated a novel approach to compute atomistic friction force between polymer-infiltrated flCNTs using the same simulation geometry described herein. Using the same approach, friction simulations were performed on both the unpolymerized and polymerized models for each resin system. For all the models, both the flCNTs (both top and bottom walls of the flCNT layers) were tethered to two distinct points with a virtual spring using LAMMPS. Thus, the walls within a single layer of flCNTs were not allowed to slide with respect to each other such that the friction between the flCNT/polymer interface could be isolated. The spring constant used for both the springs was set to 1 kcal/mol·Å^2. The point connected to the bottom layer was linearly displaced in the X direction using a velocity range of 0.1 Å/ps to 5 Å/ps. The other layer was held in position using the NPT ensemble with 300 K temperature and 1 atm pressure. The polymer layers and the sliding flCNT were maintained under the NVE ensemble, allowing the temperature to change, and thus enhancing the vibrations at the interfaces. The resulting friction force was computed between the moving flCNT and the polymer layer, and the fixed flCNT and the polymer layer. FIGURE represents the friction force simulation setup.

The third criterion studied is the transverse strength of the layered models. The equilibrated model with a polymer mass fraction of approximately 0.4 was used for comparison with other resin systems. This polymer mass fraction is comparable with previously reported data [100-102]. Additionally, the lowest and highest polymer mass fraction models were also evaluated to provide an insight on the effect of the polymer mass fraction on the transverse properties. To assess the transverse tension behavior, the simulation box was subjected to a uniaxial strain in the direction perpendicular to the flCNT plane at a constant strain rate of 2×10^8 s^{-1} until there was total separation of one of the CNT/polymer interfaces or a maximum of 150% strain was reached. The overall system stresses and strains were recorded, and the corresponding stiffness, strength, and toughness values were calculated. An R script was used for this analysis. It is important to note that in these simulations, the upper and lower walls of single layers of flCNTs did not separate from each other, as the flCNT/polymer interface always failed first. Thus, the results are naturally focused only on the flCNT/polymer interface mechanical behavior.

4.3 Results

4.3.1 Interaction energy

$$\mathrm{I.E.} = E_{Total} - \left(E_{polymer} + E_{flCNT}\right) \tag{5}$$

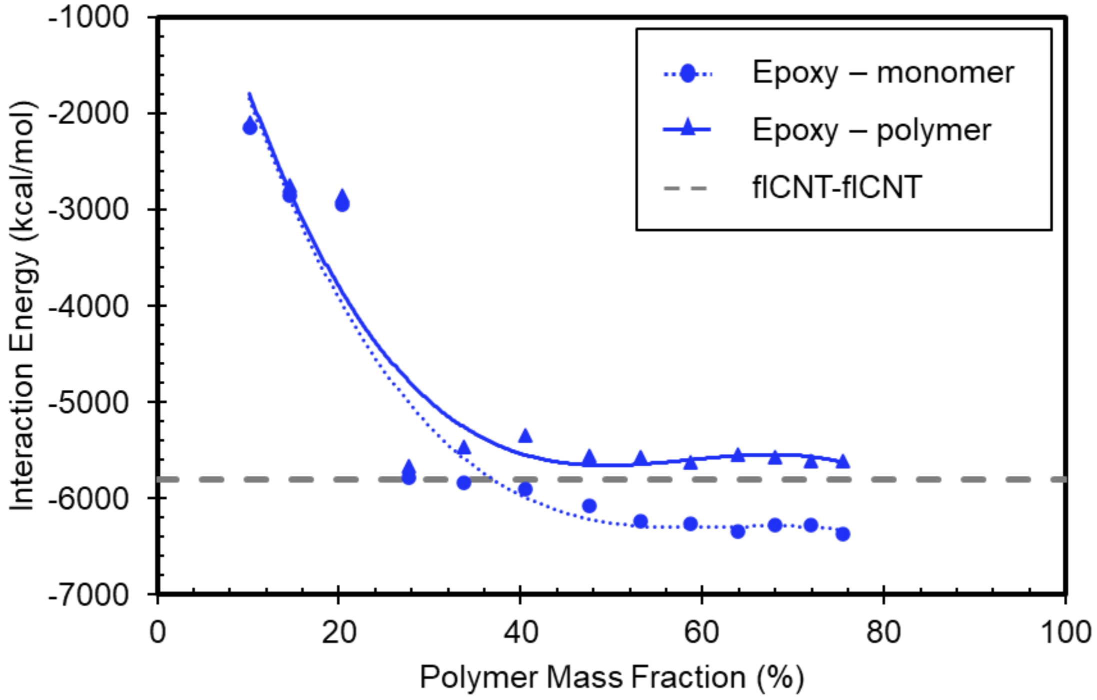

Figure 4.7. Interaction energy between flCNTs and polymer layers with varying polymer mass fraction for monomer and polymer case.

Interaction energy is the non-bonded energy within the system which is not associated with the individual components of the model. It is a measure of the attractive energy between the polymer atoms and the flCNT atoms and is obtained by computing Equation (5). Where, E_{Total} is the total non-bonded energy in the MD model (van der Waals and electrostatic energies), and $E_{polymer}$ and E_{flCNT} are the non-bonded energies from the polymer layer and flCNTs, respectively. The interaction energy for the unpolymerized and polymerized models are shown in Figure 4.7. The displayed trendlines are to distinguish different datasets and provide clear trends amongst the scattered data points. It is important to note that the trendlines do not bear any physical significance. The interaction energy values carry a negative sign which indicates attraction to the aromatic surface of the flCNT. Therefore, higher negative values indicate greater polymer/surface affinity. Figure 4.7

shows a dramatic increase in the interaction energy, both monomer and polymer, with increases in polymer mass fraction.

The data in Figure 4.7 indicates the strengthening of interaction depends highly on the effective saturation of the polymer-flCNT interface. The initial increase is significant and is due to clustering of polymer molecules at the interface for lower mass fractions, which is evident from Figure 4.6(a). Well-distributed monomers are observed in the interfacial region at polymer mass fractions 33% or greater. For higher polymer mass fractions, the flCNTs were completely encompassed by a 10 Å or thicker polymer region, and the interaction energy stays relatively constant.

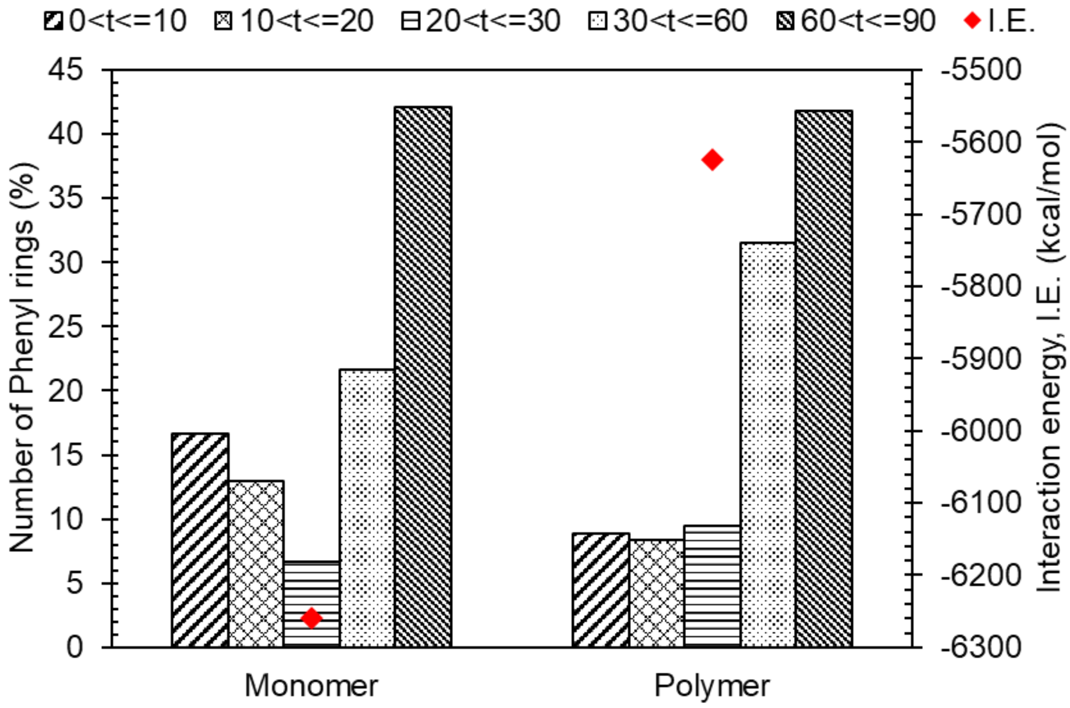

Figure 4.8. Alignment of phenyl rings (dihedral angles) and interaction energy for 58.66% polymer mass fraction model, t(degrees) is dihedral angle formed by the phenyl rings with the XY plane.

Post-polymerization, the interaction energy plot shift upwards indicating loss of interaction strength due to the new networked polymer topology. Figure 4.8 shows the orientation of the phenyl rings in the monomer and polymer structures with respect to the flCNT surface. It is well-documented that phenyl groups promote aromatic-aromatic non-bonded stacking, a.k.a. π-π stacking [114-117]. The orientations were computed by extracting the dihedral angles of the phenyl rings within the polymer layers. The angle was calculated with respect to the X-Y plane of the flCNT surface, ignoring deviations caused due to slight waviness as seen in Figure 4.6. Lower angles represent greater degrees of alignment with the flCNT surface. The monomer/polymer mass fractions used for this analysis correspond to the converged interaction energies. This analysis was conducted to provide physical insight into the interaction energy trends. Earlier studies have shown the non-bonded interactions between the aromatic groups is a strong contributor towards the interaction energy [117].

Figure 4.8 clearly shows the decrease in interfacial interaction when the monomers undergo polymerization and result in lower numbers of phenyl rings aligned with the interface. The creation of networks results in additional mobility constraints which results in higher angles between the phenyl rings and the flat aromatic surface. Within each model, the number of phenyl rings with less than 10^{o} angle is reduced after crosslinking. The models show a higher drop in the interaction energy since neither of the two components strongly prefer the flCNT surface.

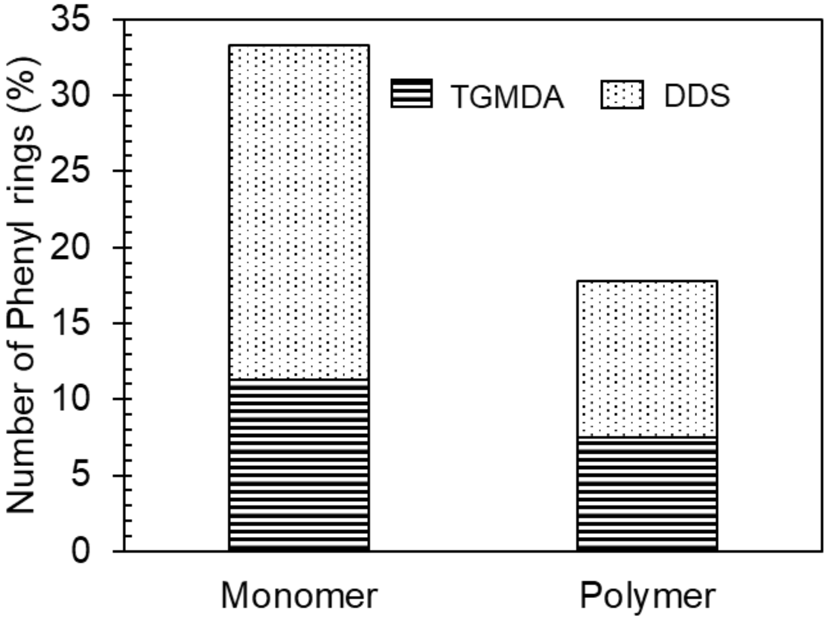

Figure 4.9. Alignment of phenyl rings with a dihedral angle of 10° or less for the individual components of the epoxy system.

Figure 4.9 shows the number of phenyl rings with a dihedral angle of less than or equal to 10° with the flCNT surface for the epoxy systems highlighting the orientations from the individual components. It can be concluded that the epoxy system does not benefit greatly with the increasing mass fractions at the expense of adding mass to the system.

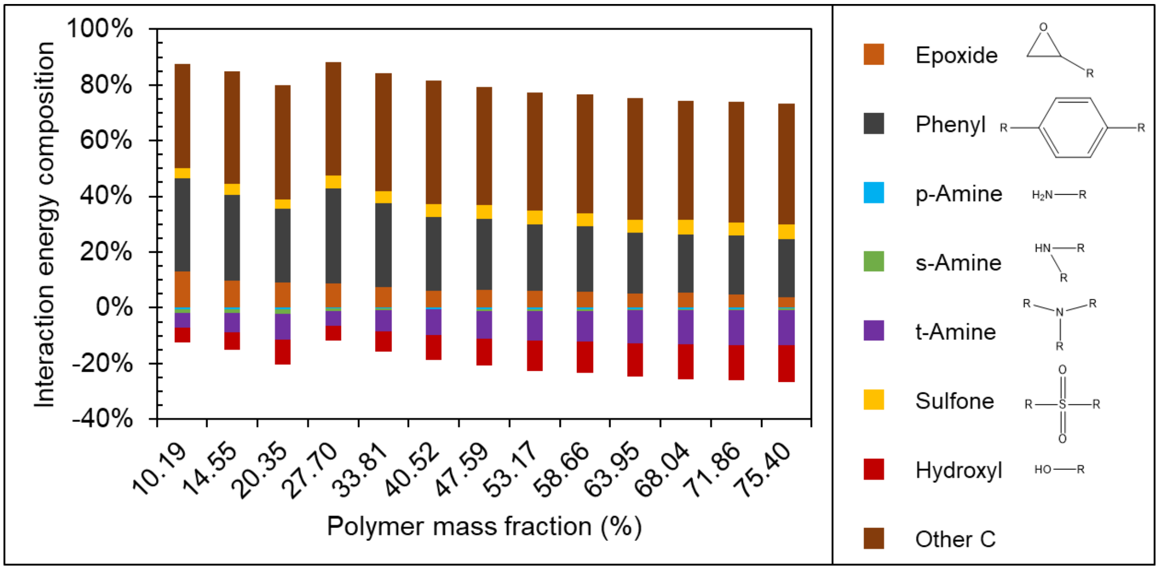

Figure 4.10. Chemical group-wise decomposition of the total interaction energy for all the models.

Figure 4.10 shows the contribution from chemical groups within the epoxy composition towards the total interaction energy. The analysis was performed to understand how individual chemical groups contribute to the overall interaction energy. The results indicate that the reactive groups within the polymer, the epoxide and amine, dictate the effect of polymer mass fraction on the overall interaction energy. With increasing polymer mass fraction, the extent of polymerization also increases as seen from Figure 4.3. Hence, the amount of newly formed bonds increases with increasing conversion percent. This results in a smaller number of epoxide groups, and more tertiary amine and hydroxyl groups. The negative value does not necessarily mean the contribution is repulsive, it is an artifact of the individual formulation of the potential energy which is established in the initial stages of model building. As seen from the Figure 4.10, for higher polymer mass fractions, the availability of the more N atoms benefits the overall interaction energy.

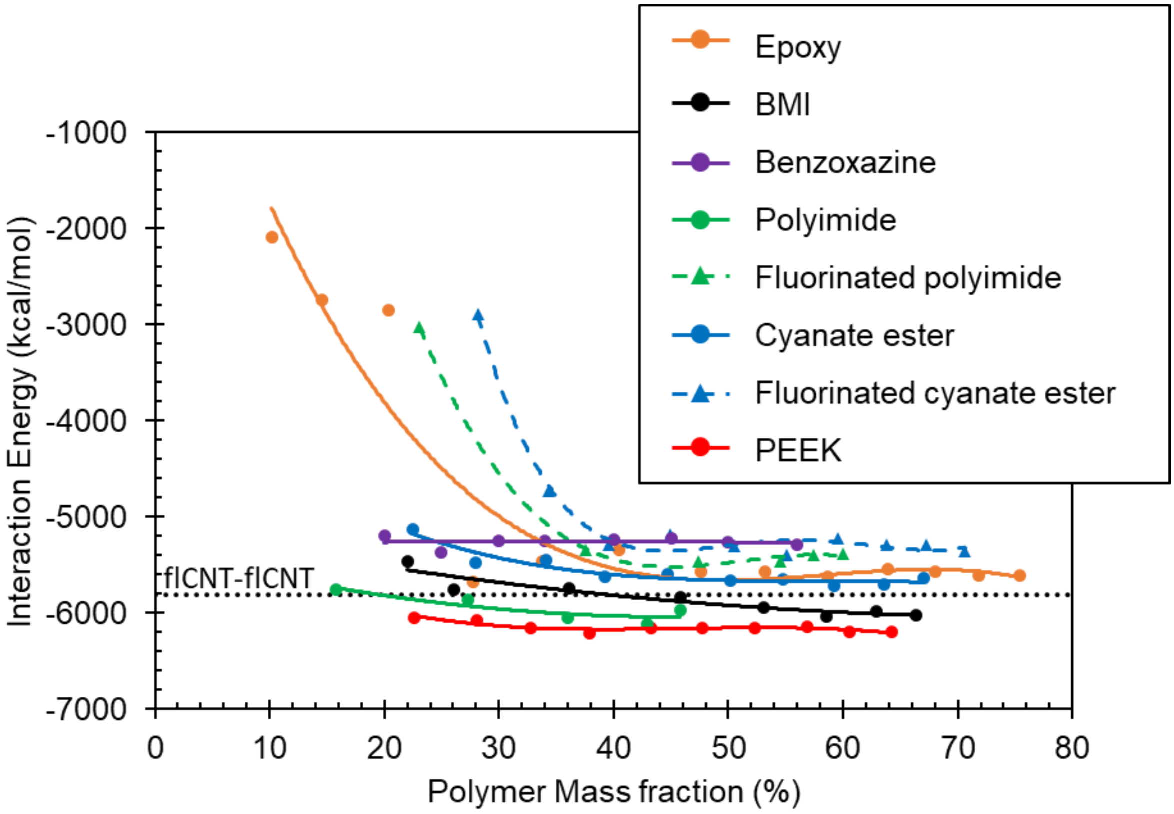

Figure 4.11. Interaction energy between flCNTs and polymer layers with varying polymer mass fraction for a wide range of polymers, including data from Pisani et al. [101], Deshpande et al. [102] and Patil et al. [100].

Figure 4.11 shows the interaction energy for multiple polymer systems including those reported in previous studies [100-102]. The PEEK and non-fluorinated polyimide show the highest degree of interaction, whereas the fluorinated polymers have a relatively low level of interaction because of steric hindrance from the fluorinated groups. The interaction from the benzoxazine is also relatively low. The interaction energy of BMI and epoxy systems lie in the middle of the other polymers. BMI shows slightly better affinity due to the preferential adsorption of BMPM molecules. BMI is the only thermoset in this group with an interaction energy that is lower than that of the bare flCNTs.

4.3.2 Frictional Resistance

The results from the friction simulations are detailed in this section for both the monomers and polymers. The trend lines used in all the figures are included to visually distinguish between the datasets and do not hold any physical significance.

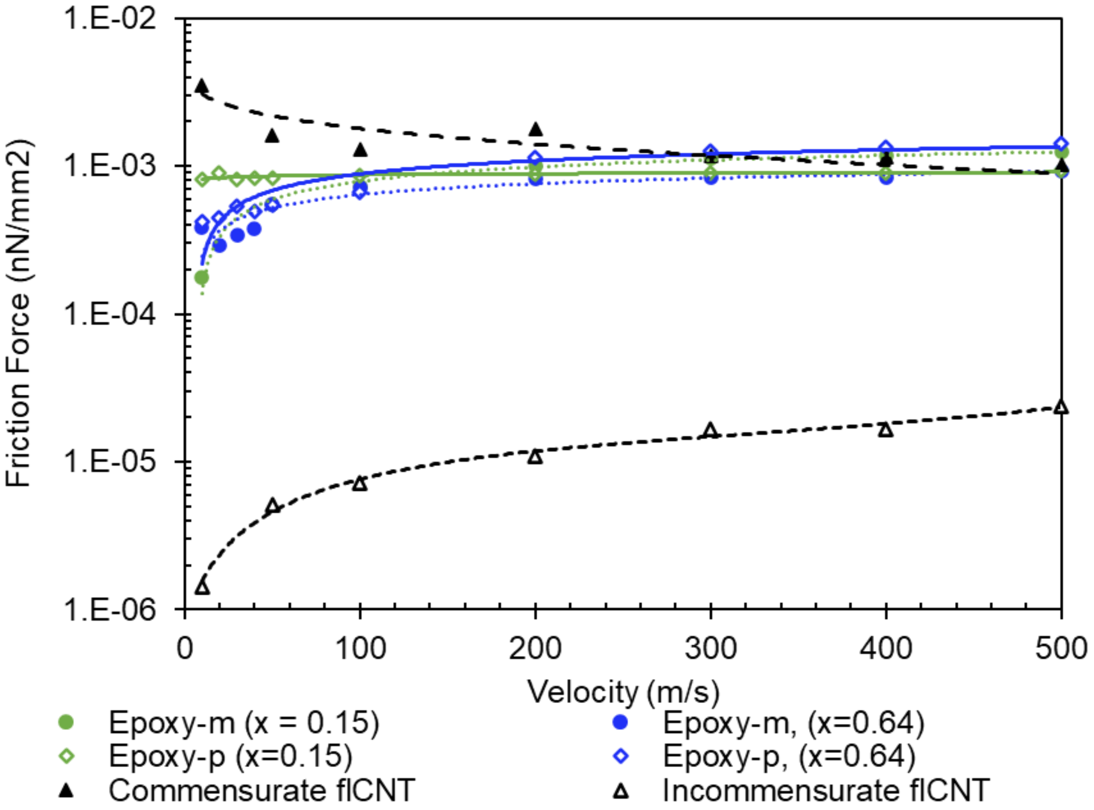

Figure 4.12. Friction force of the composite and commensurate/incommensurate flCNTs as a function of velocity for monomer and polymer cases, where x is the polymer mass fraction.

Figure 4.12 reveals the friction force trend for the polymerized and unpolymerized models, as well as the friction force associated with flCNTs with no polymer (commensurate and incommensurate). The incommensurate flCNT-flCNT friction case is considered to accurately represent the actual stacking configuration in flCNT stacks [118, 119]. As reported previously, the presence of a polymer layer results in an increase of two orders of magnitude in the friction force exhibited by the incommensurate flCNT-flCNT [100-102]. At low velocities, the models (both monomeric and polymeric forms) display a close performance because of the scarcity of polymer atoms at the interface. Crosslinking the models significantly enhances the friction force. The effect of polymerization displays an inverse trend as seen from the interaction energy study, where polymerization reduced the interaction, yet increases the frictional force. Polymerization imposes additional restrictions on the movement of the monomeric units by the formation of a polymer network. The formation of a more rigid network causes a greater amount of coarsening (i.e., protrusion of constrained molecular groups into the flCNT surface) and thus increased interface friction, whereas un-crosslinked monomers can more easily conform to the flCNT surface and thus form a smoother interface with less friction. Figure A-4 and Figure A-5 display the minimum and maximum polymer mass fraction models for the unpolymerized and polymerized conditions, respectively.

In Figure A-1, the effect of polymer mass fraction on the frictional resistance is demonstrated for the complete collection of flCNT-polymer models and no discernable trend was observed for the range of mass fractions. The results from 10 m/s sliding velocity were chosen for comparison. For all the models, the friction force increases post-polymerization. As seen in Figure 4.7, the observations indicate an inverse relation between the friction force and interaction energy. That is, polymers exhibiting higher interaction energies exhibited lower frictional resistance, and the systems with lower interaction energy displayed better friction force. Also, polymerization degrades the interaction energy of all the polymers, however, it enhances the friction force for the same systems. Figure A-3 from the Appendix A shows the data for other velocities and similar trends were observed.

To summarize the results for the friction simulations, Figure 4.13 shows the frictional force curves of the polymerized models and includes results for the polyimide, PEEK, BMI, benzoxazine and cyanate ester systems from Patil et al. [100], Pisani et al. [101], and Deshpande et al. [102]. The benzoxazine system shows higher frictional resistance in comparison to the fluorinated polymers. It was reported that the fluorinated polymers exhibit higher friction due to the presence of the trifluoromethyl groups [100]. The epoxy and BMI systems also exhibit a good frictional resistance amongst the non-fluorinated polymers. Figure A-2 in the Appendix A shows the comparison of the same polymers for different polymer mass fractions with a 10 m/s velocity, and like Figure A-1, no discernable trend was observed.

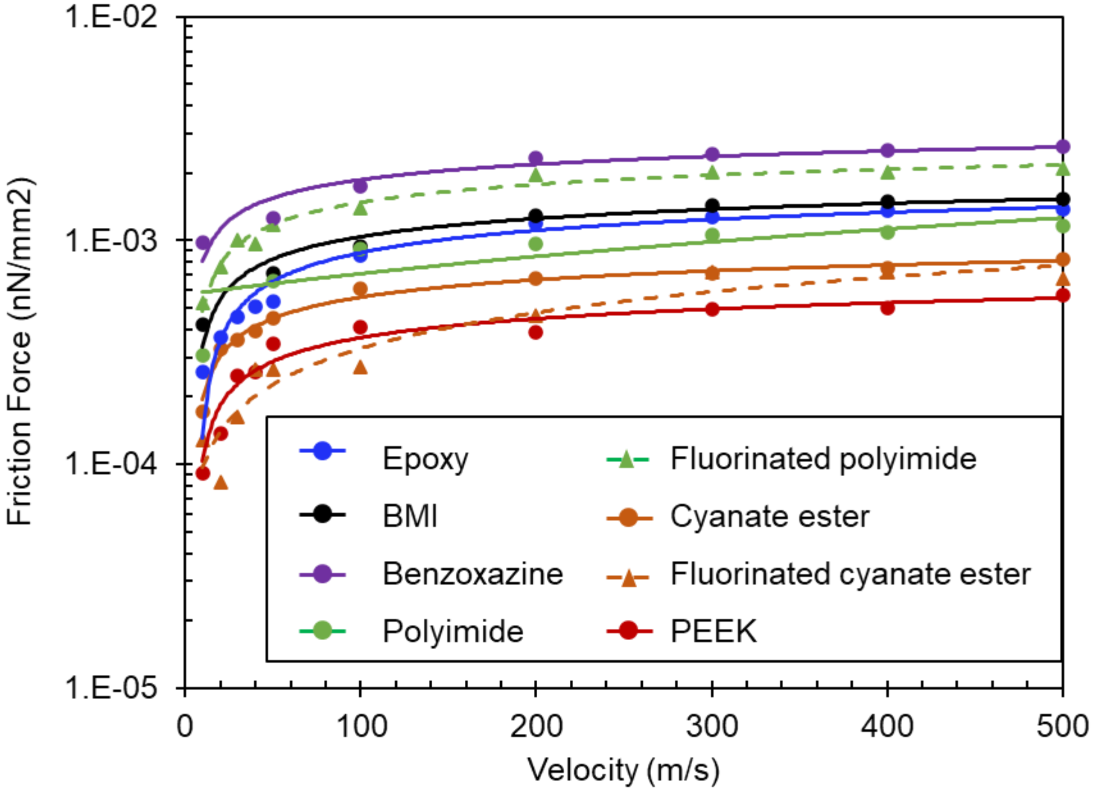

Figure 4.13. Friction force of polymer systems as a function of velocity for the polymer case, including data from Deshpande et al. [102], Pisani et al. [101], and Patil et al. [100].

4.3.3 Transverse Strength

Figure 4.14. Transverse tension simulation from 0 % to 65 % strain in Z direction.

Figure 4.14 shows the snapshot of MD simulation box for 41% polymer mass fraction model during the transverse tension simulation in Z direction. Figure 4.15 shows the stress-strain response from the transverse tension simulations for polymer mass fractions of 10

%, 41%, and 75%. The selected models included the lowest, optimal, and highest mass fraction. The optimal mass fraction refers to the model which is comparable to the other polymer systems reported in previous work [100-102]. It is important to note that stress-strain data that is generated using all-atom MD simulations inherently includes a strain rate effect that results from the simulated deformation rates that are orders of magnitude above laboratory-observed deformation rates [8, 9, 44]. Thus, the stress strain response shown in the figure is not necessarily what would be expected from an experimental tensile test of the interfacial region. However, the relevant information from the figure is the comparative response of the different systems. MD-generated stress-strain curves provide a quantitative comparison the response of different systems to discern trends and physical insight.

Table 1. Transverse properties

Polymer Mass fraction (x)	0.1	0.41	0.75
Stiffness (GPa)	9.91	6.07	6.65
Toughness (MJ/m^3)	120.01	82.77	32.14
Peak Strength (MPa)	498.83	331.07	332.45

From the Figure 4.15, the optimal and the highest mass fraction model display deterioration of transverse properties when compared to the lowest mass fraction model. Table 1 lists the numeric values of the three selected metrics. Addition of more polymer atoms results in 38.71% and 32.90% reduction in the transverse stiffness, 31.03% and 73.22% reduction in the toughness, and 33.63% and 33.36 % in the peak strength for the optimal and highest mass fraction model respectively when compared to the lowest mass fraction model.

Figure 4.16 includes the transverse tension results for all the polymer systems including the corresponding data for the polyimide, cyanate ester, BMI, benzoxazine and PEEK systems from previous studies [100-102]. From the comparison, BMI shows the best performance in all the three metrics. Epoxy shows the second highest stiffness and peak strength but lower toughness than benzoxazine and the fluorinated cyanate ester.

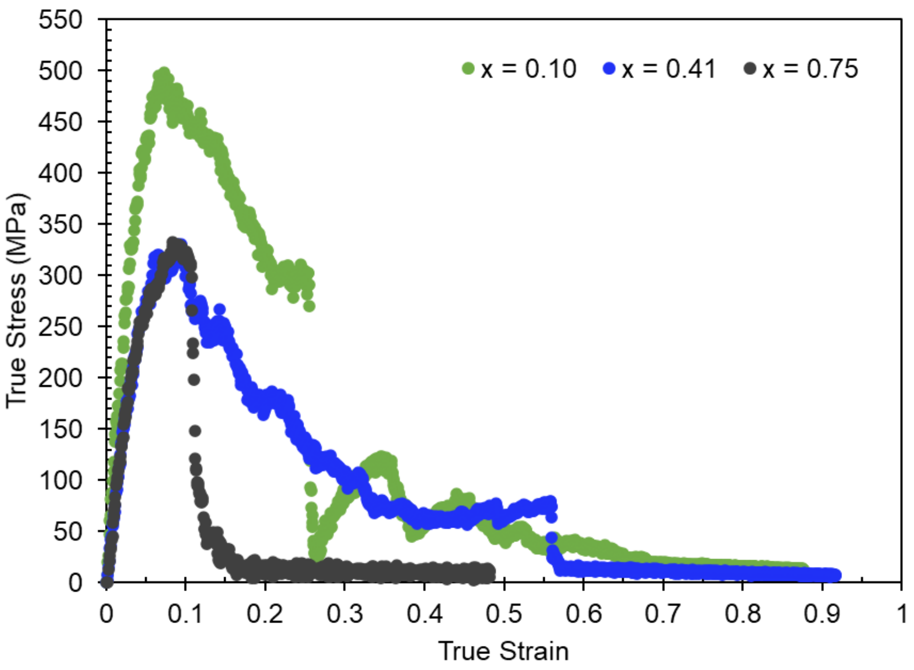

Figure 4.15. Stress-strain curves of the three polymerized systems in transverse tension.

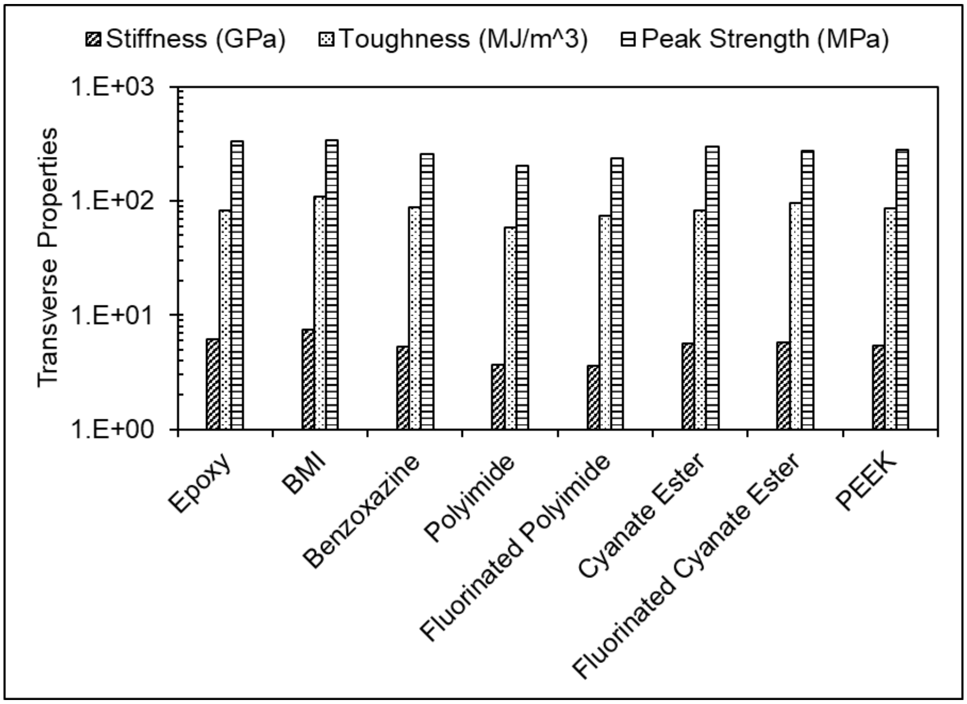

Figure 4.16. Stiffness, toughness, and peak strength for the polymerized polymer/flCNTs.

4.4 Conclusion

Epoxy produces the best overall compatibility with the flCNTs after BMI. Including the previously reported systems, PEEK still shows the best interaction with the flCNTs with the polyimide and BMI also showing higher interaction than bare flCNTs [100-102]. However, benzoxazine exhibits a much superior friction force than the other systems from Patil et al. [100], Pisani et al. [101], and Deshpande et al. [102]. With a best performance in two out of the three metrics, including the three sub-metrics from transverse tension, the BMI is the polymer matrix of choice when considering the flCNT stacks. However, in the design of such nanocomposites, careful consideration may be required in balancing the three described metrics as per the application. Therefore, the molecular insights gained from this research can be helpful in guiding the selection of resin systems for the engineering of new flCNT-based composites. The results of this study are not applicable to traditional carbon fiber/polymer composites, as carbon fiber generally has a significant sizing layer on the fiber surface, and carbon fibers generally don’t have the pristine aromatic surface that was studied herein for flCNTs.

5 Optimizing functionalization to improve interfacial shear strength of BMI composite

5.1 Introduction

Polymer matrix composites (PMCs) are commonly used in the aerospace industry as primary structural components. Porting these materials for space applications will require designing ultra-strong, yet lightweight counterparts [87]. Graphene-like reinforcements have been studied extensively to produce the desired mechanical properties. The exceptional properties of these materials include a specific modulus of ~1 TPa and a specific strength greater than 100 GPa [30]. Like most of the carbon reinforced composites, these materials are limited by poor load transfer at the interface [1, 2]. Improving the design of the interfacial region is critical to enhancing the interfacial strength of the material.

One of many strategies that enhance the interfacial strength is the covalent functionalization of the reinforcement [4, 5, 120]. Functionalization of the reinforcement results in the formation of covalent bonds with the polymer matrix, which can improve the load transfer within the composite. Despite several advantages, excessive functionalization often leads to a degradation of the reinforcement material. For example, pristine graphene structure is well known for its exceptional mechanical properties; however, degradation can lead to decline of the same properties [3]. Identifying the optimal degree of functionalization for any composite system can help with balancing the outcomes of functionalization [121]. Cheng et al. [5] demonstrated the enhancement of the mechanical properties of a carbon nanotube (CNT) and bismaleimide (BMI) composite when the CNT surface was functionalized with epoxy rings. The reported improvements were significant when compared to the pristine CNT/BMI composite.

To fully understand the influence of functionalization on the interfacial strength, it is critical to characterize the interface based on several factors, including the polymer matrix chemistry; chemistry of the functional groups; density and distribution of the functional groups; and polymer chain tethering with the reinforcement [3]. Computational tools like molecular dynamics (MD) provide an effective way of analyzing such characteristics [100-102, 122]. Several studies have been performed where the interfacial shear strength (ISS) was computed using MD for different polymer matrices and CNT composites [12, 122-125]. These studies were inconclusive regarding which specific factors directly affect the mechanical response of a functionalized composite. However, it is apparent that the interfacial properties are sensitive to the local chemical environment and the bulk matrix properties.

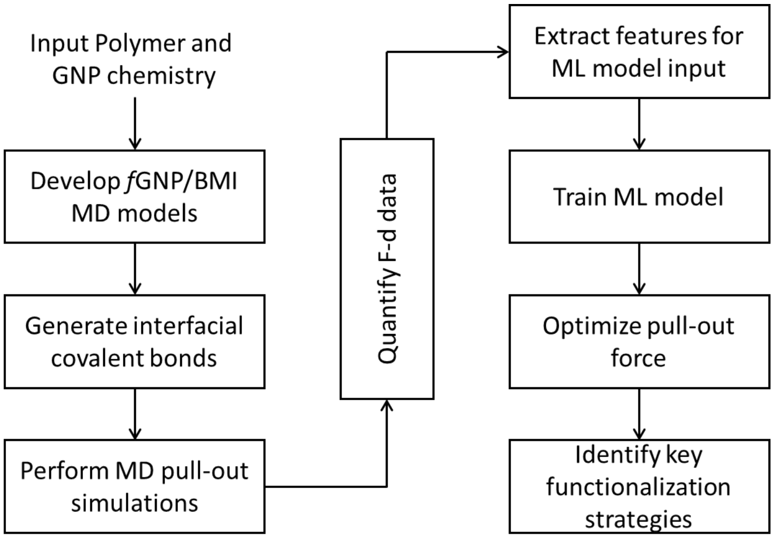

Figure 5.1. Overall modeling workflow.

Optimization of the interfacial chemistry to enhance the ISS is a complex problem and requires exploration of a large design space. MD simulations, although powerful, are computationally expensive, which may limit the investigation of the problem under study. Rahman et al. [39] developed an ML-based surrogate model that rapidly predicted the interfacial strength for different functionalization strategies by using MD simulations as the training dataset. This work adapts a similar workflow but focuses more on the characteristics of the functionalization of three-layer functionalized graphene nanoplatelet (*f*GNP)/BMI nanocomposite. To be precise, an optimal functionalization strategy for improving the nanocomposite ISS is sought. Figure 5.1 shows the schematic of the proposed MD-ML workflow. A Graph Convolutional Network or GCN is class of convolutional neural networks that can train on graph-like structured data [126-128]. A GCN is developed to link a molecular structure to its corresponding ISS. This chapter details the MD portion of the study, which includes the molecular modeling details and the resulting ISS measurements. The next steps in the proposed workflow are also discussed.

A proof-of-concept study was conducted (section 5.2.2) to verify the usage of GCN as a surrogate model to predict failure with MD simulations. For this work, a single polymer chain was modelled, and an MD simulation was performed to predict chain failure.

5.2 Molecular Modeling

The MD simulations were performed using the LAMMPS open-source code [62]. The force field used was the Reactive Interface Force Field (IFF-R), which employs a hybrid bond description to the covalent bonds in the molecule [25]. These hybrid bonds are a combination of class2 fixed bonds (or harmonic bonds) and morse bonds. The class2 bonds are rigid and do not simulate bond failure or formation, whereas the morse bonds are capable of scission. IFF-R was developed to accurately model amorphous materials with MD, and it was chosen to simulate the reinforcement pull-out [8, 21, 55, 56, 104]. The Nose-Hoover thermostat and barostat with "aniso" settings were used for all the simulations [64-66, 105]

5.2.1 *f*GNP/BMI composite

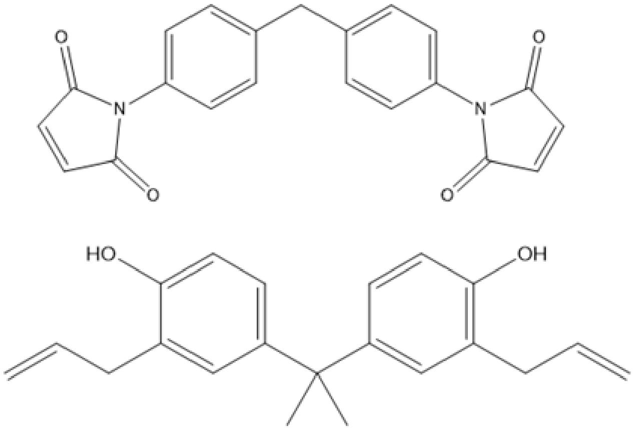

Figure 5.2. Chemical structures of (top) 4,4'-bismaleimidodiphenylmethane or BMPM and (bottom) O,O'-diallyl bisphenol-A or DBA.

The MD model composition includes a bismaleimide (BMI) matrix and a three-layer functionalized graphene nanoplatelet (*f*GNP). The chosen BMI system resembles the

Matrimid-5292 resin which is produced by Huntsman International LLC [129]. The chemical structures of this two-component resin are shown in Figure 5.2. To maximize crosslinking during cure, it is crucial to achieve complete stoichiometry. Each of the two resin components being di-functional were mixed with a stoichiometric ratio of 1:1. The *f*GNP was functionalized by attaching epoxy rings on the top surface of the 3-layer GNP [5]. The top surface of the *f*GNP interfaces with the polymer atoms. Total layer count of three was strategically selected since the inter-layer distances account for the full range of van der Waals interaction of ~10 Å. With the interaction distance under consideration, the interfacial properties should be ideal to maximize the ISS.

To build the MD model, the two BMI monomers were multiplied to create a big simulation box with ~22,000 polymer atoms. All the six box boundaries were set to fixed (or non-periodic) to avoid atoms passing the boundary. This condition was maintained until the *f*GNP layers were combined with the polymer layer. Molecular minimization simulations were performed to ensure best conformations and lowest energy configurations.

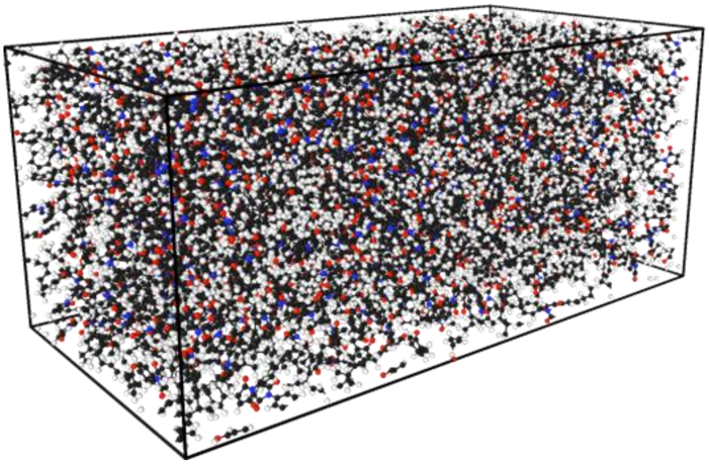

Figure 5.3. MD model of the polymer layer.

Next, the monomers were allowed to mix for 0.1 ns with a temperature ramp of 600 K – 300 K using the NVT conditions. Then the simulation box was gradually densified to achieve the bulk density of the polymer. The LAMMPS command “fix deform” is used to gradually increase the density of the simulation box by geometric compression. The target density of the polymer was set equal to that of the reported resin density of BMI, 1.2 g/cm3

[130]. The initial density of the model was in the range of 0.09-0.10 g/cm3. This densification was performed at 300K at a constant deformation strain rate of 10 Å/ns. During the densification, the X and Y dimensions were maintained at 101 Å and 51 Å, respectively. Only the Z dimension was subjected to deformation over 4 ns. The dimensional constraints were employed since the X and Y dimensions of the *f*GNP model were fixed at the same values. The fully densified model is shown in Figure 5.3. To verify uniform densification, densities across X-, Y-, and Z-directions were computed. The average density obtained was 1.2 g/cc, the distribution being uniform in each direction.

A three-layer pristine GNP was modeled using LAMMPS. Using an in-house Python script, epoxy rings were attached to the top layer by randomly converting the GNP sp^2 carbon atoms to sp^3 carbon. Figure 5.4 shows the flowchart which explains the process of generating the functionalizations on the top surface. Once the epoxy groups were attached on the GNP layer, a supplementary LAMMPS simulation was performed to update the topological transformations. This simulation was performed using the NPT condition over 0.1 ns at 300 K temperature. A range of functionalization degrees were modeled. In total, 55 unique *f*GNP models were generated with the range of functionalization densities between 0.51 % to 17.99 %.

Next, each of the *f*GNP models were combined with the polymer layer and annealed by ramping down the system temperature from 500 K to 300 K with a constant cooling rate of 50 K/ns. An NPT condition was maintained throughout the simulation. The X and Y boundaries were switched to be periodic, however the Z boundary was still fixed. By fixing the Z boundary, the bottom *f*GNP layer was inert to the polymer atoms across the boundary.

With the fully annealed models, interfacial crosslinking was performed by implementing another in-house Python script. Figure 5.5 shows the flowchart that depicts the Python-LAMMPS workflow which was used to generate interfacial crosslinks. The hydroxyl groups in the DBA monomer were selected by parsing through the ones which were within the 6 Å distance from the epoxy rings on the *f*GNP. The eligible hydroxyl groups were then crosslinked with the epoxy groups and the related force field parameters were subsequently updated. A supplementary LAMMPS simulation was performed to delete the pre-reaction bonds, update related parameters, and stabilize the newly formed topologies. This simulation was performed under NPT conditions over 0.1 ns at 300 K temperature.

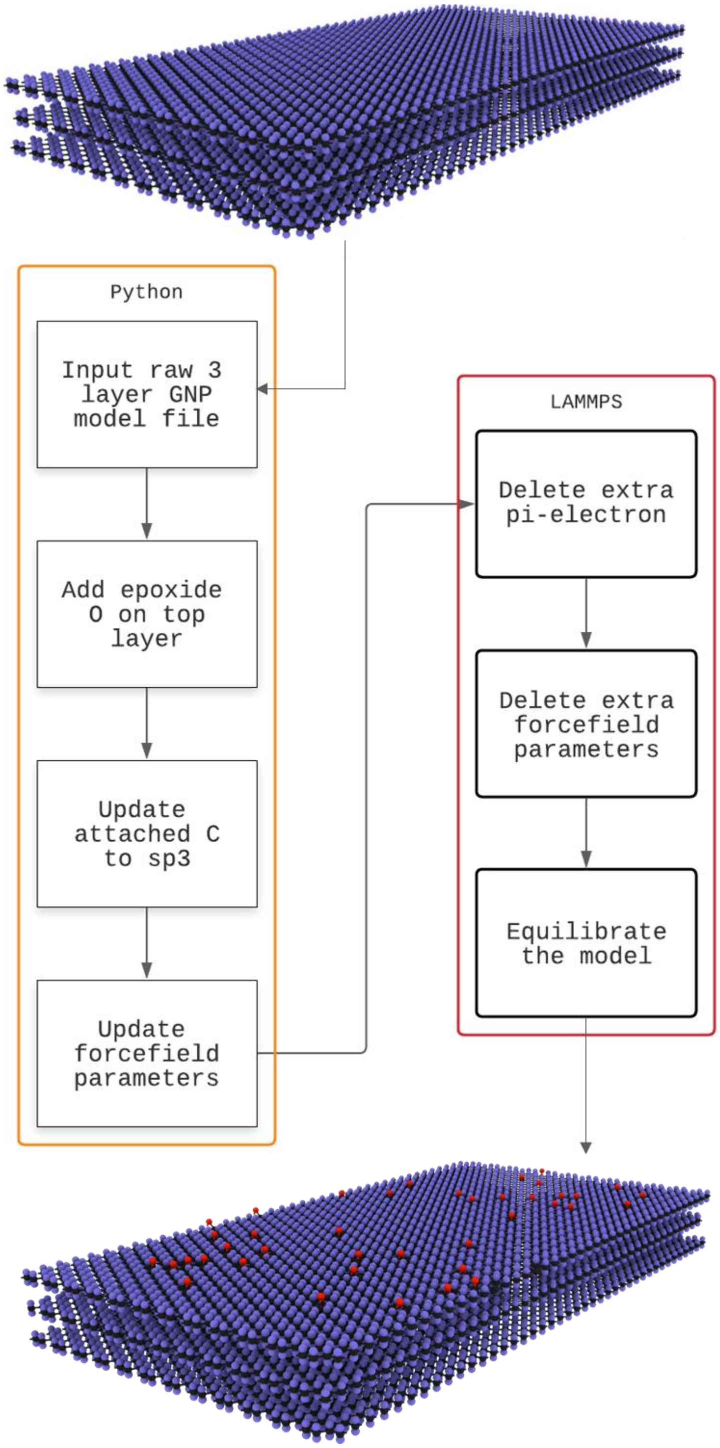

Figure 5.4. Flowchart to generate functionalizations on the GNP top-layer.

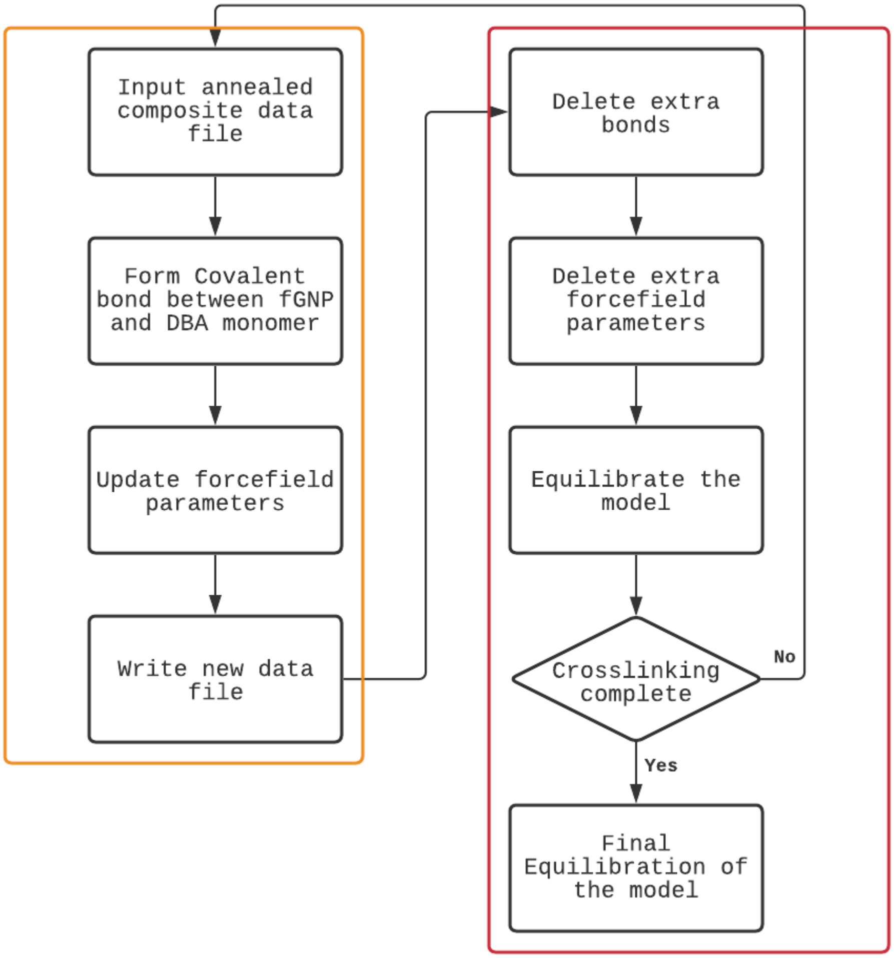

Figure 5.5. Flowchart for generating interfacial covalent bonds. Steps under yellow box were executed using Python and steps under red box were executed using LAMMPS.

Next, the polymer molecules were crosslinked by performing the ene crosslink reactions [102, 130]. The REACTER protocol was implemented to perform all the ene reactions [69, 70]. Although BMI resin is known to undergo multiple cure pathways, the ene reaction requires the lowest activation temperature [131]. When the two reactive monomers are mixed in equimolar ratio, the ene pathway consumes maximum number of reactive sites [132]. Most of the other pathways require an imbalance in the molar ratio between the maleimide and the allyl groups [132]. There are various commercial BMI resins where the ratio is always imbalanced [133]. The simulation was performed using the NVT ensemble with the reaction probabilities set to 0.01% and the cut-off radius was set to 6 Å. Lower probabilities helped with maintaining the stability of the models.

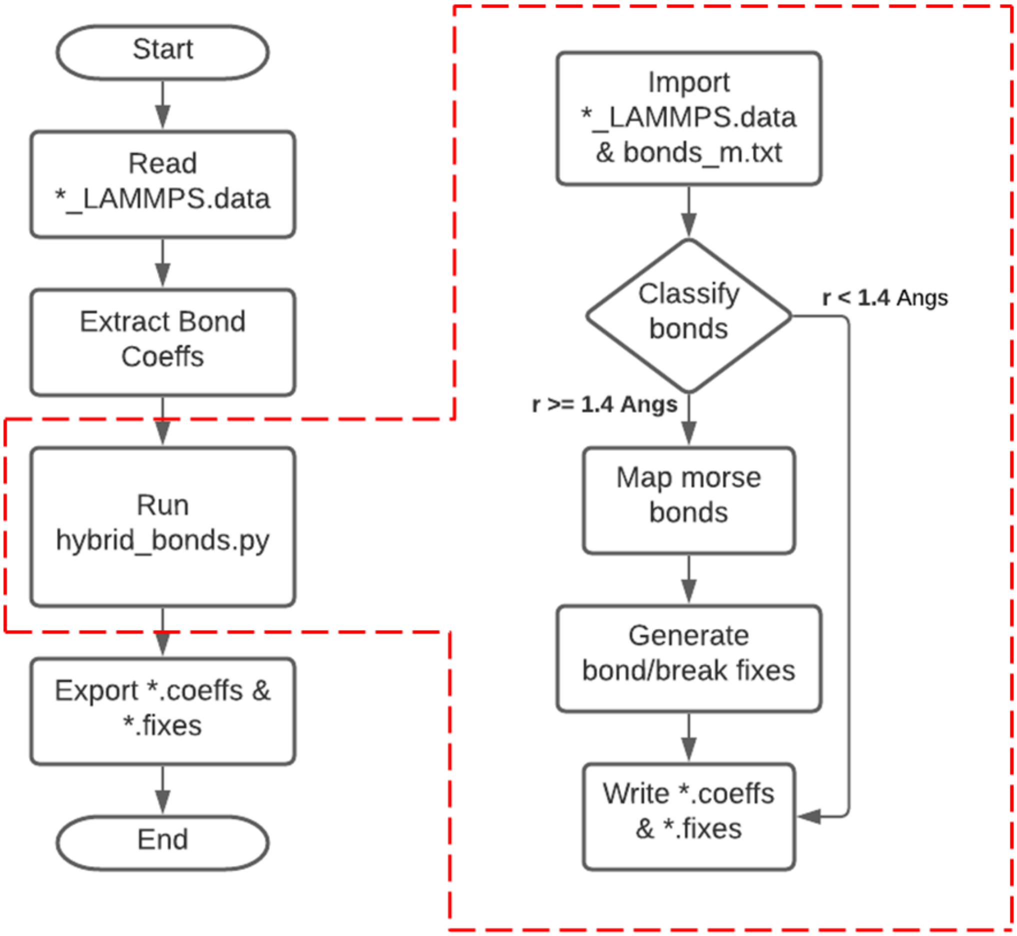

Figure 5.6. Flowchart for converting class-2 bonds to morse bonds.

Post-crosslinking, the models were equilibrated using the NPT ensemble over 1 ns. The equilibration simulation was performed in two parts. The first run was performed using the NPT ensemble over 1 ns. The temperature was ramped down from 300 K to 30 K over 0.5 ns and then maintained at 30 K for another 0.5 ns. During this run the bonds were maintained in class-2 configuration, so no morse bonds in the model. For second run the morse bonds were turned on for all the bonds with the equilibrium bond distance more than 1.4 Å. The run was performed at 30 K temperature using the NPT ensemble over 1 ns. The temperature of 30 K was carefully selected to limit the effect of thermal vibrations and improve the computational efficiency. For both the equilibration runs, the Z boundary was switched to periodic to allow complete relaxation.

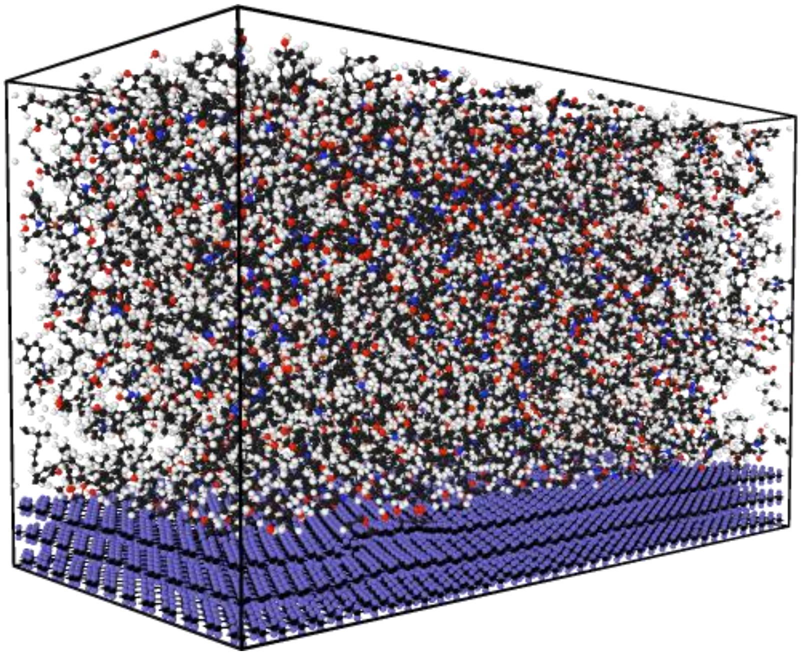

Figure 5.7. Representative fully equilibrated MD model of *f*GNP/BMI composite.

To convert the bonds from class-2 to morse an in-house Python module was used. Figure 5.6 shows the flowchart for implementing the conversion of class-2 bonds to morse bonds. The script requires a morse bond database and a LAMMPS data file to perform the conversion. The morse bond database was generated for a wide range of bonds and maintained a LAMMPS readable format. The output files include a *coeffs* file which contains the bond parameters for the hybrid bond style and the *fixes* file which contains the bond/break parameters for all the morse bonds. The bond/break parameters were maintained as per the "fix bond/break" command requirement in LAMMPS. The bond/break parameters allowed breaking of bonds when they were stretched to longer distances.

Also, the system temperature was lowered to 30 K. All the following simulations were performed at 30 K to reduce the thermal effects and improve the computational efficiency of the simulations. Next, another equilibration simulation was performed but with morse bonds enabled with identical settings. For both the equilibration runs, the z boundary was switched to periodic. Figure 5.7 shows a representative MD model after complete equilibration.

The fully equilibrated models were used to perform the pull-out simulation. Figure 5.8 shows the simulation setup. A uniform unidirectional force was applied to all the *f*GNP atoms in the in-plane X direction. The maximum applied force was 0.5 kcal/mol.Å (~ 34.7 pN). The atoms in the polymer layer were fixed to the center of mass by using a virtual spring with the stiffness of 1000 kcal/mol.Å^2. The polymer atoms maintained an NPT condition at 30 K temperature and 1 atm pressure. The *f*GNP atoms maintained an NVE condition. During the simulation, the total bond breaks were closely monitored, and a conditional halt was implemented when the number of bond breaks reached 1000. For all the 55 models, it was evident that peak pull-out force occurred well before the 1000 bond breaks. This condition was specific for these models since they were identically developed. The average applied force and displacement of the *f*GNP layers was computed.

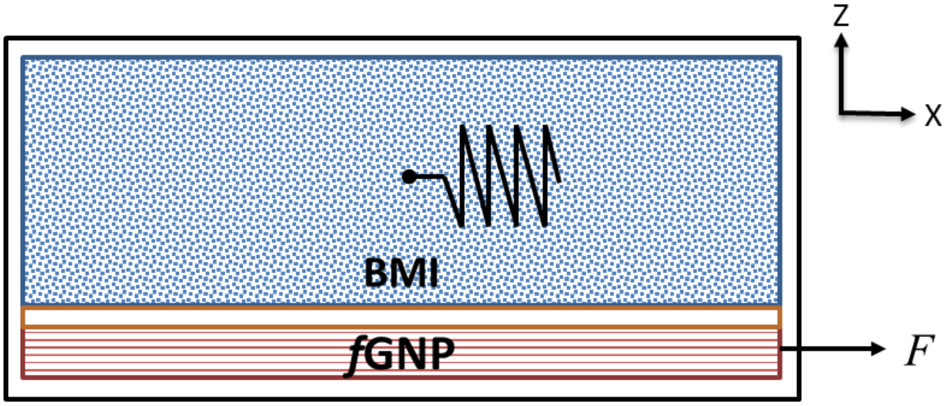

Figure 5.8. Pull-out simulation setup with boundary conditions.

5.2.2 Single Polymer Chain Strength

To establish the applicability of GCN as a surrogate model for MD simulations, a proof-of-concept study was performed. Where, a single polymer chain was subjected to uniaxial tension simulations. The simulated polymer chains were divided into six structural variables. Figure 5.9 shows the MD-ML workflow that was implemented for this study. The figure also lists the six variables, the holder structure (E_H) is a set of edge atoms within the polymer chain which were fixed during the simulation, shown in Figure 5.11 (top-right). The puller atom (E_P) is the terminal sp^2 C atom which represents a graphitic atom. This atom was displaced using a constant displacement rate during the simulation. The three monomer units (M_1, M_2, M_3) were a combination of molecular structures shown in Figure 5.10. The total number of unique polymer chains was 3330. The functional groups (B_F) used to connect the puller atom to the rest of the chain are shown in Figure 5.11 (bottom). And the last variable was the bridge (B) which connected all the rest of the variables, shown in Figure 5.11 (top-left).

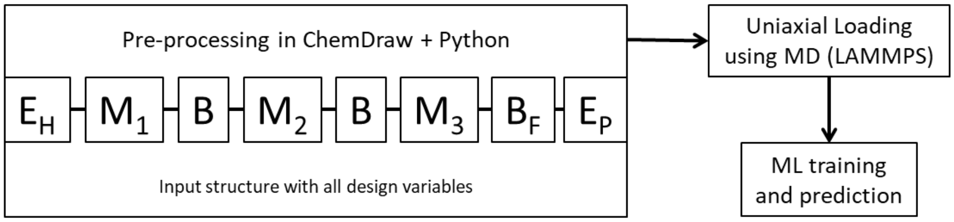

Figure 5.9. MD-ML workflow to predict failure in a single polymer chain. Where E_H is the holder structure, M_1 is the monomer unit 1, M_2 is the monomer unit 2, M_3 is the monomer unit 3, B is the bridge structure, B_F is the bridge structure with a functional group and E_P is the puller atom.

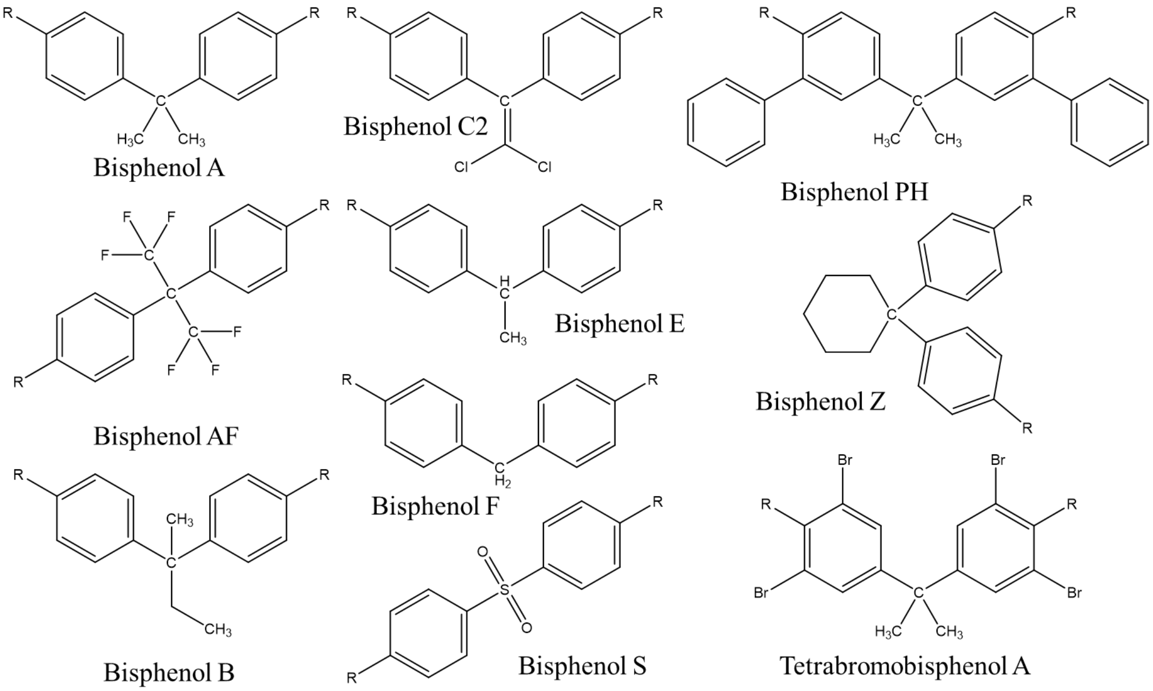

Figure 5.10. Molecular structures of all the monomer candidates. R represents either the bridge, puller, or holder.

All the individual structures were developed using the ChemScript suite, a commercial software. The ChemScript files were then converted to LAMMPS data files using an in-house Python script. The single chain uniaxial tension simulations were performed on all the 3330 structures over three iterations. The three runs were executed to account for statistical distribution of the mechanical response. The selection of boundary conditions and various simulation settings were rigorously evaluated. Appendix B discusses different simulation parameters that were used. The selected simulation settings include a dynamic run with a canonical ensemble (NVT) at 1 K temperature using a constant displacement rate of 0.01 Å/ps. Figure 5.12 shows the loading condition along with the critical design variables for the pure bisphenol A case. Morse bonds were included for simulating bond break. To generate the morse bonds an in-house Python script was used, flowchart shown in Figure 5.6.

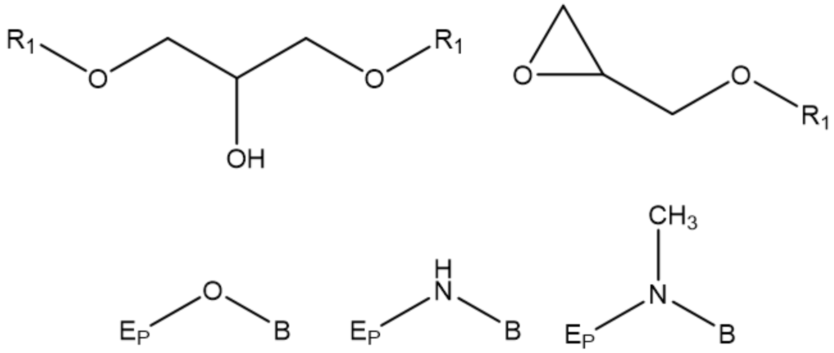

Figure 5.11. Molecular structure of the bridge (top-left), the holder (top-right), and the functional group structures (bottom).

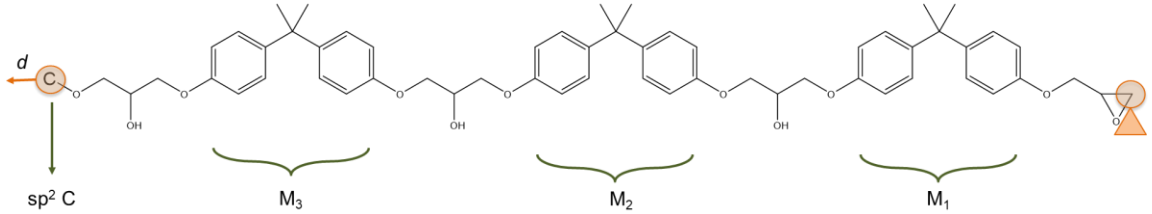

Figure 5.12. Boundary conditions for the pull-apart simulations for a pure bisphenol A chain.

5.3 Results

5.3.1 *f*GNP/BMI composite

Figure 5.13 shows the MD modeling space in terms of the degree of functionalization for each model and the corresponding extent of covalent bonding at the interface. A total of 55 models were developed using identical simulation steps. Pull-out simulations were performed on the same 55 models. The average applied force and the displacement of the *f*GNP layers were extracted.

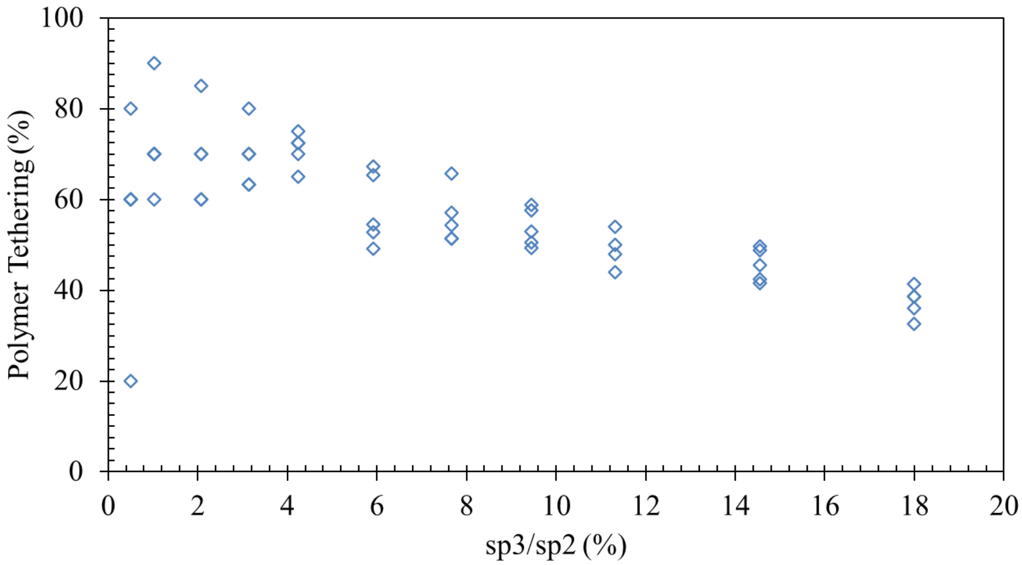

Figure 5.13. MD modeling space with the range of degree of functionalization and the corresponding interfacial crosslinking density.

Figure 5.14 shows four representative force-displacement plots for the models with the sp^3/sp^2 ratios of 0.51 %, 1.03 %, and two with 3.14%. Similar data was compiled for all the models. For consistency, all the force-displacement plots were post-processed using smoothening window of 5. The maximum or peak force was used to represent the pull-out force for individual models. Comparing the three different sp^3/sp^2 ratios results, increase in the interfacial crosslinks provides higher pull-out force. Next, comparing the two models with identical sp^3/sp^2 ratios, both the pull-out displacement and the maximum pull-out force are significantly different. From Figure 5.14 the stochastic nature of pull-out force is evident. Therefore, a ML-based surrogate model is the optimal choice to evaluate the proposed improvements to the ISS.

The data from the GNP pull-out simulations will be used as training data for a GCN model. The input to the GCN will be a graph representation of an *f*GNP model, where the graph captures the chains of polymers bonded to the functionalized GNP. Key features represented in a graph may include the polymer and *f*GNP chemistry, functional or reactive groups in the system, local chemical environments, and various energy terms obtained from the applied force field parameters. Information about the degree of functionalization and spatial distribution of functionalization sites will also be provided to the GCN. The GCN model will be trained to predict the pull-out force for a given MD model. Once trained, the GCN model will be capable of predicting pull-out forces in a fraction of the time required to determine GNP pull-out forces via MD simulations.

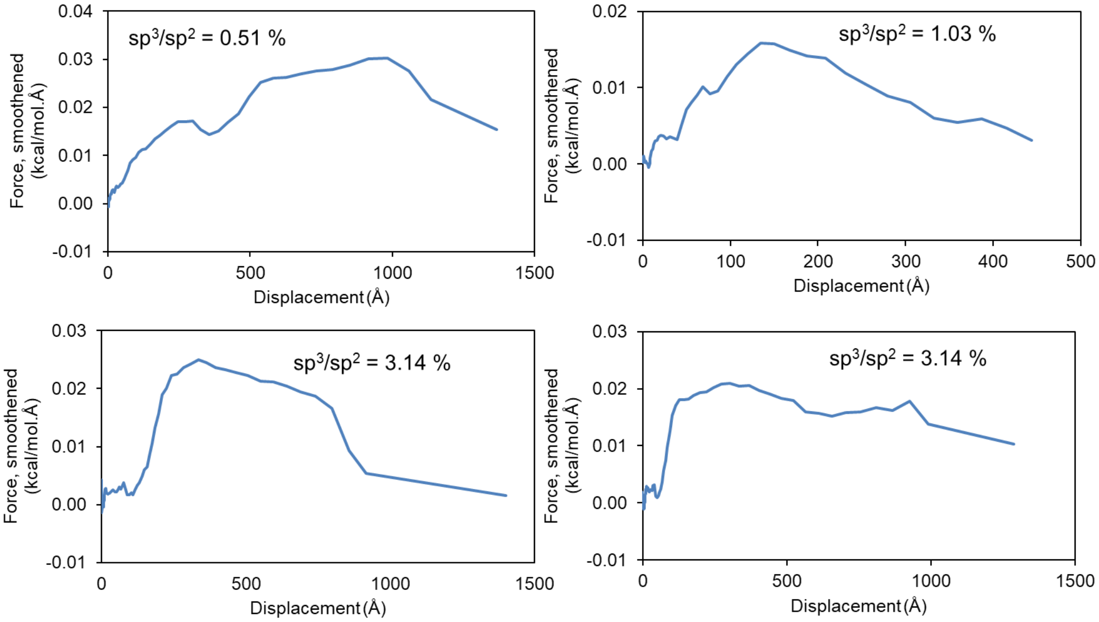

Figure 5.14. Four representative force-displacement curves.

With the trained GCN acting as a surrogate model, the identification of functionalization strategies that maximize pull-out force will be expedited. First, an optimization of pull-out force will be completed. In this optimization, the trained GCN will be used to thoroughly explore the functionalization strategy design space without simulating new *f*GNP models. Through the pull-out force predictions, *f*GNP models associated with the largest pull-out forces will be identified. The identified *f*GNP models will then be simulated to validate the

GCN’s largest pull-out force predictions. Next, key functionalization features related to pull-out forces will be identified. In this step, functionalization strategy metrics will be extracted from all *f*GNP models. The comparison of functionalization strategy metrics for *f*GNP models with large and small pull-out forces can be used to reveal functionalization features that maximize ISS.

5.3.2 Single Polymer Chain Strength

Figure 5.15. Snapshot of chain failure. Image generated using OVITO[63]. Highlighted in red spheres are the atoms associated with the broken bond.

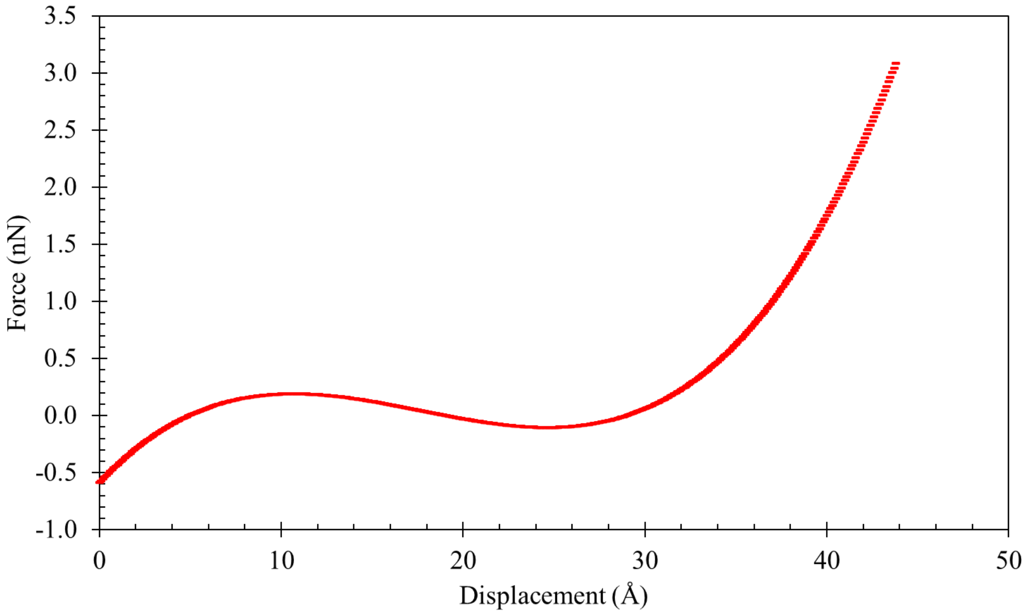

Figure 5.16. Representative force-displacement response from single chain failure.

The 3330 polymer chains were subjected to uniaxial loading with a constant displacement rate of 0.01 Å/ps. When the bonds reached threshold distance, bond/breaks were implemented to simulate bond scission. A conditional halt was implemented to stop the simulation after 1 bond break. Since the goal of this proof-of-concept was to establish a working GCN model, the only data of interest was the force-displacement data at the onset of failure. In a simple structure like a standalone polymer chain, a single bond break generates the onset of failure. Figure 5.15 shows the snapshot captured just after the first bond break in a pure bisphenol A chain. Figure 5.16 shows the corresponding force-displacement curve with the maximum or critical force of 3.09 pN.

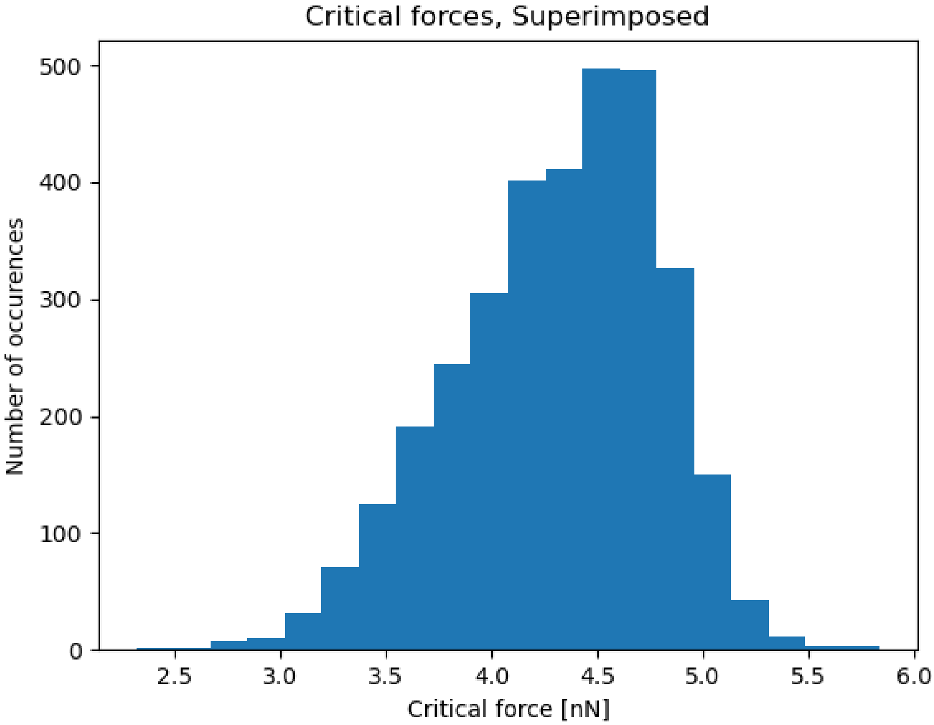

Figure 5.17. Distribution of critical forces for all the simulated cases.

To run a large amount of MD simulations, a bash-LAMMPS parallel script was developed which automated the data generation. The distribution of critical force for all the models is shown in Figure 5.17. Using the same setup, the two additional runs were performed. GCN used for this work was developed by Dr. Ashley Spear's research group at the University of Utah. Predictions made by the GCN are shown in form of Pearson correlation in Figure 5.18 [134]. The training-testing data split was achieved by using the data from each of the three runs against the data from the remaining two runs and a superimposed (all three together) data. The results indicate that the Pearson correlation coefficients were significantly lower than ideal value of 1. The GCN was erratic in predicting the critical force, however the lesson learnt from this study was that it can be used to represent the molecular structures.

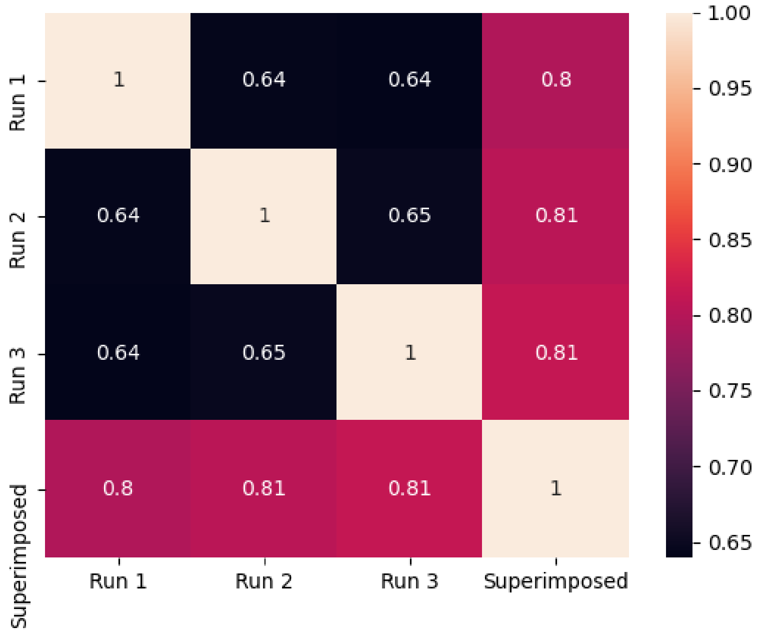

Figure 5.18. Pearson correlation from GCN predictions.

5.4 Conclusion

The results of this study indicate that MD simulations can be used to generate high-fidelity data for training an ML model. The inclusion of a wide range of degree of functionalizations will help identify the optimal functionalization strategy that improves the ISS. In addition, finer details, like local chemical environments, functionalization characteristics, and bulk matrix properties, can be linked to the optimization of the ISS. The proof-of-concept study helped established the usability of GCN for optimizing MD simulation data. For the *f*GNP/BMI models, the GCN model can help with understanding the underlying features that directly and indirectly affect the ISS by providing a surrogate model to rapidly link atomic structure to pull-out force. From this work, understanding of the structure-property relationship for carbon-based polymer matrix composites can be improved. This understanding will assist in fabricating superior carbon-based polymer matrix composites for next generation of spacecrafts.

6 Recommendations for future work

6.1 ReaxFF force field

All the MD simulations in this research were performed using the IFF and IFF-R force field. The simulations performed in Chapter 3 and Chapter 5 include a set of mechanical simulations. These simulations cause bond stretching which can induce certain reactive events like bond scissions, new bond formations, and but not limited to chemical transformations. ReaxFF force field has several parameterizations that can be used which can be beneficial since reactivity is the default feature. A major challenge will be benchmarking the simulation size and boundary conditions since ReaxFF is a computationally expensive force field. For perspective, simulations with IFF-R are close to 120% more efficient [25]. However, ReaxFF will help alleviate the user involvement in alterations to the mechanical simulations.

6.2 Impact Modifiers and Additives

Impact modifiers are a common component in high performance polymer resins. These materials are added to the resin to enhance the impact properties like impact strength and toughness [135, 136]. Usually, these materials are non-reactive and do not transform during the manufacturing process. The presence of these materials results in the formation of interpenetrating polymer network or IPN. IPN is a “spaghetti” type mixture of individual chains where there is a sub-network of crosslinks. This sub-network is a result of the resin polymerization. The impact modifiers in the IPN are non-reactive chains that align within the sub-network. Inclusion of an impact modifier has benefits if there is a balance between the mixed mass fractions. Excessive composition can result in degradation of some of the thermo-mechanical properties [135].

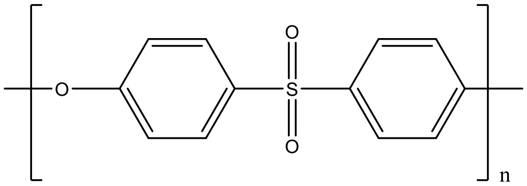

Figure 6.1. Molecular structure of polyether sulfone (PES). Where *n* is an integer representing the total number of repeating units.

During the research conducted in Chapter 4, some initial modeling and interaction energy analysis was performed for three cases of flCNT/epoxy composites with varying amount of polyether sulfone (PES). PES is an impact modifier which is commonly used as an additive in aerospace resins [135, 136]. Figure 6.1 shows the chemical structure of the PES. The three cases were classified based on the value of repeating units (*n* =1,2,3). Varying *n* resulted in different molecular weight of the PES molecule. The modeling steps were identical to section 4.2, with the PES molecule mixed with the two epoxy components. The mass fraction of PES in the flCNT/epoxy nanocomposite was varied from 3% to 39% with the total of 6 models for each molecular weight of PES (total models = 19).

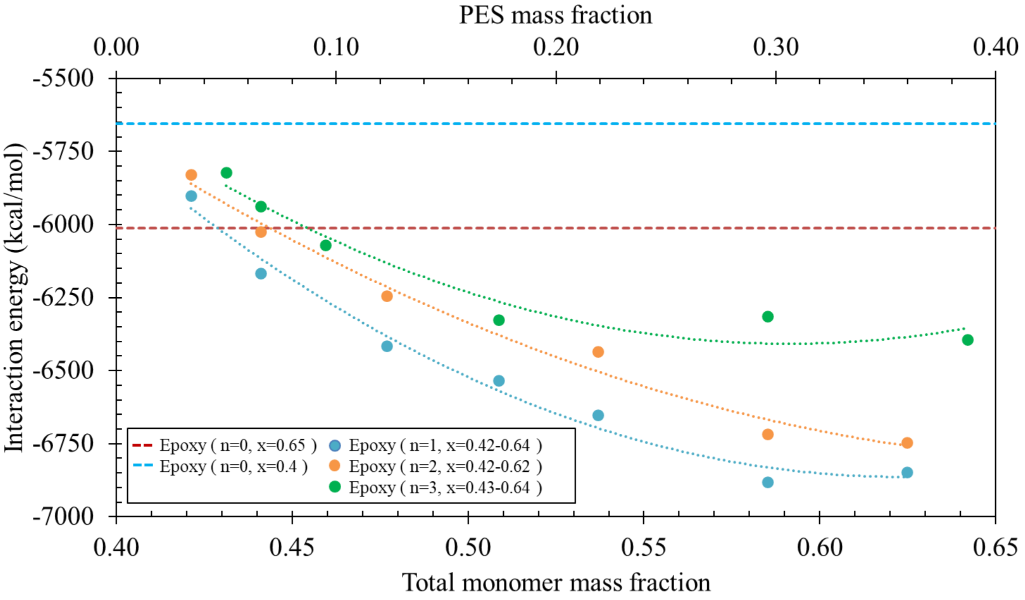

Figure 6.2. Interaction energy between polymer and flCNT with varying amount of PES with three different molecular weights. *n* = Total number of repeating units for each molecular weight of PES, *x* = Total monomer mass fraction (including PES). Dotted lines (*n*=0) represent interaction energy of the polymer without PES.

Figure 6.2 shows the interaction energy prediction for the three cases but only for the monomer case (no polymerization). The results show that PES significantly enhances the interaction of the polymer atoms with the graphitic surface of the flCNT. Varying the molecular weight also influences the interaction energy. As the PES molecule size increases, the lower the interaction energy. Also, from Figure 6.2, the dotted lines signify the interaction energy range from polymer without PES and again it is clear that inclusion of PES benefits the interaction. Additional analysis is included in Appendix C.

With the preliminary analysis, an in-depth study can be beneficial to fully understand the role of impact modifiers and additives on the interfacial properties of a flCNT composite. The potential study can include-

1. Interaction energy after polymerization and in presence of IPN
2. Frictional resistance with IPN
3. Transverse strength with IPN

6.3 Machine Learning for ISS prediction

The current modeling effort for the MD simulation includes a lot of conditions that are essential to complete the much-required training data for the ML algorithm. However, these conditions are a problem since they restrict the design space. These conditions include the 1000 bond break exit condition and converting the structure files to hybrid format which was discussed in detail in Chapter 5. The set conditions during the pull-out simulations can be easily relieved by switching the force field from IFF-R to ReaxFF. With ReaxFF the entire interfacial failure can be accurately captured without any topology-based errors.

The current modeling space for the training dataset includes 55 unique MD models with 55 corresponding mechanical responses. This number can be easily increases without going through the entire MD modeling procedure. All the mechanical response simulations were performed with an axial force applied in X direction. By changing the direction of the applied force, it will be easy to increase the training dataset. Performing these simulations will only need a small variable change in the LAMMPS input script.

7 References

1. Desai, A.V. and M.A. Haque, *Mechanics of the interface for carbon nanotube–polymer composites.* Thin-Walled Structures, 2005. **43**(11): p. 1787-1803.
2. Chen, J., et al., *Interfacial characteristics of carbon nanotube-polymer composites: A review.* Composites Part A: Applied Science and Manufacturing, 2018. **114**: p. 149-169.
3. Eitan, A., et al., *Surface Modification of Multiwalled Carbon Nanotubes: Toward the Tailoring of the Interface in Polymer Composites.* Chemistry of Materials, 2003. **15**(16): p. 3198-3201.
4. Liu, C., et al., *Enhanced mechanical and tribological properties of graphene/bismaleimide composites by using reduced graphene oxide with non-covalent functionalization.* Composites Part B: Engineering, 2019. **165**: p. 491-499.
5. Cheng, Q., et al., *Functionalized carbon-nanotube sheet/bismaleimide nanocomposites: mechanical and electrical performance beyond carbon-fiber composites.* Small, 2010. **6**(6): p. 763-7.
6. Bandyopadhyay, A., et al., *Molecular modeling of crosslinked epoxy polymers: The effect of crosslink density on thermomechanical properties.* Polymer, 2011. **52**(11): p. 2445-2452.
7. Odegard, G., T. Clancy, and T. Gates, *Prediction of Mechanical Properties of Polymers with Various Force Fields*, in *46th AIAA/ASME/ASCE/AHS/ASC Structures, Structural Dynamics and Materials Conference*. 2005, American Institute of Aeronautics and Astronautics.
8. Odegard, G.M., et al., *Molecular Dynamics Modeling of Epoxy Resins Using the Reactive Interface Force Field.* Macromolecules, 2021. **54**(21): p. 9815-9824.
9. Radue, M.S., et al., *Comparing the Mechanical Response of Di-, Tri-, and Tetra-functional Resin Epoxies with Reactive Molecular Dynamics.* J Polym Sci B Polym Phys, 2018. **56**(3): p. 255-264.
10. Li, C. and A. Strachan, *Molecular dynamics predictions of thermal and mechanical properties of thermoset polymer EPON862/DETDA.* Polymer, 2011. **52**(13): p. 2920-2928.
11. Vashisth, A., et al., *Effect of chemical structure on thermo-mechanical properties of epoxy polymers: Comparison of accelerated ReaxFF simulations and experiments.* Polymer, 2018. **158**: p. 354-363.
12. Chowdhury, S.C. and T. Okabe, *Computer simulation of carbon nanotube pull-out from polymer by the molecular dynamics method.* Composites Part A: Applied Science and Manufacturing, 2007. **38**(3): p. 747-754.
13. Allison, J., D. Backman, and L. Christodoulou, *Integrated computational materials engineering: A new paradigm for the global materials profession.* JOM, 2006. **58**(11): p. 25-27.
14. Shah, S., et al., *Multiscale Modeling for Virtual Manufacturing of Thermoset Composites*, in *AIAA Scitech 2020 Forum*. 2020, American Institute of Aeronautics and Astronautics.

15. Hinchliffe, A., *Molecular Modelling for Beginners*. Second ed. 2008, United Kingdom: John Wiley & Sons Ltd.
16. Tuckerman, M.E., *Ab initio molecular dynamics: basic concepts, current trends and novel applications.* Journal of Physics: Condensed Matter, 2002. **14**(50): p. R1297-R1355.
17. D.A. Case, H.M.A., K. Belfon, I.Y. Ben-Shalom, J.T. Berryman, S.R. Brozell, D.S. Cerutti, T.E. Cheatham, III, G.A. Cisneros, V.W.D. Cruzeiro, T.A. Darden, R.E. Duke, G. Giambasu, M.K. Gilson, H. Gohlke, A.W. Goetz, R. Harris, S. Izadi, S.A. Izmailov, K. Kasavajhala, M.C. Kaymak, E. King, A. Kovalenko, T. Kurtzman, T.S. Lee, S. LeGrand, P. Li, C. Lin, J. Liu, T. Luchko, R. Luo, M. Machado, V. Man, M. Manathunga, K.M. Merz, Y. Miao, O. Mikhailovskii, G. Monard, H. Nguyen, K.A. O'Hearn, A. Onufriev, F. Pan, S. Pantano, R. Qi, A. Rahnamoun, D.R. Roe, A. Roitberg, C. Sagui, S. Schott-Verdugo, A. Shajan, J. Shen, C.L. Simmerling, N.R. Skrynnikov, J. Smith, J. Swails, R.C. Walker, J Wang, J. Wang, H. Wei, R.M. Wolf, X. Wu, Y. Xiong, Y. Xue, D.M. York, S. Zhao, and P.A. Kollman, *Amber 2022.* University of California, San Francisco, 2022.
18. Jorgensen, W.L., D.S. Maxwell, and J. Tirado-Rives, *Development and Testing of the OPLS All-Atom Force Field on Conformational Energetics and Properties of Organic Liquids.* Journal of the American Chemical Society, 1996. **118**(45): p. 11225-11236.
19. MacKerell Jr, A.D., et al., *All-atom empirical potential for molecular modeling and dynamics studies of proteins.* The journal of physical chemistry B, 1998. **102**(18): p. 3586-3616.
20. Brooks, B.R., et al., *CHARMM: A program for macromolecular energy, minimization, and dynamics calculations.* Journal of Computational Chemistry, 1983. **4**(2): p. 187-217.
21. Heinz, H., et al., *Thermodynamically consistent force fields for the assembly of inorganic, organic, and biological nanostructures: the INTERFACE force field.* Langmuir, 2013. **29**(6): p. 1754-65.
22. Sun, H., *COMPASS: An ab Initio Force-Field Optimized for Condensed-Phase ApplicationsOverview with Details on Alkane and Benzene Compounds.* The Journal of Physical Chemistry B, 1998. **102**(38): p. 7338-7364.
23. Sun, H., et al., *An ab Initio CFF93 All-Atom Force Field for Polycarbonates.* Journal of the American Chemical Society, 1994. **116**(7): p. 2978-2987.
24. van Duin, A.C.T., et al., *ReaxFF: A Reactive Force Field for Hydrocarbons.* The Journal of Physical Chemistry A, 2001. **105**(41): p. 9396-9409.
25. J. Winetrout, K.K., G. Sachdeva, R. Pandey, B. Damirchi, A. van Duin, G. Odegard, H. Heinz, *Implementing Reactivity in Molecular Dynamics Simulations with the Interface Force Field (IFF-R) and Other Harmonic Force Fields*. 2021: arXiv:2107.14418.
26. Cottrell, T.L., *The strengths of chemical bonds*. 1958: Butterworths Scientific Publications.
27. Iijima, S., *Helical microtubules of graphitic carbon.* Nature, 1991. **354**(6348): p. 56-58.

28. De Volder Michael, F.L., et al., *Carbon Nanotubes: Present and Future Commercial Applications.* Science, 2013. **339**(6119): p. 535-539.
29. Herrera-Herrera, A.V., et al., *Carbon nanotubes applications in separation science: A review.* Analytica Chimica Acta, 2012. **734**: p. 1-30.
30. Siochi, E.J. and J.S. Harrison, *Structural nanocomposites for aerospace applications.* MRS Bulletin, 2015. **40**(10): p. 829-835.
31. Downes, R.D., et al., *Geometrically constrained self-assembly and crystal packing of flattened and aligned carbon nanotubes.* Carbon, 2015. **93**: p. 953-966.
32. Jolowsky, C., et al., *Microstructure evolution and self-assembling of CNT networks during mechanical stretching and mechanical properties of highly aligned CNT composites.* Composites Science and Technology, 2018. **166**: p. 125-130.
33. Gu, G.X., C.-T. Chen, and M.J. Buehler, *De novo composite design based on machine learning algorithm.* Extreme Mechanics Letters, 2018. **18**: p. 19-28.
34. Rupp, M., R. Ramakrishnan, and O.A. von Lilienfeld, *Machine Learning for Quantum Mechanical Properties of Atoms in Molecules.* The Journal of Physical Chemistry Letters, 2015. **6**(16): p. 3309-3313.
35. von Lilienfeld, O.A., et al., *Fourier series of atomic radial distribution functions: A molecular fingerprint for machine learning models of quantum chemical properties.* International Journal of Quantum Chemistry, 2015. **115**(16): p. 1084-1093.
36. Wang, Y., J.M. Lamim Ribeiro, and P. Tiwary, *Machine learning approaches for analyzing and enhancing molecular dynamics simulations.* Current Opinion in Structural Biology, 2020. **61**: p. 139-145.
37. Chmiela, S., et al., *Machine learning of accurate energy-conserving molecular force fields.* Science Advances. **3**(5): p. e1603015.
38. Alred, J.M., et al., *Machine learning electron density in sulfur crosslinked carbon nanotubes.* Composites Science and Technology, 2018. **166**: p. 3-9.
39. Rahman, A., et al., *A machine learning framework for predicting the shear strength of carbon nanotube-polymer interfaces based on molecular dynamics simulation data.* Composites Science and Technology, 2021. **207**.
40. Plepys, A.R., *A study of residual stress formation in threedimensionally constrained epoxy resins*, in *Department of Polymer Science and Engineering*. 2014, University of Massachusetts Amherst: MA, USA.
41. Hoa, S.V., P. Ouellette, and T.D. Ngo, *Determination of Shrinkage and Modulus Development of Thermosetting Resins.* Journal of Composite Materials, 2009. **43**(7): p. 783-803.
42. Müller, J., Müller-Pabel, M., Lorenz, N., Gröger, B., Gerritzen, J., Gude, M., & Hopmann, C., *Visco-thermo-elastic Simulation Approach For Prediction of Cure-induced Residual Stresses in Fiber Reinforced Composites*, in *ESAFORM 2021. 24th International Conference on Material Forming*. 2021: Liège, Belgique.
43. Al Mahmud, H., et al., *Multiscale modeling of carbon fiber- graphene nanoplatelet-epoxy hybrid composites using a reactive force field.* Composites Part B: Engineering, 2019. **172**: p. 628-635.

44. Odegard, G.M., et al., *Predicting mechanical response of crosslinked epoxy using ReaxFF.* Chemical Physics Letters, 2014. **591**: p. 175-178.
45. Gartner, T.E. and A. Jayaraman, *Modeling and Simulations of Polymers: A Roadmap.* Macromolecules, 2019. **52**(3): p. 755-786.
46. Fan, J., et al., *Molecular dynamics predictions of thermomechanical properties of an epoxy thermosetting polymer.* Polymer, 2020. **196**.
47. Hadden, C.M., et al., *Mechanical properties of graphene nanoplatelet/carbon fiber/epoxy hybrid composites: Multiscale modeling and experiments.* Carbon, 2015. **95**: p. 100-112.
48. Masoumi, S., B. Arab, and H. Valipour, *A study of thermo-mechanical properties of the cross-linked epoxy: An atomistic simulation.* Polymer, 2015. **70**: p. 351-360.
49. B. Arab, A.S., *Molecular Dynamics Simulation of Cross-Linked Epoxy Polymers: the Effect of Force Field on the Estimation of Properties.* Journal of Nano- and Electronic Physics, 2013. **5**.
50. Tack, J.L. and D.M. Ford, *Thermodynamic and mechanical properties of epoxy resin DGEBF crosslinked with DETDA by molecular dynamics.* J Mol Graph Model, 2008. **26**(8): p. 1269-75.
51. Park, H. and M. Cho, *A multiscale framework for the elasto-plastic constitutive equations of crosslinked epoxy polymers considering the effects of temperature, strain rate, hydrostatic pressure, and crosslinking density.* Journal of the Mechanics and Physics of Solids, 2020. **142**.
52. Yang, S. and J. Qu, *Computing thermomechanical properties of crosslinked epoxy by molecular dynamic simulations.* Polymer, 2012. **53**(21): p. 4806-4817.
53. Pandiyan, S., et al., *A molecular dynamics study of water transport inside an epoxy polymer matrix.* Computational Materials Science, 2015. **106**: p. 29-37.
54. Knox, C., et al. *HIGH STRAIN RATE MECHANICAL BEHAVIOR OF EPOXY NETWORKS FROM MOLECULAR DYNAMICS SIMULATIONS*. in *27th Army Science Conference Proceedings, 2010*. 2010.
55. Gaikwad, P.S., et al., *Understanding the Origin of the Low Cure Shrinkage of Polybenzoxazine Resin by Computational Simulation.* ACS Applied Polymer Materials, 2021. **3**(12): p. 6407-6415.
56. Patil, S.U., et al., *Reactive Molecular Dynamics Simulation of Epoxy for the Full Cross-Linking Process.* ACS Applied Polymer Materials, 2021. **3**(11): p. 5788-5797.
57. Deshpande, P., Shah, S., Patil, S., Kashmari, K., Olaya, M., Odegard, G., Maiaru, M. *Multiscale Modelling of the Cure Process in Thermoset Polymers Using ICME*. in *Proceedings of the American Society for Composites—Thirty-fifth Technical Conference 2020*. 2020. New Jersey: American Society for Composites.
58. Deshpande, P., Shah, S., Patil, S., Kashmari, K., Odegard, G., Maiaru, M. *A multi-scale approach for modelling the cure of thermoset polymers within ICME*. in *Proceedings of the American Society for Composites—Thirty-fourth Technical Conference 2019*. 2019. Atlanta, GA: American Society for Composites.
59. *Technical Data Sheet: EPON Resin 828*. 2021, Hexion Inc.

60. *Technical Bulletin: Jeffamine D-230 Polyetheramine*. 2015, Huntsman Corporation.
61. Bruce Burton, D.A., Howard Klein, Angela Garibay-Vasquez, Alan Pekarik, Chris Henkee, *Epoxy Formulations Using Jeffamine Polyetheramines*. 2005, Huntsman Corporation: USA. p. 103.
62. Plimpton, S., *Fast Parallel Algorithms for Short-Range Molecular Dynamics.* Journal of Computational Physics, 1995. **117**(1): p. 1-19.
63. Stukowski, A., *Visualization and analysis of atomistic simulation data with OVITO–the Open Visualization Tool.* Modelling and Simulation in Materials Science and Engineering, 2009. **18**(1): p. 015012.
64. Martyna, G.J., D.J. Tobias, and M.L. Klein, *Constant pressure molecular dynamics algorithms.* The Journal of Chemical Physics, 1994. **101**(5): p. 4177-4189.
65. Tuckerman, M.E., et al., *A Liouville-operator derived measure-preserving integrator for molecular dynamics simulations in the isothermal–isobaric ensemble.* Journal of Physics A: Mathematical and General, 2006. **39**(19): p. 5629-5651.
66. Shinoda, W., M. Shiga, and M. Mikami, *Rapid estimation of elastic constants by molecular dynamics simulation under constant stress.* Physical Review B, 2004. **69**(13).
67. M. Parrinello, A.R., *Polymorphic transitions in single crystals: A new molecular dynamics method.* Journal of Applied Physics, 1981. **52**(12): p. 234505.
68. E. Polak, G.R., *Note sur la convergence de methodes de directions conjuguees.* Revue Francaise d'lnformatique et de Recherche Operationnelle, 1969. **16**: p. 35-43.
69. Gissinger, J.R., B.D. Jensen, and K.E. Wise, *REACTER: A Heuristic Method for Reactive Molecular Dynamics.* Macromolecules, 2020. **53**(22): p. 9953-9961.
70. Gissinger, J.R., B.D. Jensen, and K.E. Wise, *Chemical Reactions in Classical Molecular Dynamics.* Polymer (Guildf), 2017. **128**: p. 211-217.
71. Flory, P.J., *Molecular size distribution in three dimensional polymers. I. Gelation1*. JACS Au, 1941. **63**(11): p. 3083.
72. Hädicke, E. and H. Stutz, *Comparison of the structure of step-growth networks obtained by Monte Carlo simulation and branching theory.* Journal of Applied Polymer Science, 2002. **85**(5): p. 929-935.
73. Varshney, V., et al., *A Molecular Dynamics Study of Epoxy-Based Networks: Cross-Linking Procedure and Prediction of Molecular and Material Properties.* Macromolecules, 2008. **41**(18): p. 6837-6842.
74. OriginPro. 2020b, OriginLab Corporation: Northampton, MA, USA.
75. F. P. Beer, E.R.J., J. T. Dewolf, D. F. Mazurek, *Mechanics of Materials*. 6th ed. 2012, New York: McGraw-Hill.
76. Knorr, D.B., et al., *Overcoming the structural versus energy dissipation trade-off in highly crosslinked polymer networks: Ultrahigh strain rate response in polydicyclopentadiene.* Composites Science and Technology, 2015. **114**: p. 17-25.
77. McAninch, I.M., *Molecular Toughening of Epoxy Networks*, in *Chemical Engineering*. 2014, Drexel University: Philadelphia, PA. p. 259.

78. Lee, A. and G.B. McKenna, *Effect of crosslink density on physical ageing of epoxy networks.* Polymer, 1988. **29**(10): p. 1812-1817.
79. Sirk, T.W., et al., *High strain rate mechanical properties of a cross-linked epoxy across the glass transition.* Polymer, 2013. **54**(26): p. 7048-7057.
80. Spencer, J.B., *Cure Shrinkage in Casting Resins*, U.S.D.o. Energy, Editor. 1961, Sandia National Laboratory.
81. Shan, L., *Effect of network structure of epoxy DGEBA-poly (oxypropylene) diamines on tensile behavior.* Journal of polymer science., 1999. **37**(19): p. 2815.
82. Zhou, G., S. Movva, and L.J. Lee, *Nanoclay and long-fiber-reinforced composites based on epoxy and phenolic resins.* Journal of Applied Polymer Science, 2008. **108**(6): p. 3720-3726.
83. Greaves, G.N., et al., *Poisson's ratio and modern materials.* Nature Materials, 2011. **10**(11): p. 823-837.
84. Park, J. and S.C. Jana, *Effect of Plasticization of Epoxy Networks by Organic Modifier on Exfoliation of Nanoclay.* Macromolecules, 2003. **36**(22): p. 8391-8397.
85. McGrath, L.M., et al., *Investigation of the thermal, mechanical, and fracture properties of alumina–epoxy composites.* Polymer, 2008. **49**(4): p. 999-1014.
86. Teh, P.L., et al., *Thermal and mechanical properties of particulate fillers filled epoxy composites for electronic packaging application.* Polymers for Advanced Technologies, 2008. **19**(4): p. 308-315.
87. NASA, *2020 NASA Technology Taxonomy*. 2020, NASA.
88. Kim, J.-W., et al., *Assessment of carbon nanotube yarns as reinforcement for composite overwrapped pressure vessels.* Composites Part A: Applied Science and Manufacturing, 2016. **84**: p. 256-265.
89. Kim, J.-W., et al., *Modifying carbon nanotube fibers: A study relating apparent interfacial shear strength and failure mode.* Carbon, 2021. **173**: p. 857-869.
90. Bellucci, S., et al., *CNT composites for aerospace applications.* Journal of Experimental Nanoscience, 2007. **2**(3): p. 193-206.
91. Baur, J. and E. Silverman, *Challenges and Opportunities in Multifunctional Nanocomposite Structures for Aerospace Applications.* MRS Bulletin, 2007. **32**(4): p. 328-334.
92. Zhe Liu, Y.-S.D., Matthew Lundblad, Ayou Hao and Zhiyong Liang, Youssef Aider and Yeqing Wang, *Lightweight and Flexible Thermal Protection Systems for High Temperature Composite Applications*, in *SAMPE 2020*. 2020: Virtual Series.
93. Kaiser, A.L., I.V. Albelo, and B.L. Wardle, *Fabrication of Aerospace-grade Epoxy and Bismaleimide Matrix Nanocomposites with High Density Aligned Carbon Nanotube Reinforcement*, in *AIAA Scitech 2020 Forum*. 2020, American Institute of Aeronautics and Astronautics.
94. Sandi G. Miller, J.K.S., Daniel A. Scheiman, Michael Maryanski, and Michelle Schlea, *STUDY OF OUT-TIME ON THE PROCESSING AND PROPERTIES OF IM7/977-3 COMPOSITES*, in *SAMPE 2010*. 2010: Seattle, WA.
95. Vincent J.Lopata, C.B.S., Ajit Singh, Christopher J.Janke, George E.Wrenn, Stephen J.Havens, *Electron-beam-curable epoxy resins for the manufacture of*

high-performance composites. Radiation Physics and Chemistry, 1999. **56**(4): p. 405-415.
96. Hundley, J.M., et al., *Multi-Scale Modeling of Metal-Composite Interfaces in Titanium-Graphite Fiber Metal Laminates Part I: Molecular Scale.* Open Journal of Composite Materials, 2011. **01**(01): p. 19-37.
97. Okabe, T., et al., *Curing reaction of epoxy resin composed of mixed base resin and curing agent: Experiments and molecular simulation.* Polymer, 2013. **54**(17): p. 4660-4668.
98. Song, Y., et al., *Carbon nanotube sensor thread for distributed strain and damage monitoring on IM7/977-3 composites.* Smart Materials and Structures, 2014. **23**(7).
99. Liu, Y., et al., *Shape memory polymers and their composites in aerospace applications: a review.* Smart Materials and Structures, 2014. **23**(2).
100. Patil, S.U., et al., *Interfacial characteristics between flattened CNT stacks and polyimides: A molecular dynamics study.* Computational Materials Science, 2020. **185**.
101. Pisani, W.A., et al., *Interfacial modeling of flattened CNT composites with cyanate ester and PEEK polymers.* Composites Part B: Engineering, 2021. **211**.
102. Deshpande, P.P., et al., *Prediction of the Interfacial Properties of High-Performance Polymers and Flattened CNT-Reinforced Composites Using Molecular Dynamics.* Langmuir, 2021. **37**(39): p. 11526-11534.
103. Pramanik, C., et al., *Carbon Nanotube Dispersion in Solvents and Polymer Solutions: Mechanisms, Assembly, and Preferences.* ACS Nano, 2017. **11**(12): p. 12805-12816.
104. Dharmawardhana, C.C., et al., *Reliable computational design of biological-inorganic materials to the large nanometer scale using Interface-FF.* Molecular Simulation, 2017. **43**(13-16): p. 1394-1405.
105. M. Parrinello, A.R., *Polymorphic transitions in single crystals: A new molecular dynamics method.* J Appl Phys, 1981. **52**(12): p. 7182-7190.
106. Solvay, *CYCOM 977-3*. Solvay.
107. Pisani, W.A., et al., *Multiscale modeling of PEEK using reactive molecular dynamics modeling and micromechanics.* Polymer, 2019. **163**: p. 96-105.
108. Maoshuai He, J.D., Kaili Zhang, Feng Ding, Hua Jiang, Annick Loiseau, Juha Lehtonen, and Esko I. Kauppinen, *Precise Determination ofthe Threshold Diameter for a Single-Walled Carbon Nanotube To Collapse.* ACS Nano, 2014. **8**(9): p. 9657-9663.
109. Bond, S.D. and B.J. Leimkuhler, *Stabilized Integration of Hamiltonian Systems with Hard-Sphere Inequality Constraints.* SIAM Journal on Scientific Computing, 2008. **30**(1): p. 134-147.
110. Jan-Eric Ehlers, N.G.R., Lam K. Huynh, Ha Pham, Maurice Marks, and Thanh N. Truong, *Theoretical Study on Mechanisms of the Epoxy-Amine Curing Reaction.* Macromolecules, 2007. **40**(12): p. 4370-4377.
111. Huber, T., A.E. Torda, and W.F. van Gunsteren, *Local elevation: A method for improving the searching properties of molecular dynamics simulation.* Journal of Computer-Aided Molecular Design, 1994. **8**(6): p. 695-708.

112. Radue, M., *Molecular Modeling of Aerospace Polymer Matrices Including Carbon Nanotube-Enhanced Epoxy*, in *Mechanical Engineering-Engineering Mechanics*. 2017, Michigan Technological University. p. 126.
113. Bogusz, S., T.E. Cheatham, and B.R. Brooks, *Removal of pressure and free energy artifacts in charged periodic systems via net charge corrections to the Ewald potential.* The Journal of Chemical Physics, 1998. **108**(17): p. 7070-7084.
114. Huber, R.G., et al., *Heteroaromatic pi-stacking energy landscapes.* J Chem Inf Model, 2014. **54**(5): p. 1371-9.
115. McGaughey, G.B., M. Gagne, and A.K. Rappe, *pi-Stacking interactions. Alive and well in proteins.* J Biol Chem, 1998. **273**(25): p. 15458-63.
116. Mutasem Omar Sinnokrot, E.F.V., and C. David Sherrill, *Estimates of the Ab Initio Limit for π−π Interactions: The Benzene Dimer.* J. Am. Chem. Soc., 2002. **124**(36): p. 10887-10893.
117. Mingjun Yang, V.K., and Michael Zaiser, *Interactions between Polymers and Carbon Nanotubes: A Molecular Dynamics Study.* J. Phys. Chem. B, 2005. **109**(20): p. 10009-10014.
118. Xu, H., J. Al-Ghalith, and T. Dumitrică, *Smooth sliding and superlubricity in the nanofriction of collapsed carbon nanotubes.* Carbon, 2018. **134**: p. 531-535.
119. Xu, H., et al., *Collapsed carbon nanotubes: From nano to mesoscale via density functional theory-based tight-binding objective molecular modeling.* Carbon, 2019. **143**: p. 786-792.
120. Liu, M., et al., *Diazonium functionalization of graphene nanosheets and impact response of aniline modified graphene/bismaleimide nanocomposites.* Materials & Design, 2014. **53**: p. 466-474.
121. Jensen, B.D., K.E. Wise, and G.M. Odegard, *Simulation of mechanical performance limits and failure of carbon nanotube composites.* Modelling and Simulation in Materials Science and Engineering, 2016. **24**(2): p. 025012.
122. Al Mahmud, H., et al., *Computational Modeling of Hybrid Carbon Fiber/Epoxy Composites Reinforced with Functionalized and Non-Functionalized Graphene Nanoplatelets.* Nanomaterials, 2021. **11**(11).
123. Odegard, G.M., et al., *Constitutive modeling of nanotube–reinforced polymer composites.* Composites Science and Technology, 2003. **63**(11): p. 1671-1687.
124. Frankland, S.J.V., et al., *Molecular Simulation of the Influence of Chemical Cross-Links on the Shear Strength of Carbon Nanotube−Polymer Interfaces.* The Journal of Physical Chemistry B, 2002. **106**(12): p. 3046-3048.
125. Zheng, Q., et al., *Computational analysis of effect of modification on the interfacial characteristics of a carbon nanotube–polyethylene composite system.* Applied Surface Science, 2009. **255**(6): p. 3534-3543.
126. Kipf, T.N. and M. Welling, *Semi-supervised classification with graph convolutional networks.* arXiv preprint arXiv:1609.02907, 2016.
127. Gao, H., Z. Wang, and S. Ji, *Large-Scale Learnable Graph Convolutional Networks*, in *Proceedings of the 24th ACM SIGKDD International Conference on Knowledge Discovery & Data Mining*. 2018, Association for Computing Machinery: London, United Kingdom. p. 1416–1424.

128. Zhang, S., et al., *Graph convolutional networks: a comprehensive review.* Computational Social Networks, 2019. **6**(1): p. 11.
129. Huntsman, *Advanced Materials: Matrimid 5292 A-2 Resin; Matrimid 5292 B Hardener*. 2010, Huntsman Corporation: Texas, USA.
130. Radue, M.S., et al., *Molecular Modeling of Cross-Linked Polymers with Complex Cure Pathways: A Case Study of Bismaleimide Resins.* Macromolecules, 2018. **51**(5): p. 1830-1840.
131. Morgan, R.J., et al., *Characterization of the cure reactions of bismaleimide composite matrices.* Polymer, 1997. **38**(3): p. 639-646.
132. Rozenberg, B.A., et al., *The cure mechanism of the 4,4'-(N, N'-bismaleimide)diphenylmethane-2,2'-diallylbisphenol A systems.* Polymer science. Series A, 2001. **43**(4): p. 386-399.
133. Lincoln, J.E., R.J. Morgan, and E.E. Shin, *Moisture absorption-network structure correlations in BMPM/DABPA bismaleimide composite matrices.* Journal of advanced materials, 2000. **32**(4): p. 24-34.
134. Benesty, J., et al., *Pearson correlation coefficient*, in *Noise reduction in speech processing*. 2009, Springer. p. 1-4.
135. Lee, S.-E., et al., *Improvement of the mechanical and thermal properties of polyethersulfone-modified epoxy composites.* Journal of Industrial and Engineering Chemistry, 2016. **33**: p. 73-79.
136. Rajangam, R., *Effect of polyethersulfone and N,N'-bismaleimido-4,4'-diphenyl methane on the mechanical and thermal properties of epoxy systems.* Express Polymer Letters - EXPRESS POLYM LETT, 2008. **2**: p. 339-348.

A Frictional Resistance Analysis

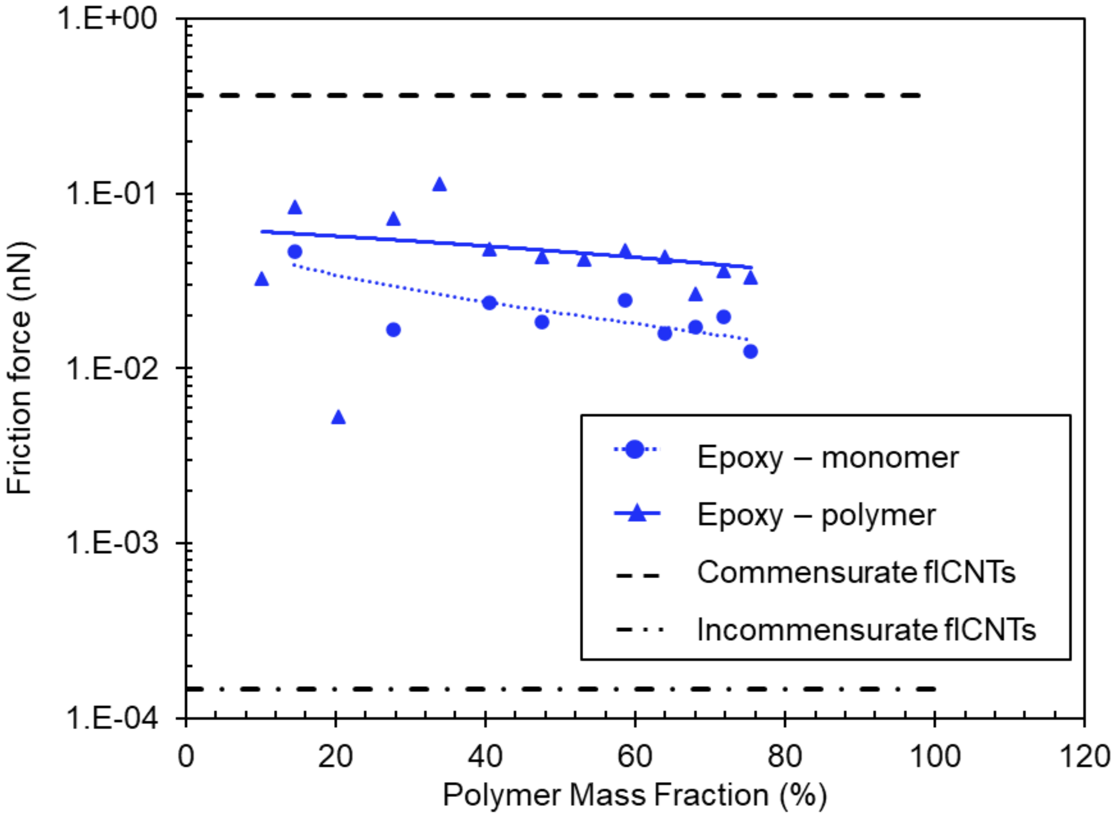

Figure A-1. Friction force as a function of polymer mass fraction at a velocity of 10 m/s for monomer and polymer cases, and commensurate/incommensurate flCNTs.

This section discusses the additional details of the friction simulations results. Figure A-2 shows friction force results as a function of the polymer mass fraction for the input velocity of 10 m/s. The linear fits are inserted for visual aid and do not hold any physical significance. Results clearly indicate that increasing the polymer mass fraction does not affect the friction force, it depends on the interfacial roughness from the chemical groups within the polymer. Additionally, from Figure A-3, the increase in velocity for the different polymer mass fractions showed a linear increase in the friction force for each mass fraction. This increment due to higher velocities was significant for higher mass fractions.

In Figure A-4, the minimum and maximum mass fraction models in the monomeric form are compared. The epoxy models show a tight zone where the frictional output lies. For BMI, addition of polymer atoms significantly degrades the frictional force. Clustering was observed in the low mass fraction models resulting in a lower friction force than the high mass fraction models. As reported by Pisani et al. [101] for the fluorinated cyanate esters, epoxy shows an inverse relation of friction force with the polymer mass fraction. Figure A-5 shows frictional resistance displayed by the same models but after polymerization. Crosslinking the models reduces the spread in the data between different polymer mass fraction models. The epoxy model with the mass fraction of 15% is only slightly affected by the increase in velocity, which is not observable due to the logarithmic scale in the figure.

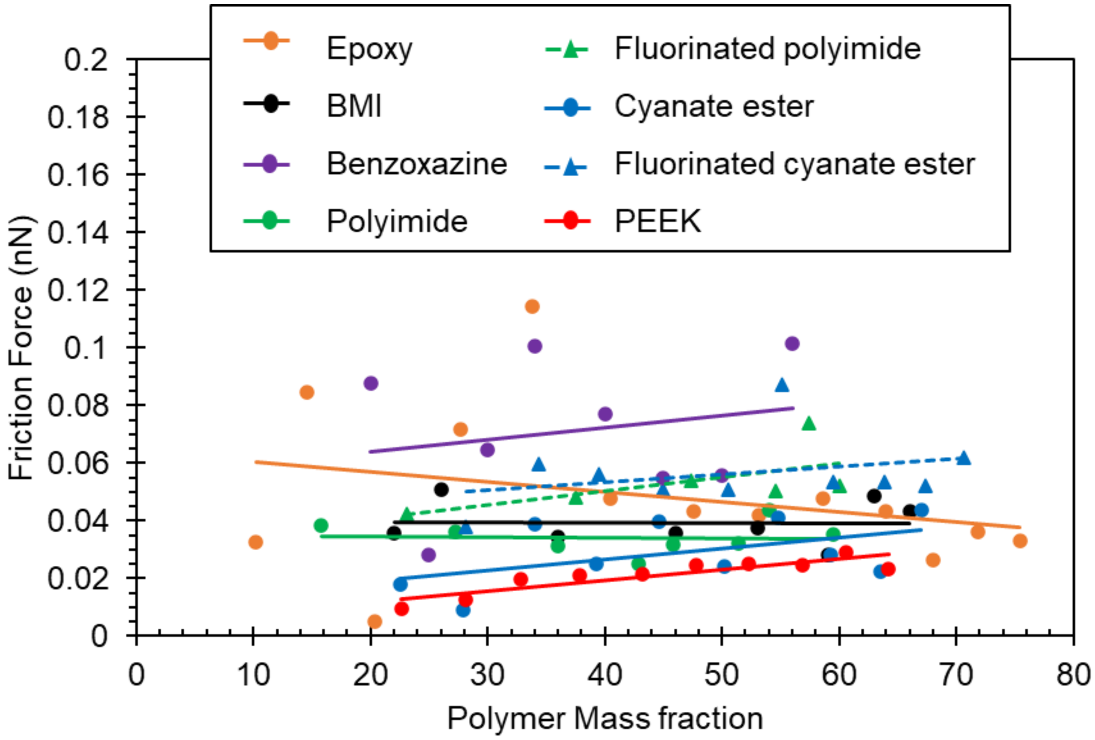

Figure A-2. Friction force as a function of polymer mass fraction at 10 m/s velocity for polymer case, including data from Deshpande et al. [102], Pisani et al. [101], and Patil et al. [100].

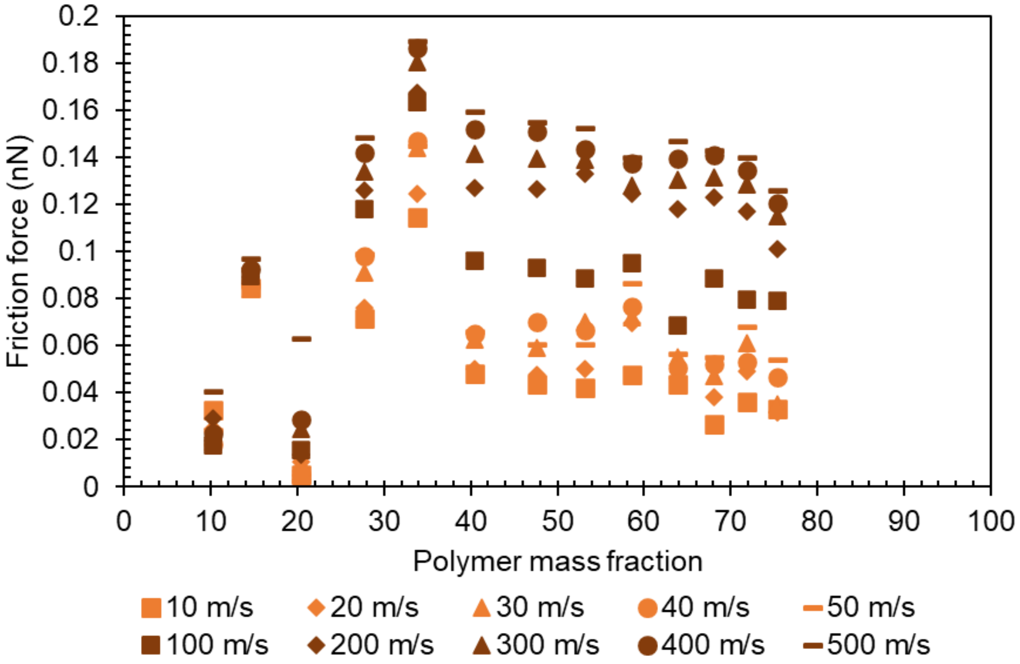

Figure A-3. Friction force as a function of polymer mass fraction for flCNT/epoxy systems at all simulated velocities

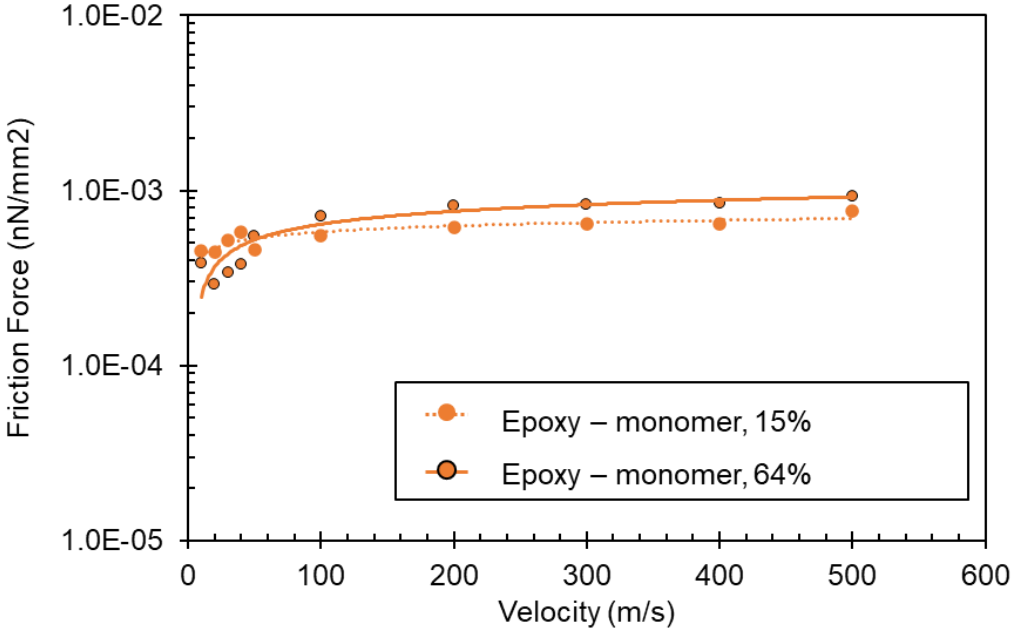

Figure A-4. Friction force of polymer systems as a function of velocity for the monomer case.

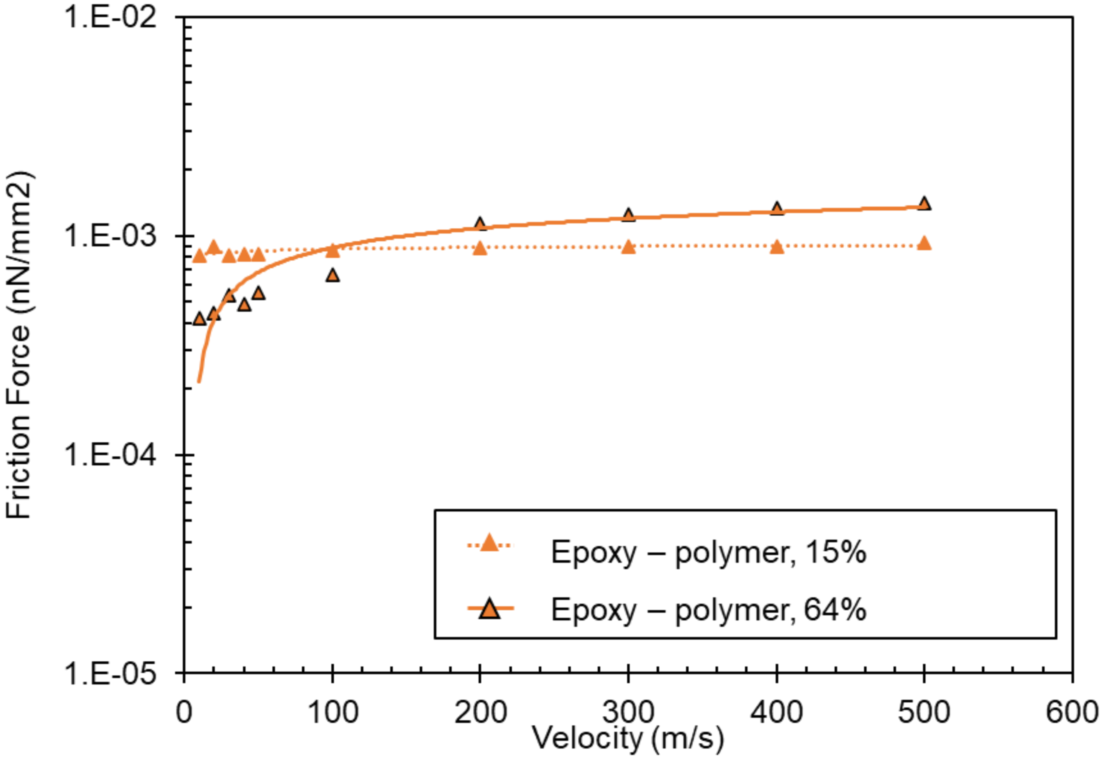

Figure A-5. Friction force of polymer systems as a function of velocity for the polymer case.

B Single Polymer Chain Strength

B.1 Boundary conditions

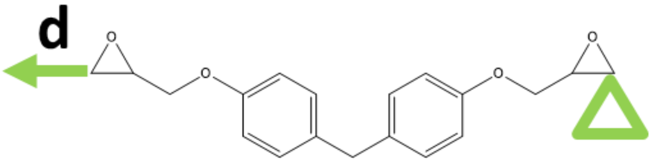

Figure B-1. Loading condition for assessing different boundary conditions. *d* is the applied displacement.

Various boundary conditions were assessed to establish a valid workflow for conducting the single polymer chain strength simulations. Figure B-1 shows the load application on a single bisphenol F epoxy chain. One epoxy ring C was fixed by setting the forces to zero and the other epoxy ring C was displaced by applying a constant displacement rate of 0.01 Å/ps.

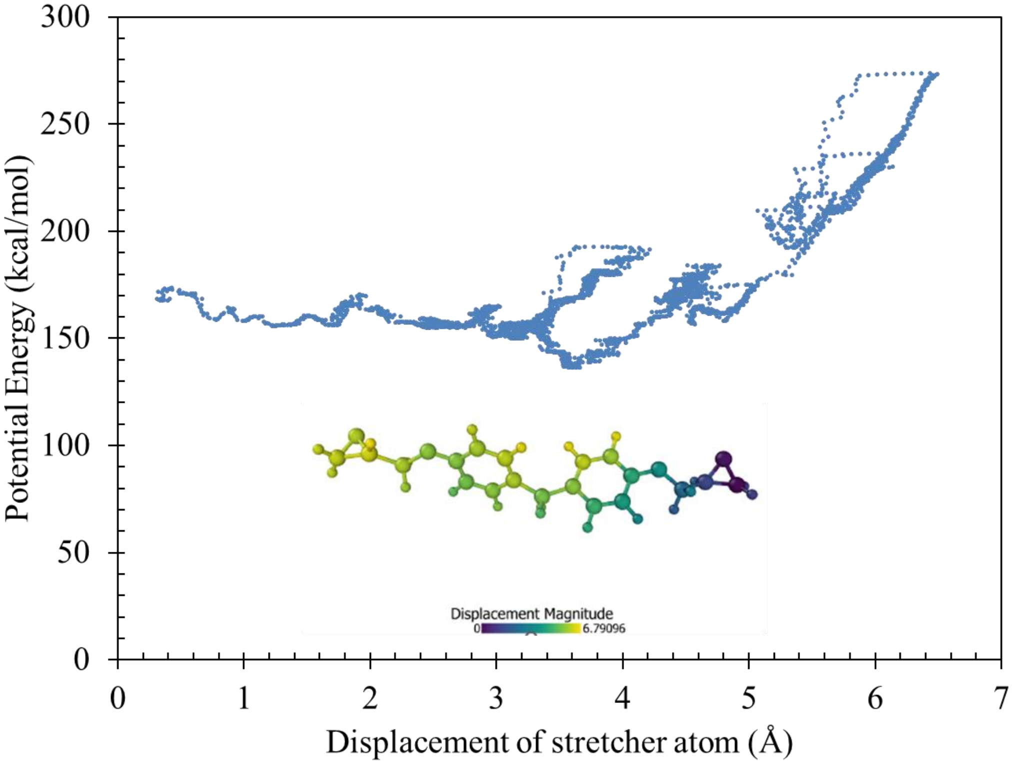

Figure B-2. Potential energy curve with elastic stretching of the chain. (inset) Snapshot of the polymer chain at maximum displacement.

The first setup involved a static stretching of the chain without any morse bonds, hence elastic stretching. Figure B-2 shows the potential energy curve for the elastic stretching run. The simulation was a static simulation with molecular minimizations performed after every timestep to update the chain configuration. The conjugate gradient method was implemented [68]. Since no bond breaks were simulated, the failure of the chain was not achieved.

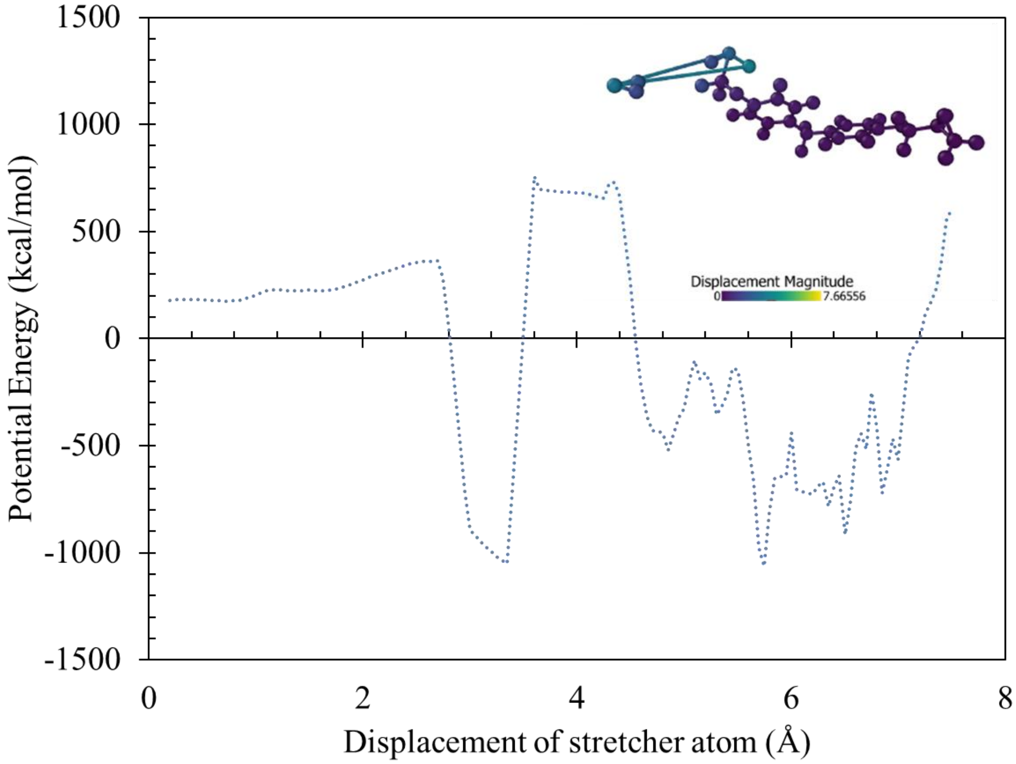

Figure B-3. Potential energy curve for the static stretching of the chain. (inset) Snapshot of the polymer chain at maximum displacement.

The second setup also was a static stretching simulation but with morse bonds in place. Figure B-3 shows the potential energy curve for the static stretching run. Similar to the first run, molecular minimizations with conjugate gradient were performed after each timestep. With this setup there was a bond break near the applied load with minimal to no transfer through the chain axis. Post-failure, the energy curve displayed uncommon artifacts with multiple peaks and valleys. This occurrence was the artifact of using a fixed bond force field which, even without bonds, carries energy terms from neighboring atoms.

The third setup was identical to the second run but with load application to both the epoxy ring Cs. Figure B-4 shows the potential energy curve for the two-way static stretching run. Similar to the second run, the post-failure energy computations were inaccurate due to the fixed bond force field.

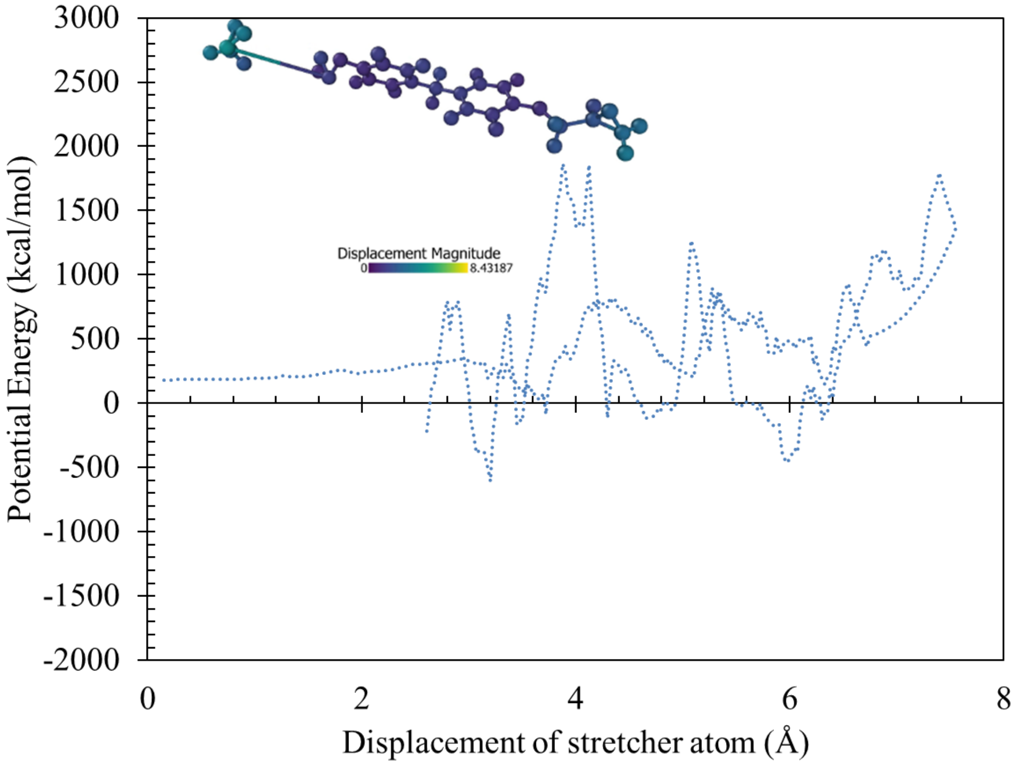

Figure B-4. Potential energy curve for the two-way static stretching of the chain. (inset) Snapshot of the polymer chain at maximum displacement.

The final setup was a molecular dynamics simulation where a canonical ensemble (NVT) was applied at 300 K temperature over 0.5 ns. Figure B-5 shows the potential energy curve for the dynamic stretching run. With the thermal effects in play, the energy curve shows the expected behavior throughout the simulation. Post-failure, the energy swiftly approaches to zero without any extra loading cycles. This setup was eventually used for all the single polymer chain stretching simulations.

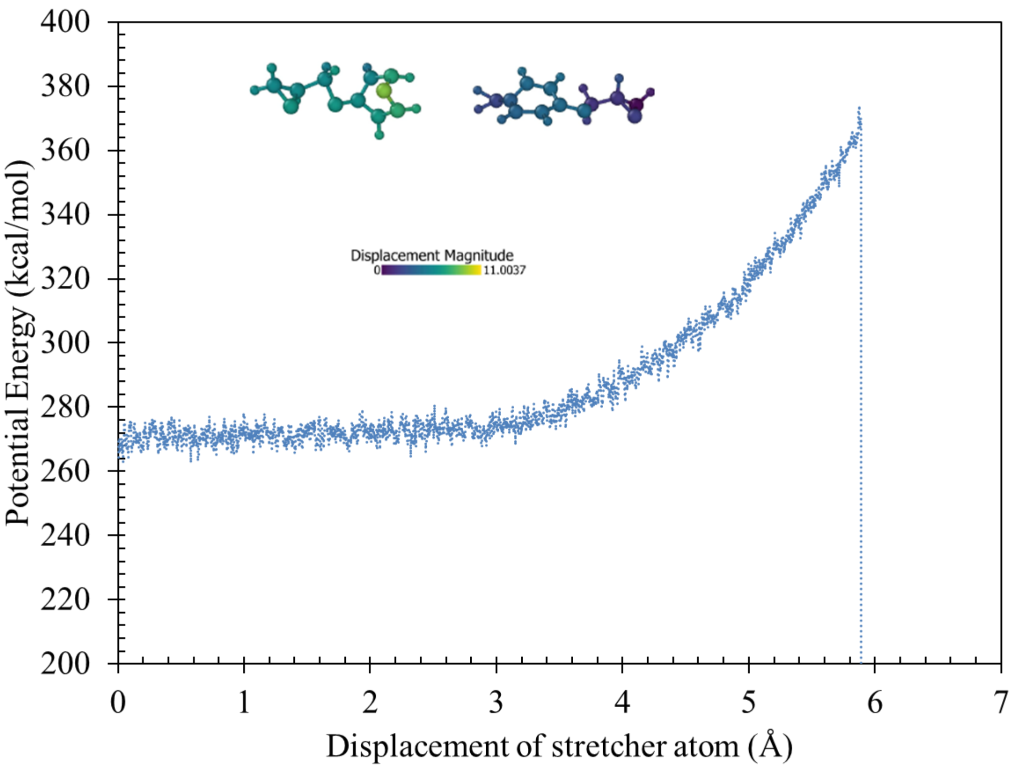

Figure B-5. Potential energy curve for the dynamic stretching of the chain. (inset) Snapshot of the polymer chain at maximum displacement.

B.2 Displacement rate analysis

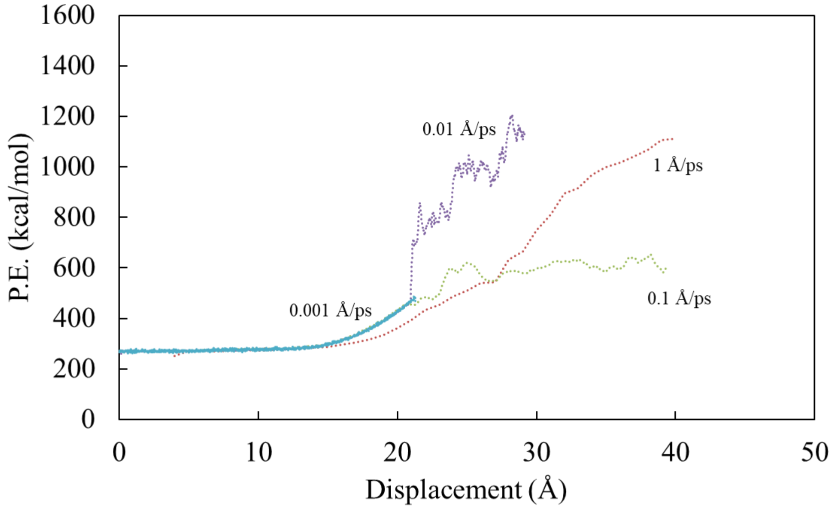

Figure B-6. Displacement rate effect on single chain failure.

Figure B-6 shows the potential energy (P.E.) curve for different displacement rates with identical simulation settings. All the simulations were performed at 298 K temperature. The pre-failure response did not get affected by the different displacement rates but the post-failure, the results were dramatically different. No discernable trends were observed. The simulation efficiency plot in Figure B-7 suggests that the slower rates show significant increase in the simulation run time. Since no trend was observed from Figure B-6, the displacement rate can be selected solely based on the lowest wall time.

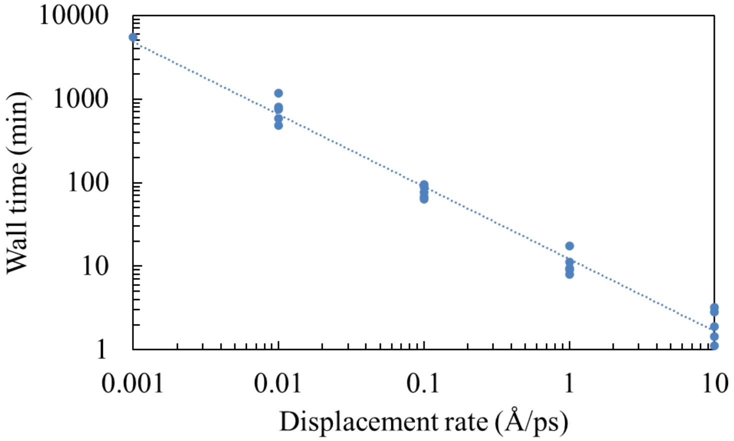

Figure B-7. Simulation efficiency for different displacement rates.

Figure B-8 lists all the dissociated bonds at different displacement rates. The data does not provide any definitive results. The broken bonds were random and irreproducible.

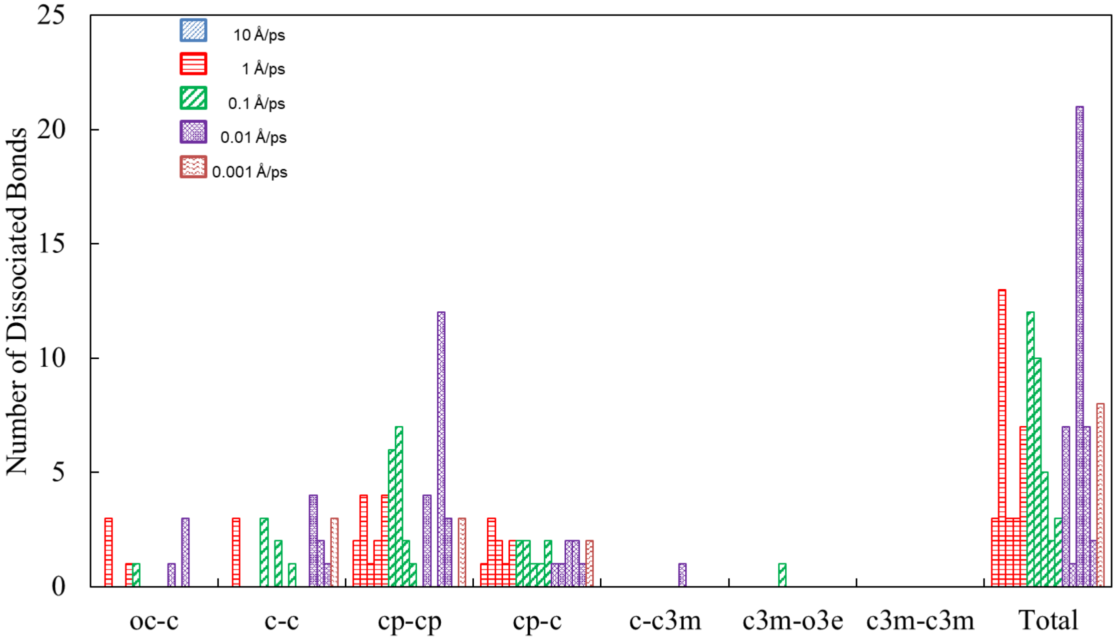

Figure B-8. Dissociated bonds count for different displacement rates. The involved atoms are ether O (*oc*), sp^3 C (*c*), sp^2 C (*cp*), epoxy C (*c3m*), and epoxy O (*o3e*).

B.3 Simulation temperature analysis

Figure B-9 shows the potential energy (P.E.) curve for different temperatures with identical simulation settings. All the simulations were performed at 0.01 Å/ps displacement rate. The mechanical response with 1 K temperature shows the repeatable nature when five simulations were performed for statistical purposes. For the other temperature values, the post-failure energy curve shows a high stochastic effect due to the increased influence of thermal vibrations. Based on the reproducibility, the 1 K temperature was selected to reduce noise in the data. Additionally, Figure B-10 shows that the 1 K temperature simulations were the fastest.

Figure B-11 lists all the dissociated bonds at different temperatures. Unlike with Figure B-8, a clear trend was observed. For 1 K temperature, for each of the five runs the same bond broke. For higher temperatures, the bond breaks were random without any observable trends.

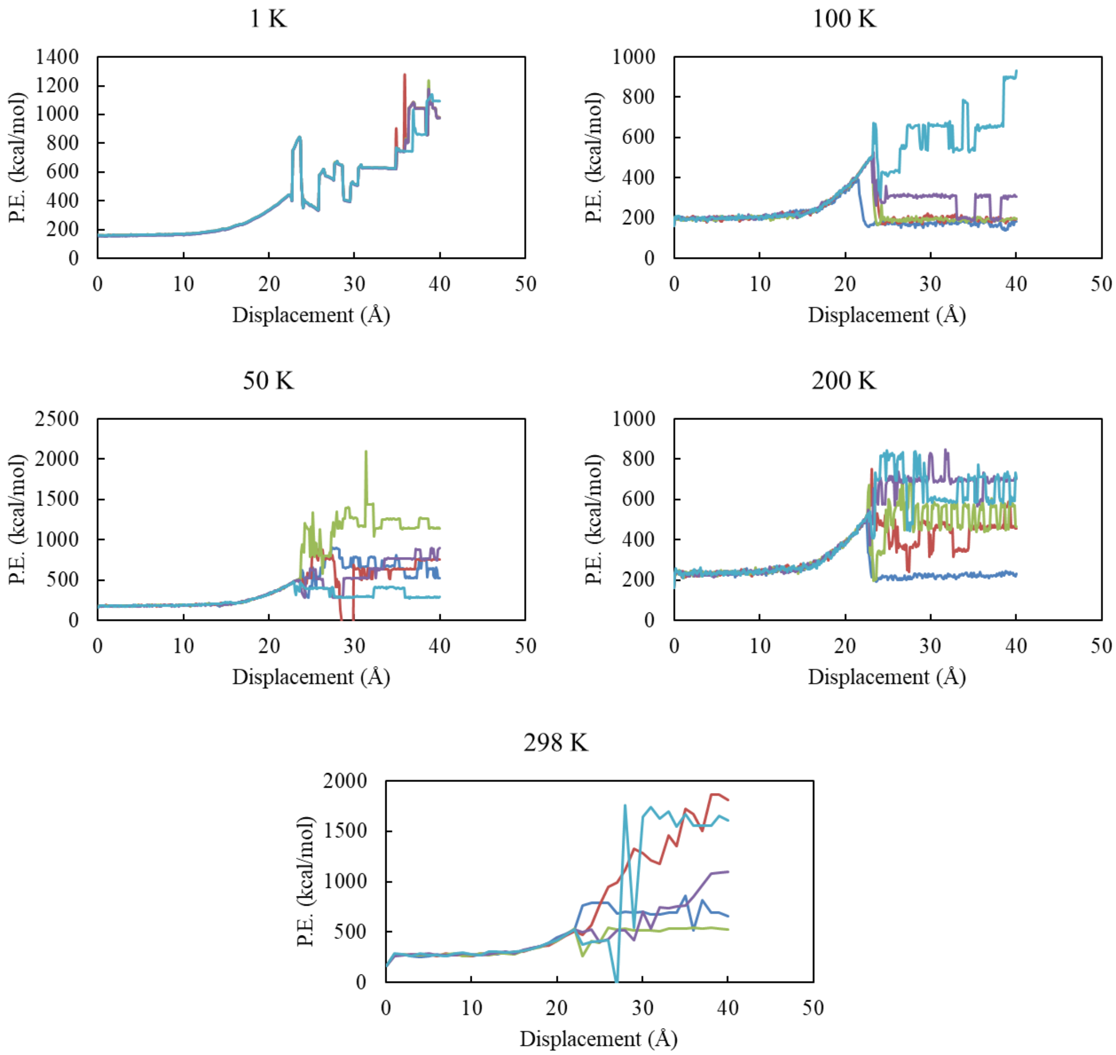

Figure B-9. Temperature effect on single chain failure.

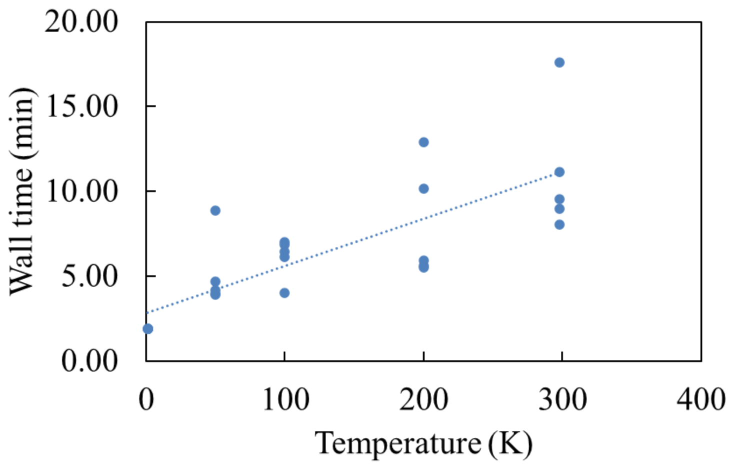

Figure B-10. Simulation efficiency for different temperatures.

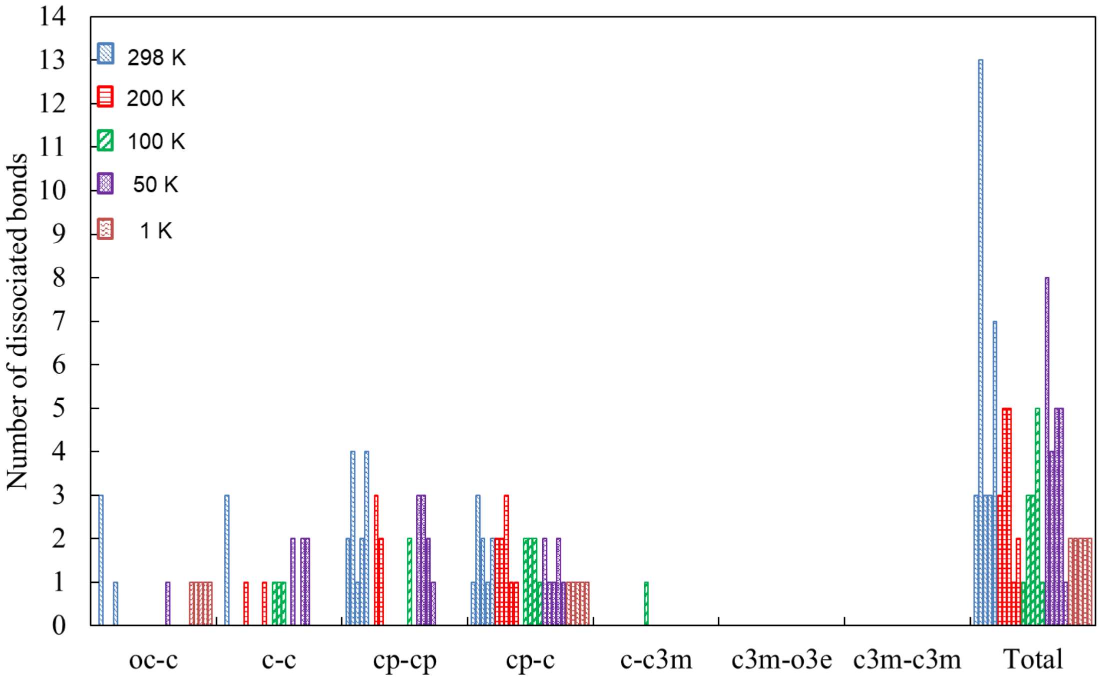

Figure B-11. Dissociated bonds count for different temperatures. The involved atoms are ether O (*oc*), sp^3 C (*c*), sp^2 C (*cp*), epoxy C (*c3m*), and epoxy O (*o3e*).

C Interaction Energy with PES

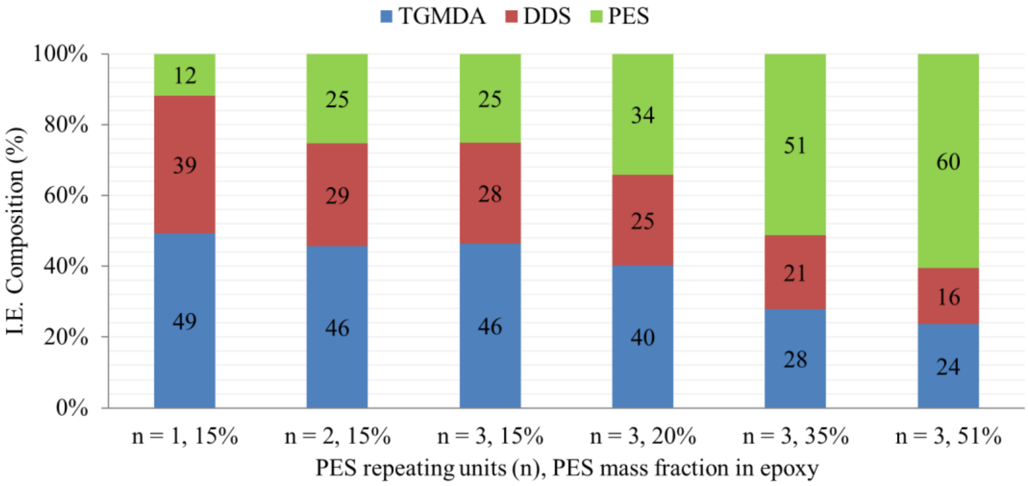

Figure C-1. Interaction energy contribution from individual monomers.

Figure C-1 shows the individual contribution of the monomers towards the interaction energy with the flCNTs. The first three data bars can be compared to understand the effect of molecular weight of PES on the interaction energy contribution. These data bars (n=1, 15%; n=2, 15%; n=3, 15%) show that increasing the molecular weight beyond *n*=2 does not benefit the interaction but adds to the monomer mass fraction. The last four data bars (n=3) can be compared to influence of PES mass fraction on the individual contribution to the interaction energy. It is evident that PES dominates the energy contribution. The PES molecule is flexible chain which can align and conform within the polymer layer. This flexibility and the presence of more phenyl rings results in the most contribution. Figure C-2 shows the molecular structures of the three modeled PES molecules. The larger molecule consists of 6 phenyl rings, the most in any molecule modelled in this study.

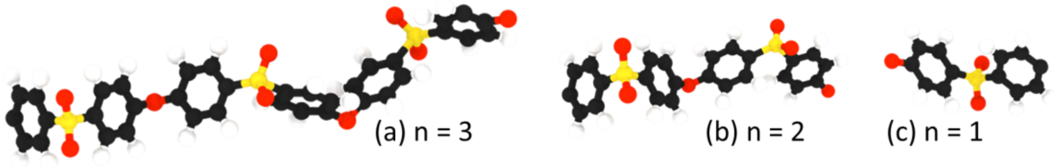

Figure C-2. Molecular models of the three PES molecules.

To understand the reason for PES dominating the interaction energy, atomic count profile was generated for one of the model where *n* = 1 PES was in the polymer layer. The PES mass fraction in the polymer layer was 21.9 %. The atomic profile in Figure C-3 shows that PES molecules adhere to the flCNT surface due to their mobility even when they make up just 21.9% of the polymer atoms. As shown in Figure C-3 (bottom-left) the majority of phenyl rings aligned at one of the interfaces belong to the PES molecule. In summary, inclusion of PES benefits the interfacial interaction between the polymer and the flCNTs.

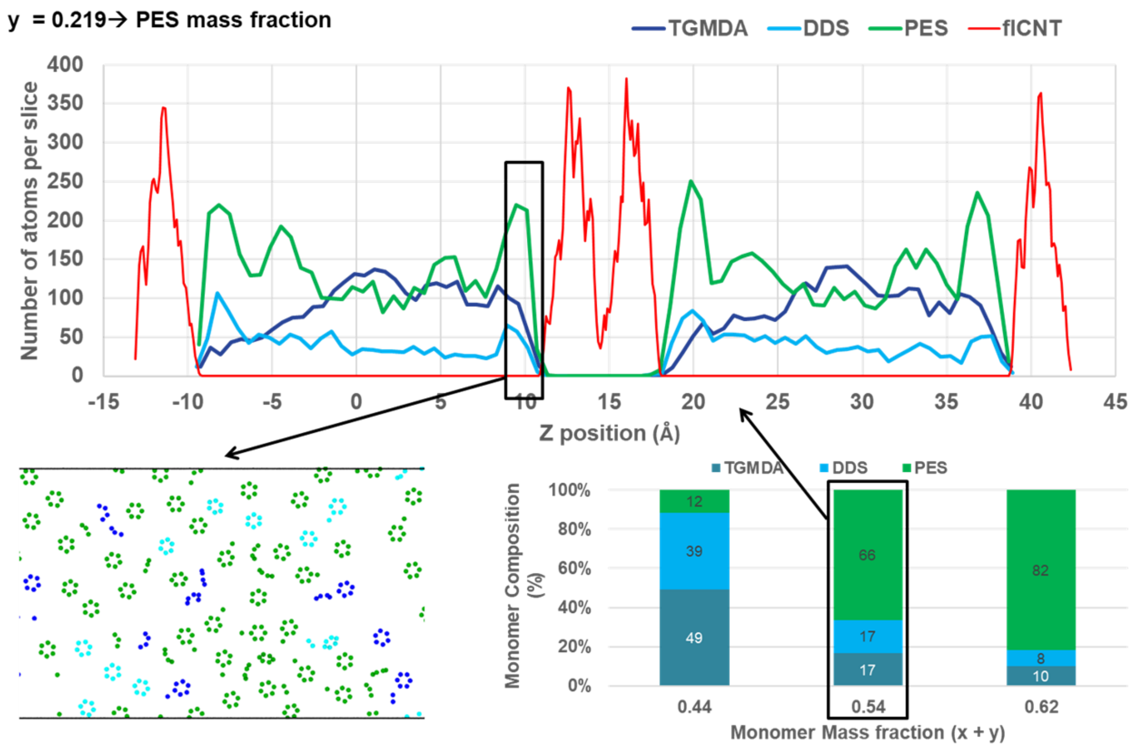

Figure C-3. Atomic count profile of individual monomers across Z direction for 0.54 polymer mass fraction (top), Monomer composition in the polymer layers for 0.44, 0.54, and 0.62 polymer mass fractions (bottom-right), and phenyl ring alignment at one of the interfaces for 0.54 polymer mass fraction (bottom-left). Where *x* is the polymer mass fraction without PES.

D HPC Specifications

Three different clusters were used to generate all the MD data in this document.

D.1 Superior (generation 1.0) and Portage

Organization: Michigan Technological University

1. 92 CPU compute nodes - 16 CPU cores/node (Intel Xeon E5-2670 2.60 GHz) - 64 GB RAM - providing 30 TFLOPS.
2. 4 CPU compute nodes - 24 CPU cores/node (Intel Xeon E4-2680 2.50 GHz) - 256 GB RAM - providing 2 TFLOPS.
3. 5 GPU compute nodes - 16 CPU cores/node (Intel Xeon E5-2670 2.60 GHz) - 64 GB RAM and 4 NVIDIA Tesla M2090 GPUs - providing 13 TFLOPS.
4. 3 storage nodes - 32 TB/node usable space.

Portage has 3 TFLOPS of CPU computing capacity.

D.2 Superior (generation 2.0)

Organization: Michigan Technological University

85 CPU compute nodes - 32 CPU cores/node (Intel Xeon E5-2683 2.10 GHz) - 256 GB RAM - providing 91 TFLOPS.

D.3 Center for High Performance Computing – Notchpeak

Organization: The University of Utah

9 GPU nodes – 32 cores/node (Intel XeonSP Skylake) or 40 cores/node (Intel XeonSP Cascadelake) - 192GB memory. Mix of P40, V100, A100, and RTX2080Ti GPUs.

1. 25 dual socket nodes (Intel XeonSP Skylake) with 32 cores each.
    a. 4 nodes with 96 GB memory.
    b. 19 nodes with 192 GB memory.
    c. 2 nodes with 768 GB memory.
2. 1 dual socket node (Intel XeonSP Skylake) with 36 cores, 768 GB memory.

3. 7 dual socket nodes (Intel XeonSP Cascadelake) with 40 cores, 192 GB memory.
4. 32 single socket AMD Rome nodes with 64 cores, 256 GB memory.
5. 2 dual socket AMD Naples nodes, each with 64 cores, 512 GB memory.

E LAMMPS and Python scripts

A number of LAMMPS scripts were developed to help with conducting MD simulations for all the research in this document. The research is part of different collaborations and contains intellectual property. To maintain confidentiality, the scripts cannot be included in this document. However, some of the scripts can be made available upon request. Requests can be made via email to ppdeshpa@mtu.edu or gmodegar@mtu.edu.

All the analysis presented in the document was performed on MS Excel and Python. Python scripts used were developed under collaborative efforts and are not directly available. A request can be made to the above mentioned email addresses.

E.1 MD simulation statistics

- Time period : September 1, 2015, to June 24, 2022
- Total completed MD simulations : 9355
- Wall time (h:mm:ss) : 120,548:19:43
- CPU time (h:mm:ss) : 2,865,387:30:33
- Computing value ($) : 286,538.70

F Copyright documentation

F.1 Copyright Agreement for Chapter 3

CONTRIBUTING AUTHOR COPYRIGHT RELEASE FORM

As author of the chapter/contribution titled Multiscale Modelling of the Cure Process in Thermoset Polymers using ICME ,

to appear in the *Proceedings of the American Society for Composites—35th Technical Conference—2020* Electronic product, I hereby agree to the following:

1. To grant to DEStech Publications, Inc., 439 North Duke Street, Lancaster, PA, 17602, copyright of the above named chapter/contribution (for U.S. Government employees to the extent transferable), in print, electronic, and online formats. However, the undersigned reserve the following:
   a. All proprietary rights other than copyright, such as patent rights.
   b. The right to use all or part of this article in future works.
   DEStech Publications thereby retains full and exclusive right to publish, market, and sell this material in any and all editions, in the English language or otherwise.

2. I warrant to DEStech Publications, Inc., that I am the (an) author of the above-named chapter/contribution and that I am the (a) copyright holder of the above-named chapter/contribution granted to DEStech Publications, Inc.
3. I warrant that, where necessary and required, I have obtained written permission for the use of any and all copyrighted materials used in the above-named chapter/contribution. I understand that I am responsible for all costs of gaining written permission for use of copyrighted materials.
4. I agree to assume full liability to DEStech Publications, Inc. and its licensee, and to hold DEStech Publications, Inc. harmless for any claim or suit filed against DEStech Publications, Inc. for violation of copyrighted material used in the above-named contribution.

Please sign and date this form and retain a copy for your records. Please include original form with your chapter/paper.

Thank you for your cooperation.

Please print name: Prathamesh P. Deshpande

Signed: [redacted] Dated: 07/01/2020

F.2 Copyright Agreement for Chapter 3

CONTRIBUTING AUTHOR COPYRIGHT RELEASE FORM

As author of the chapter/contribution titled _Process Modelling the Cure of Bisphenol-A Epoxy/Jeffamine System using ICME_ , to appear in the Proceedings of the American Society for Composites—36th Technical Conference—2021 Electronic product, I hereby agree to the following:

1. To grant to DEStech Publications, Inc., 439 North Duke Street, Lancaster, PA, 17602, copyright of the above named chapter/contribution (for U.S. Government employees to the extent transferable), in print, electronic, and online formats. However, the undersigned reserve the following:

a. All proprietary rights other than copyright, such as patent rights.

b. The right to use all or part of this article in future works.

DEStech Publications thereby retains full and exclusive right to publish, market, and sell this material in any and all editions, in the English language or otherwise.

2. I warrant to DEStech Publications, Inc., that I am the (an) author of the above-named chapter/contribution and that I am the (a) copyright holder of the above-named chapter/contribution granted to DEStech Publications, Inc.

3. I warrant that, where necessary and required, I have obtained written permission for the use of any and all copyrighted materials used in the above-named chapter/contribution. I understand that I am responsible for all costs of gaining written permission for use of copyrighted materials.

4. I agree to assume full liability to DEStech Publications, Inc. and its licensee, and to hold DEStech Publications, Inc. harmless for any claim or suit filed against DEStech Publications, Inc. for violation of copyrighted material used in the above-named contribution.

Please sign and date this form and retain a copy for your records. Please include original form with your chapter/paper.

Thank you for your cooperation.

Please print name: _Prathamesh P. Deshpande___________________________________

Signed: _[redacted]_____________Dated: _8/2/2021_________________________

F.3 Copyright Agreement for Chapter 4

PERMISSION/LICENSE IS GRANTED FOR YOUR ORDER AT NO CHARGE

This type of permission/license, instead of the standard Terms and Conditions, is sent to you because no fee is being charged for your order. Please note the following:

- Permission is granted for your request in both print and electronic formats, and translations.

- If figures and/or tables were requested, they may be adapted or used in part.

- Please print this page for your records and send a copy of it to your publisher/graduate school.

- Appropriate credit for the requested material should be given as follows: "Reprinted (adapted) with permission from Langmuir 2021, 37, 39, 11526–11534; DOI: 10.1021/acs.langmuir.1c01800. Copyright 2021 American Chemical Society."

- One-time permission is granted only for the use specified in your RightsLink request. No additional uses are granted (such as derivative works or other editions). For any uses, please submit a new request.

If credit is given to another source for the material you requested from RightsLink, permission must be obtained from that source.

American Chemical Society's Policy on Theses and Dissertations:

This policy addresses permission to include your article(s) or portions of text from your article(s) in your thesis.

Reuse/Republication of the Entire Work in Theses or Collections: Authors may reuse all or part of the Submitted, Accepted or Published Work in a thesis or dissertation that the author writes and is required to submit to satisfy the criteria of degree-granting institutions. Such reuse is permitted subject to the ACS' "Ethical Guidelines to Publication of Chemical Research." Appropriate citation of the Published Work must be made as follows:

"Reprinted with permission from Langmuir 2021, 37, 39, 11526–11534; DOI: 10.1021/acs.langmuir.1c01800. Copyright 2021 American Chemical Society." Insert the appropriate wording in place of the capitalized words. Citation information may be found after the "Cite this:" heading below the title of the online version and at the bottom of the first page of the pdf or print version of your ACS journal article.

If the thesis or dissertation to be published is in electronic format, a direct link to the Published Work must also be included using the ACS Articles on Request author-directed link.

If your university requires written permission and your manuscript has not yet received a DOI (published ASAP), send a request to copyright@acs.org that includes the manuscript number, the name of the ACS journal, and the date that you need to receive our reply.

If your university requires you to obtain permission for manuscripts in ASAP status or final published articles, you must use the RightsLink permission system. See RightsLink instructions at http://pubs.acs.org/page/copyright/permissions.html and make requests at the "Rights & Permissions" link under the title of the online version of the article.

Submission to a Dissertation Distributor: If you plan to submit your thesis to UMI or to another dissertation distributor, you should not include the unpublished ACS paper in your thesis if the thesis will be disseminated electronically, until ACS has published your paper. After publication of the paper by ACS, you may release the entire thesis (not the individual ACS article by itself) for electronic dissemination through the distributor; ACS's copyright credit line should be printed on the first page of the ACS paper.